Magnesium Alloys
Processing, Potential and Applications

*Edited by Tomasz Arkadiusz Tański,
Katarzyna Cesarz-Andraczke and Ewa Jonda*

Magnesium Alloys - Processing, Potential and Applications

Edited by Tomasz Arkadiusz Tański,
Katarzyna Cesarz-Andraczke
and Ewa Jonda

Magnesium Alloys - Processing, Potential and Applications
http://dx.doi.org/10.5772/intechopen.103992
Edited by Tomasz Arkadiusz Tański, Katarzyna Cesarz-Andraczke and Ewa Jonda

Notice

Statements and opinions expressed in the chapters are these of the individual contributors and not necessarily those of the editors or publisher. No responsibility is accepted for the accuracy of information contained in the published chapters. The publisher assumes no responsibility for any damage or injury to persons or property arising out of the use of any materials, instructions, methods or ideas contained in the book.

We are IntechOpen,
the world's leading publisher of
Open Access books
Built by scientists, for scientists

6,700+
Open access books available

180,000+
International authors and editors

195M+
Downloads

156
Countries delivered to

Our authors are among the
Top 1%
most cited scientists

12.2%
Contributors from top 500 universities

CLARIVATE ANALYTICS
BOOK CITATION INDEX
INDEXED
WEB OF SCIENCE™

Selection of our books indexed in the Book Citation Index
in Web of Science™ Core Collection (BKCI)

Interested in publishing with us?
Contact book.department@intechopen.com

Numbers displayed above are based on latest data collected.
For more information visit www.intechopen.com

Meet the editors

Prof. Tomasz Tański is the head of the Department of Engineering Materials and Biomaterials, Silesian University of Technology, Poland, and a member of the Committee of Metallurgy of the Polish Academy of Sciences. He is also a specialist in non-ferrous alloys, composite and nanostructured materials, and structural engineering materials. He has authored or co-authored more than 400 scientific publications worldwide, including 15 monographs and books. He has won twenty national and international awards and honors. He is and/or was a supervisor or contractor for more than fifteen research and didactic projects in Poland and abroad. He is also a reviewer and promoter of numerous scientific papers, including eight doctoral research papers in the field of nanotechnology and materials.

Dr. eng. Katarzyna Cesarz-Andraczke is a professor's assistant in the Department of Engineering Materials and Biomaterials, Silesian University of Technology, Poland. Her research interests include the structural characteristics, mechanical properties, and corrosion resistance in vitro of light metal alloys intended for resorbable medical implants. In 2016, she obtained a Ph.D. in Materials Engineering. The thematic scope of her doctoral dissertation was resorbable magnesium (Mg)-based metallic glasses. She is a co-author of two patents and more than fifty publications on the properties and structure of Mg and calcium (Ca) alloys. As part of her scientific work, Dr. Cesarz-Andraczke is looking for an effective solution to the too-rapid degradation of potential biomaterials.

Dr. eng. Ewa Jonda is a professor's assistant in the Department of Engineering Materials and Biomaterials, Silesian University of Technology, Poland, and a member of the Polish Association of Mechanical Engineers and Technicians. Her scientific interests include materials engineering, in particular surface engineering (e.g., laser processing and thermal spraying). Dr. Jonda is a reviewer and promoter of numerous scientific papers in the field of engineering materials. She is the author or co-author of many scientific articles and the winner of awards and medals for scientific achievements.

Contents

Preface

Magnesium alloys have excellent physical and mechanical properties such as high strength-to-weight ratio, electromagnetic shielding, excellent vibration and shock absorption, good machinability, high damping capacity, and good castability and recyclability. Compared to other metals and polymers, magnesium has no toxic hazards. Magnesium alloys have obvious advantages in thermal conductivity, vibration damping performance, and damping capacity, and their application in the automotive field is expanding further. This unique material property has led to increased use of magnesium and its alloys in various industrial, automotive, aerospace, and biological applications. However, significant problems in the production process of magnesium, such as low ductility at room temperature and high oxidation and flammability at high service temperatures, limit its application.

Magnesium Alloys – Processing, Potential and Applications discusses the latest developments in and applications of magnesium alloys. The book consists of several chapters relating to the production, modification, and use of magnesium alloys in various industries. The introductory chapter introduces readers to processing, potential and applications of Magnesium alloys. Due to the growing importance of lightweight construction materials, chapter "Applications of High-Pressure Die-Casting (HPDC) Magnesium Alloys in Industry" examines methods of producing magnesium alloys to achieve the best possible functional properties. Chapter "Effects of Dimensionality Reduction for High-Efficiency Mg-Based Thermoelectrics" reports on the use of magnesium alloys as thermoelectric elements. Chapter "Dissolvable Magnesium Alloys in Oil and Gas Industry" describes the possibilities of using soluble magnesium alloys. Chapter "Development of Mg-Based Bulk Metallic Glasses and Applications in Biomedical Field" discusses the concepts and advances in defining key properties for implant applications. Magnesium alloys with biocompatible chemical composition are considered as potential resorbable biomaterials.

For more than a decade, scientists have been trying to develop a manufacturing process and select the appropriate chemical composition that would meet the requirements of medical implantology. The book presents the latest literature reports in this field, but also mentions the barriers that researchers encounter in this area. It also examines the impact of the development of these alloys on improving patient quality of life and reducing associated rehabilitation costs.

Tomasz Arkadiusz Tański, Katarzyna Cesarz-Andraczke and Ewa Jonda
Department of Engineering Materials and Biomaterials,
Silesian University of Technology,
Gliwice, Poland

Section 1

Introduction to Magnesium Alloys

Chapter 1

Introductory Chapter: Magnesium Alloys

Tomasz Arkadiusz Tański, Katarzyna Cesarz-Andraczke and Ewa Jonda

1. Introduction

Non-ferrous metal alloys, including magnesium alloys, are the subject of research in numerous research and scientific centres and universities, both in Poland and abroad, as well as at major manufacturers of the automotive, mechanical engineering, shipbuilding, aviation, chemical, energy, electronics, textile and even nuclear industries. The combination of low density of magnesium alloys (1.5–1.8 g/cm^3), the best among all currently known construction materials and high strength in relation to low weight, as well as the possibility of use on machine parts operating at temperatures up to 300°C, make these alloys widely used in various industries.

Demand for magnesium and its alloys continues to grow, as they have the potential to be used in many new areas of life, as well as in expanding use in existing applications. The growth of the electronic devices market related to the growing demand for ever lighter vehicles and hand tools has repeatedly increased the trade demand for castings from Mg alloys and the efforts of manufacturers in the area of their research and development [1–3]. High specific strength (the ratio of tensile strength and modulus of elasticity to specific weight), the ability to damp vibrations and low resistance to corrosion, allows the use of castings from Mg alloys as an alternative solution to Al alloys, as well as for parts made of plastics and composite materials.

In order to reduce the weight of products while maintaining the assumed strength and stiffness, light metal alloys are most often used in the transport industry or machine construction. As a result, products made of light metals reduce the negative impact of human activity on the natural environment, while ensuring their competitiveness [4]. Industrial Mg alloys used in aviation (WE43, MSR, RZ5) are characterized by a very low elongation compared to alloys intended for use as parts in the automotive industry. Seventy percent of magnesium alloys production is used in the automotive industry, and the remaining thirty percent mainly in the aerospace and electronics industries. For example, Audi (automotive) company, in order to reduce the weight of vehicles, produces five-speed gears made of magnesium alloy AZ91HP (Cu 0.016%, Mn 0.17%, Zn 0.72%, Si 0.03%, Fe 0.002%, Al 9.45%, Ni 0.025%). Vehicles in which parts made of light metal alloys are used burn less fuel, which in turn reduces the consumption of fossil fuels and the emission of pollutants into the atmosphere [5, 6].

In addition, magnesium alloys have found applications in aviation (helicopter gear housings, A320, F16 aircraft components), automotive industry (Rolls Royce and BMW engines, wheel rims, city bus handrails), electronics industry (Nikon

SLR camera body), gardening industry (Nikon body crankcase in Husqvarna petrol mowers), recreation (elements of bicycle construction), construction (window structures, bolts, handles) or medicine (implants, e.g. Magnezix) [5, 7]. Currently, implants made of magnesium alloys (Magnezix®) are implanted in patients with wrist fractures. The metal screw after absorption is replaced by bone tissue. Screws made of Magnezix® are already being implanted in patients. On the basis of observations, wound healing after 6 weeks and gas evolution as a result of screw degradation were observed. No postoperative complications were reported. Injuries to the osteoarticular system, as well as diseases of the musculoskeletal system, including the continuous increase in the incidence of bone cancer, are the main and most common threat to the health of modern society. Hence the growing demand for new biomaterials, such as resorbable magnesium alloys.

The monograph "Magnesium Alloys - Processing, Potential, Applications" collects the latest processing methods as well as potential and newly developed areas of application of magnesium alloys. Due to the continuous improvement and development of the use of magnesium alloys in the automotive industry, the book contains content regarding both application possibilities and an improved version of the method of their production. Recent reports on the use of magnesium alloys as thermoelectric elements have also been presented. Details on the applications of dissolvable magnesium alloys are presented. In medicine, Mg and its alloys have been considered for two decades as a degradable implant material. The concept and progress in determining key properties for implantology applications are discussed.

The growing trends in the production of magnesium alloys indicate an increased need for their use in the broadly understood construction industry, therefore it is expected that these alloys will become one of the most frequently used construction materials of our century, which is the basis for maintaining and developing a high pace of research on the problem of light alloys.

Author details

Tomasz Arkadiusz Tański*, Katarzyna Cesarz-Andraczke and Ewa Jonda
Silesian University of Technology, Poland

*Address all correspondence to: tomasz.tanski@polsl.pl

IntechOpen

References

[1] Friedrich HE, Mordike BL, editors. Magnesium Technology: Metallurgy, Design Data, Applications. New York: Springer, Berlin; 2006

[2] Tan J, Ramakrishna S. Applications of magnesium and its alloys: A review. Applied Sciences. 2021;**11**:6861. DOI: 10.3390/app11156861

[3] Tański T. Kształtowanie struktury i własności powierzchni stopów Mg-Al-Zn, scientific International of the World Academy of materials and manufacturing engineering publishing scientific monographs in polis hor English only. Open Access Library. 2012;**2**(8):9-16

[4] Kazimierz AK, Oczo E. Kształtowanie metali lekkich. Warszawa: PWN; 2012

[5] Available from: www.Intlmag.org. 2018

[6] Kazimierz Poznański JSMS. Inteligentne innowacje w przemyśle aluminiowym. Izba Gospodarcza Metali Nieżelaznych i Recyklingu. 2017;**1**:1-5

[7] Available from: https://www.syntellix.de/en/doctor/technology.html

Section 2

Studies on New Applications of Magnesium Alloys

Chapter 2

Applications of High-Pressure Die-Casting (HPDC) Magnesium Alloys in Industry

Sophia Fan, Xu Wang, Gerry Gang Wang and Jonathan P. Weiler

Abstract

High-pressure die-cast (HPDC) magnesium alloys have seen diverse applications in the automotive industry, primarily driven by requirements in internal combustion engine (ICE) vehicles. As the automotive industry is transitioning to an electric vehicle (EV) architecture, there is a great potential for novel applications to improve driving range efficiency. In addition, there is a trend toward larger-sized automotive die castings and an increased interest in aerospace applications due to weight reduction. In this chapter, we reviewed the traditional automotive structural applications in ICE vehicles, as well as current and potential future EV and aerospace applications of HPDC magnesium alloys. The structural applications using AM50, AM60, AZ91 and AE44 magnesium alloys in traditional vehicles can be applied to modern EVs. Additionally, magnesium alloys with varying degrees of higher thermal conductivity, improved castability, superior high temperature properties and flammability need to be developed to replace battery and aerospace in-cabin-related structural materials to meet all safety requirements. Several newly developed magnesium alloys with superior castability are also reviewed for potential automotive and aerospace applications.

Keywords: high pressure die cast (HPDC), magnesium alloy, castability, automotive, aerospace, lightweighting

1. Introduction

There has been an increasing need to reduce the weight of vehicles as forced by emissions and fuel economy legislation. Therefore, lightweighting has become a very important topic for improving power efficiencies while maintaining safety and performance. Several lightweighting strategies, such as product optimization, material substitution and part consolidation, are driven by replacing higher density structural materials with less dense materials.

Magnesium and its alloys have several advantages compared with other automotive metals. Magnesium has a density of 1.74 g/cm^3, which is significantly lower than both aluminum and steel [1]. Magnesium alloys are well known to have excellent specific strength, superior automatability and castability characteristics as well as suitable for the use of self-threading fasteners [2]. Besides the commonly used magnesium alloys which might be unsuitable for service above 150°C [3, 4], heat and

creep resistant [5–7] as well as corrosion resistant [8, 9], magnesium alloys have been developed with the addition of appropriate alloying elements. The automotive industry is experiencing a transition in powertrain architectures from internal combustion engine (ICE) to electric vehicles (EV). The development in increasing thermal conductivity of magnesium alloys has supported battery-related applications [7]. On the other hand, flammability resistance has been a hot topic for magnesium alloys, and the related research has gained substantial progress which is highly valuable for aerospace applications [10–19]. Attributed to the above advantages, magnesium alloys have become one of the lightest and most popular structural metals utilized extensively in the automotive industry.

Most magnesium alloy components in industry are manufactured through high-pressure die casting (HPDC) process [20–21] which is illustrated in **Figure 1**. HPDC process offers attractive flexibility in design and manufacturing, excellent die filling characteristics and high efficiency in reduction of secondary processes required by steel structures. **Figure 2** provides a comparison of the yield strength of AZ91 fabricated by several different processes [22–25]. The high strength for that produced by HPDC process is a result of the remarkably fine microstructure from fast-cooling rate. With modern HPDC technologies, magnesium alloys can be produced in near-net shape products with large, thin-wall and complex geometry, exhibiting outstanding structural and functional performance, and therefore has been widely applied as an efficient and cost-saving method especially for high-volume productions.

In the current chapter, the applications of HPDC magnesium alloys in both historical and potential automotive and aerospace industries will be reviewed to provide an overall understanding of the successful examples and ongoing development status.
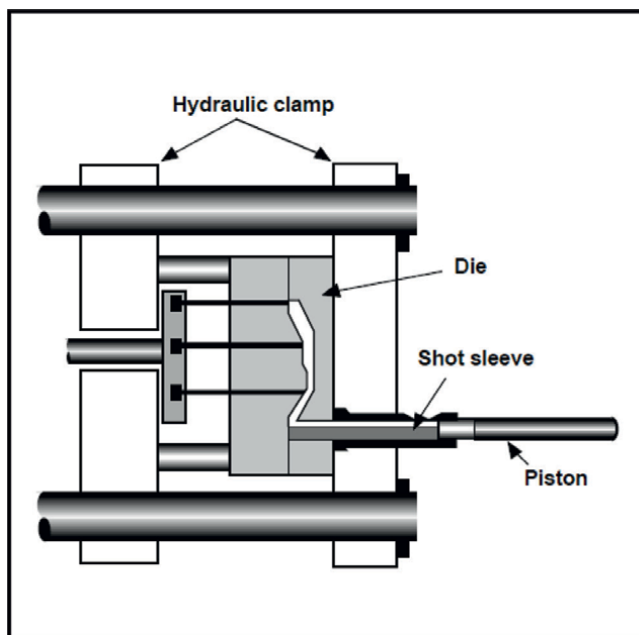
Figure 1.
Schematic diagram showing high pressure die casting (HPDC) process.
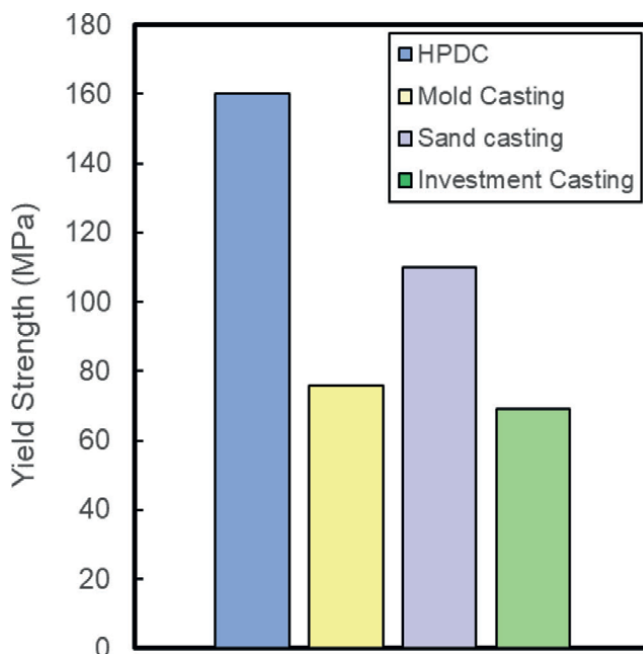
Figure 2.
Comparison of the yield strength of AZ91 fabricated by four different processes [22, 25].

2. Applications of HPDC magnesium alloys

2.1 Traditional applications

Increasing attention has been paid to replace steel and aluminum structural components with magnesium alloys on traditional internal combustion engine (ICE) vehicles in the past several decades. HPDC magnesium alloys have seen a number of these applications. Cost-economic AM50, AM60, AZ91 and AE44 magnesium alloys with excellent castability are most used to manufacture automotive components through the HPDC process. The criteria for component material selection are based on the alloy properties and component service environment.

Figure 3 shows the mechanical [25–27] and corrosion properties of conventional HPDC magnesium alloys and HPDC aluminum alloy A380. The magnesium alloys have comparable yield strength with A380 and similar or better elongations. The mass gains of the as-cast alloys were measured by Meridian Lightweight Technologies at several intervals during salt spray testing (SST) as per ASTM B117 for 1000 hours, to evaluate corrosion properties. It was noted that magnesium alloys AM60B, AZ91D and AE44 showed better corrosion resistance than HPDC A380 aluminum alloy. Based on these properties, the AE44 alloy with high strength and ductility at high temperature is typically used in elevated temperature environments, the AZ91D alloy is selected for high strength, good corrosion resistance and moderate temperature applications, and AM50A/AM60B alloys are utilized where high ductility is required in normal atmospheres.
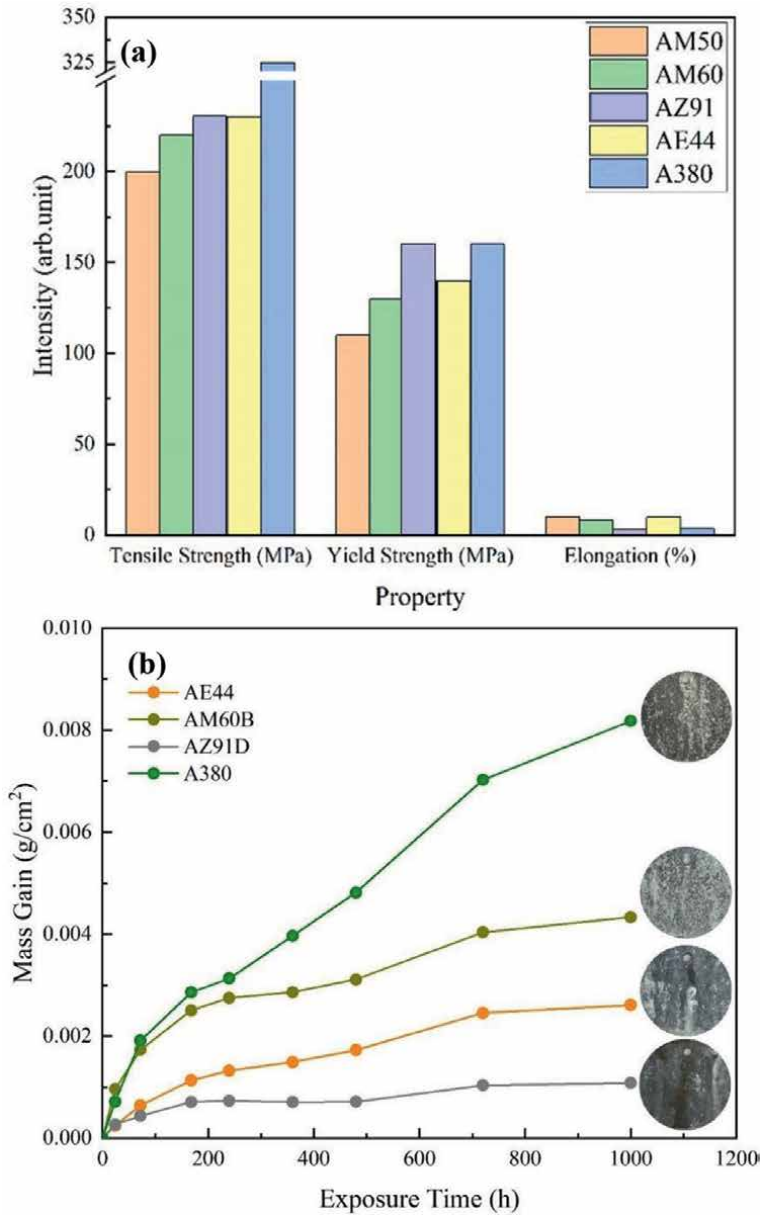
Figure 3.
Mechanical and corrosion properties of conventional HPDC magnesium alloys: (a) mechanical properties [25–27] and (b) salt spray test for 1000 hours conducted by Meridian lightweight technologies.

2.1.1 Interior applications

Magnesium alloy die castings have been widely utilized in interior automotive applications where minimum general corrosion resistance is required. Instrument panel (IP) or cross-car beam (CCB) is one of the earliest interior applications of magnesium alloys in the automotive industry which has been remarkably advanced owing to mass saving requirements in the past two decades. The first and largest die-cast

magnesium IP (~12.5 kg) with a wall thickness of ~4 mm was developed by General Motor in 1961 to replace a previous steel IP, which achieved ~25% weight saving [21]. With the optimization of materials and designs, the wall thickness of HPDC magnesium component has been dramatically reduced which has further improved the mass saving efficiency. State-of-the-art one-piece thin-walled cross-car beams can be cast in weights as low as 3 ~ 5 kg.

Figure 4 shows the evolution of the HPDC AM60B magnesium CCB on Jaguar Land Rover (JLR) S-type vehicle from 1998 to present [28]. The initial CCB in **Figure 4(a)** was made of steel which was replaced by the first-generation AM60B magnesium alloy in 2002 ~ 2007 model with a part weight of approximately 5.2 kg. The second-generation was then developed for the model year 2008 XF vehicle with a weight of approximately 5.7 kg and additional contents. With the optimization of design and casting wall thickness, the weight of the third-generation magnesium CCB was reduced to approximately 3.6 kg without decreasing the safety requirement. Although magnesium CCBs have been commonly used in North America and Europe, its application in China market is limited. Hybrid CCB assemblies composed of a half magnesium alloy beam on the driver side and half steel beam on the passenger side were developed on 2017 SAIC Motor Roewe i6, 2019 SAIC Motor Roewe ei5, 2018 NIO ES8 and 2020 BYD Han. These half magnesium CCBs usually have a total width of less than 1 m and weigh 2 ~ 4 kg. There is a significant opportunity to grow the magnesium alloy for one-piece CCB application in China to help meet the mass saving requirements as described in the 2020 Energy-saving and New Energy Vehicle Technology Roadmap 2.0 [29].

Seat frame is another important application of magnesium alloys in the interior automotive. The first concept of using magnesium seatback frame and cushion was demonstrated by Mercedes-Benz AG by using AM50 and AM20 alloys with a total weight ~ 8.5 kg about three decades ago [30]. Several studies and developments were reported on expanding the application of magnesium alloys for seat frames [31–35]. The state-of-the-art magnesium seatback and cushion are found with thinner wall thickness and less weight than before and are more widely utilized on vehicles. **Figure 5(a)** shows the 2014 Chevrolet Corvette Stingray AM60B magnesium backseat with a weight of 1.5 kg which demonstrates greater specific strength than the steel frame it replaced. The side bolsters provide a more supportive and
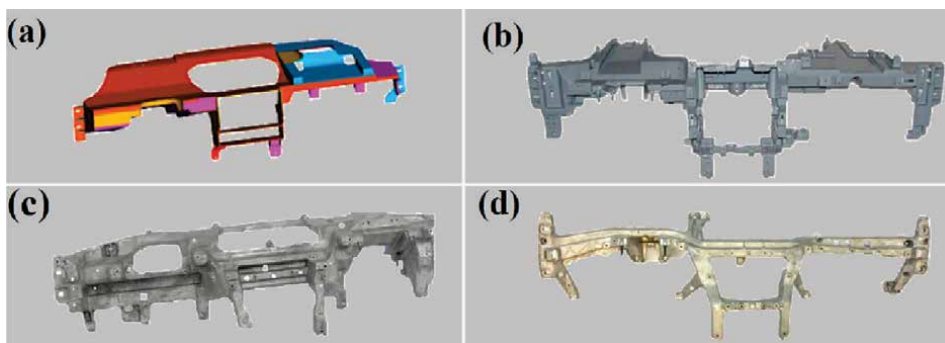
Figure 4.
Evolution of jaguar land rover (JLR) cross car beams (CCB): (a) jaguar S-type 1963 initial design (1998); (b) first-generation magnesium CCB (2002 ~ 2007 jaguar S-type X202); (c) second-generation magnesium CCB (2008–2015 jaguar XF X250) and (d) third-generation magnesium CCB (2015-present XF X260) [28].
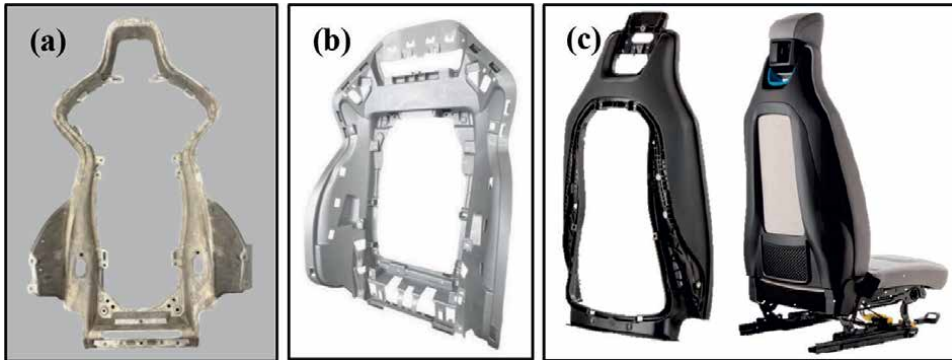
Figure 5.
Images showing backseat applications: (a) 2014 Chevrolet corvette seatback (courtesy of GM); (b) 2015 Mercedes-Benz SLK seatback [37] (courtesy of GF casting solutions) and (c) 2014 BMW i3 seatback [38] (courtesy of BASF).

comfortable seat frame on the competition sport model [36]. **Figure 5(b)** shows the 2015 Mercedes-Benz SLK AM50 magnesium seat which demonstrates a 30% weight saving and received the 2015 "Automotive Cast Design Product" Award of Excellence at the International Magnesium Association (IMA) 72nd Annual World Magnesium Conference [37]. Manufacturing a seatback frame with one-piece HPDC magnesium alloy can have advantages over injection molding using fiber reinforced composite which is another alternative solution for lightweighting. **Figure 5(c)** shows the 2014 BMW i3 back seat made through injection molding using PA66 with long glass fiber by BASF [38]. The plastic seat frame has a weight of 2.3 kg which does show weight reduction over the steel frame it replaced but requires another 2 kg steel reinforcement recliner to maintain strength [38].

Automotive steering wheels made by magnesium alloys AM40B and AM60B have been used since 1987 by Honda Motor [39]. Toyota Motor Corp. also reported the development of a one-piece HPDC AM60B magnesium steering wheel in 1991 [40, 41] which saved approximately 45% weight than the previous steel one. More recently, magnesium steering wheels made of both AM50 [42] and AM60 [43] are widely used in Europe and Asia.

Figure 6 depicts additional automotive interior applications of HPDC magnesium alloys. **Figure 6(a)** shows a HPDC AZ91D Bose audio amplifier made by Twin City Die Casting for automotive application which was awarded the 2014 North America Die Casting Association (NADCA) International Die-Casting Award for Magnesium Over 0.5lbs [44]. The audio amplifier weighs about 0.5 kg and provides both efficient weight saving and good heat dissipation. **Figure 6(b)** and **(c)** illustrates the HPDC AM60 display bracket and steering column manufactured by Meridian Lightweight Technologies. **Figure 6(d)** and **(e)** demonstrates the AM50 front and back center console on Audi A8 [37] and AM60 center stack on JLR Defender manufactured by GF Casting Solutions [45].

Another recent interior application of HPDC AM50A magnesium alloy is the rear support bracket (RSB) manufactured by Meridian Lightweight Technologies in the 2022 Mercedes-AMG SL Roadster as shown in **Figure 7**. This application was awarded the 2022 Automotive Cast Product IMA Award of Excellence at the 79th Annual World Magnesium Conference [46]. Each bracket weighs about 1.9 kg and provides Mercedes-AMG with the most economic weight saving. The bracket was
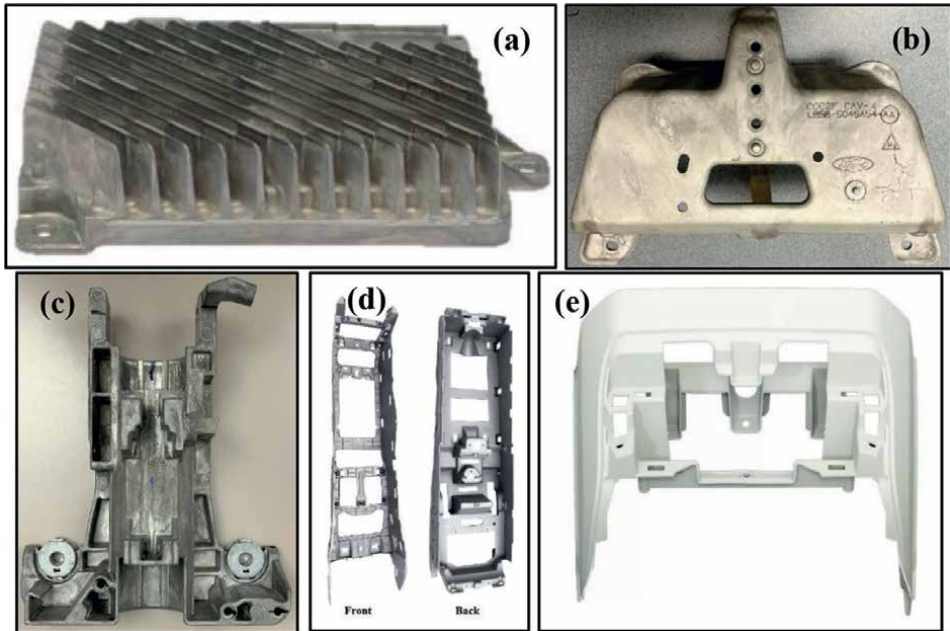
Figure 6.
Images showing interior applications of HPDC magnesium alloys: (a) AZ91D automotive audio amplifier cast by Twin City die casting company [44]; (b) AM60 display bracket on 2021 ford explorer; (c) AM60 steering column cast by Meridian lightweight technologies; (d) AM50 center console on Audi A8 and (e) AM60 center stack on JLR defender [45] (courtesy of GF casting solutions).

Figure 7.
AM50 left hand (LH) and right hand (RH) rear support brackets on 2022 Mercedes-AMG SL roadster cast by Meridian lightweight technologies [46].

able to improve vehicle strength and stiffness, provide spaces for airbags and seatbelt anchorages, contribute to the entire vehicle rigidity improvement and support the second-row backseats. It successfully helped Mercedes-AMG to re-introduce the "2 + 2" seating concept as a standard model. Overall, more efforts are being made to

replace interior automotive components with magnesium alloys which demonstrate efficient weight reductions and part consolidation.

2.1.2 Body applications

The concept of utilizing magnesium alloys for automotive body applications was developed about three decades ago and has been significantly scaled up in the recent years. Die-casting roof frames have been used on the Chevrolet C5 Corvette starting in 1997 and again on the Cadillac XLR two passenger roadster since 2003 [21]. The HPDC magnesium radiator support (MRS) was launched by Meridian Lightweight Technologies and Ford Motor Company for the 2004 Ford F-150 truck which was the first ever magnesium front-end application [47]. **Figure 8(a)** shows the overview of the first-generation MRS in 2004. The MRS was made from AM50A magnesium alloy which was assembled with EG60 steel bridging brackets. To minimize the galvanic corrosion between steel and magnesium, several corrosion prevention strategies were
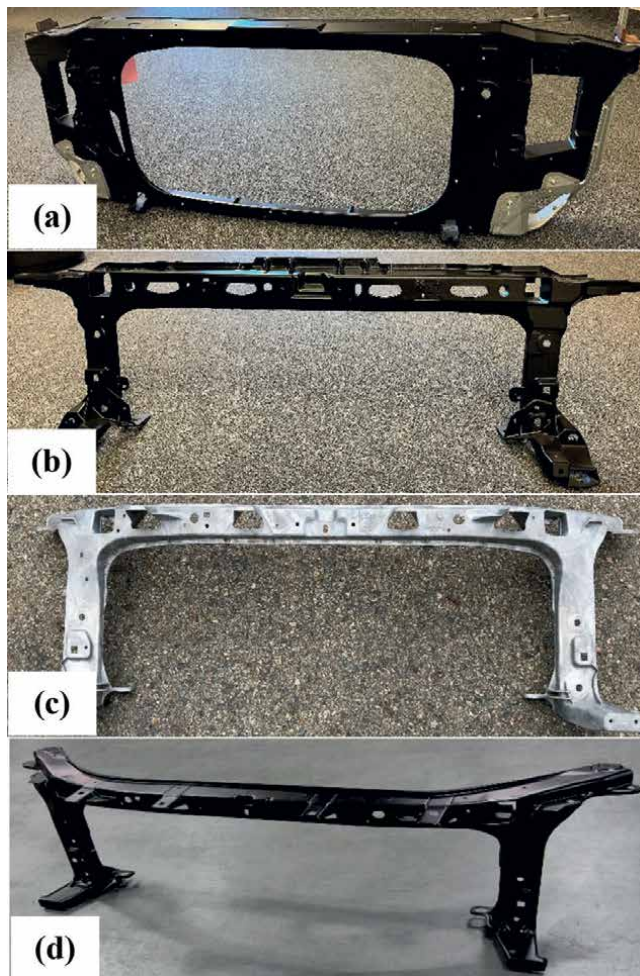
Figure 8.
Evolution of ford F-150 AM50A magnesium radiator support (MRS): (a) 2004 model; (b) 2009 model, (c) and (d) 2017 model before and after coating.

developed including redesigning the casting and brackets, applying chemical conversion coating and powder coating on magnesium, utilizing 5000 series aluminum spacers and nylon-coated bushings to avoid galvanic contact between magnesium and steel and using zinc electroplated fasteners [47]. The MRS casting design was evaluated through extensive component performance tests at Fords Arizona Proving Ground (APG). **Figure 8(b)–(d)** shows the second- and third-generation MRS castings developed in 2009 and 2017. All three generation castings have similar functionalities; however, significant mass reductions were achieved through optimization of material design and nominal wallstock reductions. The first-generation MRS (11.3 kg) saved 35% weight by replacing the original steel front end in 2004, and the third generation resulted in a mass reduction of 75% compared to the original steel design.

The Chrysler Dodge Viper SRT10 front of dash (FOD) launched in 2003 was the largest single piece of magnesium die casting for automotive body structural application [48]. The one-piece AM60B magnesium casting is assembled with three steel stampings to replace 51 individual assembled stamped steel pieces, achieving a weight reduction of 52%. The magnesium FOD implementation provided OEMs and Tier 1 suppliers with design and manufacturing flexibility and was awarded the 2002 Automotive Cast Product IMA Award of Excellence at the 59th Annual World Magnesium Conference.

A spare tire carrier (STC) component is another application of magnesium alloys for body structures implemented in 2006 [49]. A powder coating or over-molding outer layer has been applied on the STC to improve cosmetic corrosion resistance, as well as scratch and UV degradation resistance [50]. **Figure 9** shows the evolution of the Jeep Wrangler STC from 1996 to current model. The STC on 1996 ~ 2006 TJ model was made of three welded stamping steel parts assembled with a thermoplastic center high mounted stop lamp (CHMSL) which has a total weight of 5.3 kg (**Figure 9(a)**) [51]. **Figure 9(b)** shows the first magnesium STC on the 2007 ~ 2018 JK model which achieved a weight reduction of 65% and a cost saving over the previous steel STC [51]. The HPDC process also showed its advantages by integrating the carrier part with the CHMSL part together which further saved assembly and tooling cost. The casting made of AM60B magnesium alloy and a steel tether was added to provide enough strength for rear impact loading. Furthermore, powder coating, plastic washers/isolator and E-coated fasteners were utilized to enhance abrasion and corrosion performance [51].
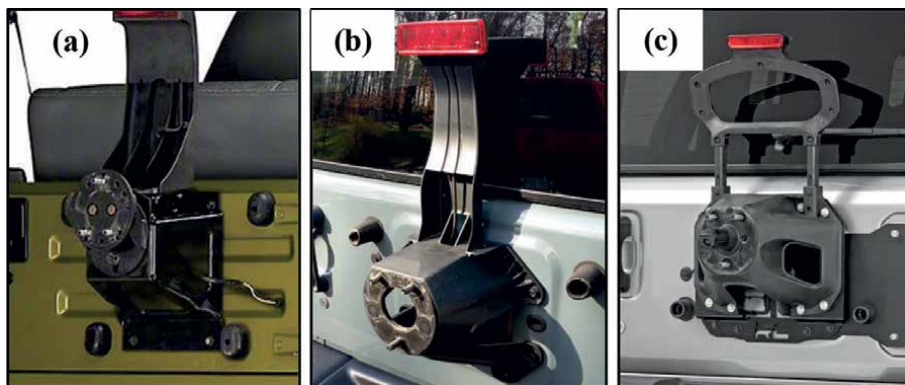
Figure 9.
Evolution of jeep wrangler spare tire carrier (STC): (a) first generation on 1996 ~ 2006 model; (b) second generation on 2007 ~ 2018 model and (c) third generation on 2018 ~ present model.

The STC on 2018 ~ present JL model is made of thixomolding AM60B magnesium alloy with Nylon 66 over molding as shown in **Figure 9(c)** [50]. The STC is designed wider to accommodate two air exhausts and has a weight of 3.1 kg. Although the third-generation STC increases its load capacity from 38 kg to 52 kg over the second generation, it adds an assembly step as a dual post plastic CHMSL, a separate component from the STC.

The first application of magnesium HPDC alloys in liftgate or hatchback inner was reported by Volkswagen Group on a 3 Liter car (3 L/100 km) Lupo TDI in 2000 [52]. The AM50A magnesium alloy inner, cast in a 3300 T die-cast machine was coupled with an aluminum outer to produce an assembly weighing 2.8 kg, resulting in a weight saving of nearly 50% compared to the steel version. Several years later, Mercedes-Benz also developed a HPDC magnesium alloy liftgate inner for the 2009 Mercedes E-class S212 T-model [53]. The 7.1 kg liftgate inner was high-pressure die cast in a 4200 T cast machine using AM50 magnesium alloy. The magnesium liftgate inner (1.4 m × 1.1 m with 2 ~ 5 mm thick) was e-coated and powder coated and then roll seamed and adhesive bonded with an AC170 aluminum outer. The entire assembly achieved 32% mass saving compared to the previous steel design. In the following year, Ford reported the first North American magnesium liftgate inner (1.38 m × 1.315 m) on the 2010 Lincoln MKT which was the largest magnesium liftgate at that time [54–56]. The final casting not only reduced the total weight by 40%, but also improved design flexibility and significantly decreased assembly time by replacing six stamped steel pieces into one integrated casting. The utilization of magnesium as rear gate inner was then significantly expanded [57, 58], and the latest examples are the liftgate inner on 2017 Chrysler Pacifica which achieved a mass reduction of nearly 50% [51, 57] and the 2018 JL swing gate [51].

A magnesium side door inner was firstly reported by Mercedes-Benz on CL-class coupe in 1999 [59] and SL-class in 2000 [60] using HPDC AM50 magnesium alloy. The utilization examples of magnesium cast door inners grown in luxury vehicles are a Ford magnesium door inner prototype project [61], the 2004 Aston Martin DB9 side door inner [62], the 2017 Aston Martin Vanquish S side door inner [58] and the GM integrated side door inner panel R&D project [63]. Some of the latest body structure applications of HPDC magnesium alloys include the door inner upper beltline reinforcement on the 2020 Chevrolet Corvette [63] and a convertible roof top on the 2013 Opel Cascade Cabrio [64].

2.1.3 Powertrain applications

The first utilization of magnesium alloys in the automotive industry was actually for engine piston application in the early 1900s using Dowmetal alloys and was proved to have similar strength and performance as aluminum in the 1921 Indianapolis 500 racing competition [65]. The first die-casting magnesium piston was made by Elektronmetal GmbH (a subsidiary of Mahle GmbH) in 1925 which was manufactured in high-volume applications ranging from commercial vehicle to submarine engines. Magnesium alloys for air-cooled powertrain applications such as pistons, engine blocks and gearboxes were extensively used in the production of the Volkswagen Beetle in 1938 and Transporter in 1949 [66]. However, utilization of magnesium alloy for powertrain applications was reduced due to increasing engine operating temperature and loading in the 1960's when air-cooling engines were replaced with water-cooling. The use of magnesium alloys was restricted due to the corrosion performance of the alloy compositions available at the time and creep

performance at the elevated engine operating temperatures. Many efforts were then taken to enhance the corrosion and creep properties of magnesium alloys including limits on impurities in alloy compositions, alloying such as rare earth (RE) element additions [67] and using hybrid designs.

In the last several years, magnesium alloy AZ91D with limits on impurity elements and RE-containing magnesium alloy AE44 have been widely used for powertrain applications. A HPDC AE44 magnesium engine front cover was used for the 2012 Porsche G1 Panamera and 2011 E2 Cayenne models with a weight of approximately 2.1 kg that achieved a 45% weight reduction over the aluminum cover it replaced [45]. A HPDC AE44 oil conduit module was manufactured by GF Casting Solutions and used on the Porsche Panamera as shown in **Figure 10(a)** [68]. The first ever magnesium oil conduit module had a weight of 4.6 kg resulting in a 24% weight saving from the previous aluminum one. **Figure 10(b)** shows the AZ91 gearbox housing utilized on Volkswagen Golf and Passat models which has a weight of 6.8 kg. **Figure 10(c)** and **(d)** shows the AZ91 transfer and transmission cases manufactured by Meridian Lightweight Technologies. Some other powertrain components made by magnesium alloys have also been reported—an AE44 valve cover on the Porsche Panamera, an AJ62 composite crankcase on the BMW 630 Ci [69] and an ACM522 magnesium oil pan used on Honda vehicles [70].

2.1.4 Chassis applications

A HPDC magnesium alloy chassis application was first reported on the 2006 GM Chevrolet Z06 Corvette with an engine cradle application [32, 69, 71]. The engine cradle was made of AE44 magnesium alloy and had a weight of 10.5 kg, resulting in a weight saving of 35% compared to an aluminum design. The magnesium engine cradle was used to support the engine and front bumper beam and functioned as a
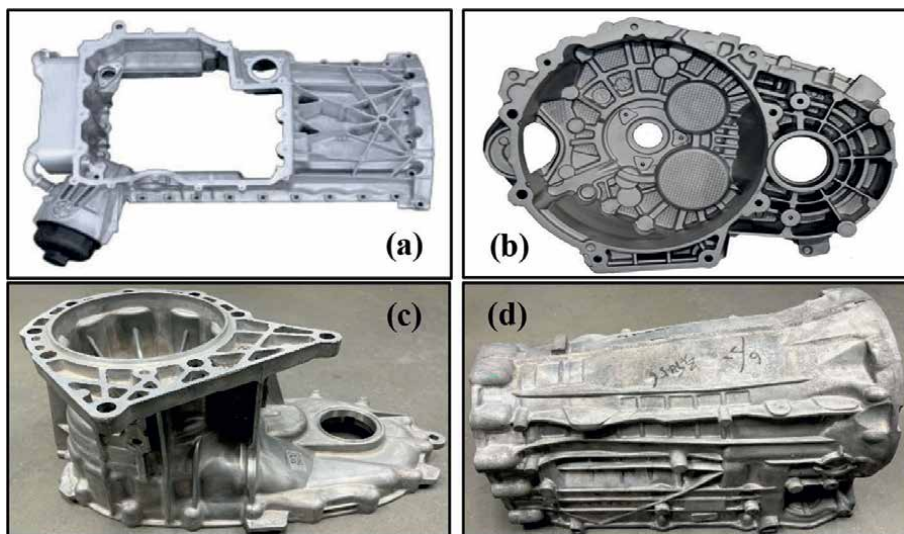
Figure 10.
Powertrain applications of HPDC magnesium alloys: (a) AE44 oil conduit module on Porsche Panamera [48] (courtesy of GF casting solutions) and (b) AZ91 gearbox on Volkswagen golf and Passat [45] (courtesy of GF casting solutions); (c) AZ91 transfer case on ford F-150 and (d) AZ91 transmission case prototype made by Meridian lightweight technologies.

mounting point for several front suspension components. An R&D project demonstrating the feasibility of an HPDC AE44 subframe is another example of magnesium alloys for chassis application [72–74]. The subframe integrated 15 steel stamping parts into a one-piece die casting which had a weight of 15.6 kg that achieved a weight saving of 32%. The subframe connected with other front suspension systems is located underneath the vehicle and is generally exposed to severe corrosive environment conditions such as water, salt and dirt. Therefore, a couple of galvanic corrosion prevention strategies such as aluminum spacers and coated fasteners were investigated through Ford proving ground and lab accelerated corrosion tests [73]. Magnesium wheels are also reported on racing vehicles and roadsters although mainly manufactured through forging process [24, 75, 76]. A die-cast AM60 magnesium wheel was used for the 2015 Yamaha YZF-R1 motorcycle which improved the vehicle maneuverability and handling stability [77]. The advantages and disadvantages of using magnesium automotive wheels were also investigated [78–80]. However, the high cost and corrosion concerns of magnesium alloys restrict their application on automotive wheels. Furthermore, porosity in HPDC components is a safety concern for magnesium cast wheels. The application of HPDC magnesium alloys for automotive chassis application is limited and requires further investigation.

2.1.5 Other automotive applications

Other HPDC magnesium alloy applications in the automotive industry have also been reported. A magnesium AE44 alloy strut tower brace was utilized on the 2020 Ford Mustang Shelby GT500 [81–84]. **Figure 11** shows the evolution of the strut tower brace. The magnesium strut tower brace weighs 3.6 kg and integrates the previous stamped steel and extruded aluminum pieces into one die casting part which achieved a 46% mass reduction. Several coating options were evaluated through Ford's L-467 cyclic corrosion testing (CCT). The resulting production intent coating chosen was a ceramic-based pretreatment and UV-compatible powder coating, while anodized aluminum washers were used for galvanic corrosion prevention [83].
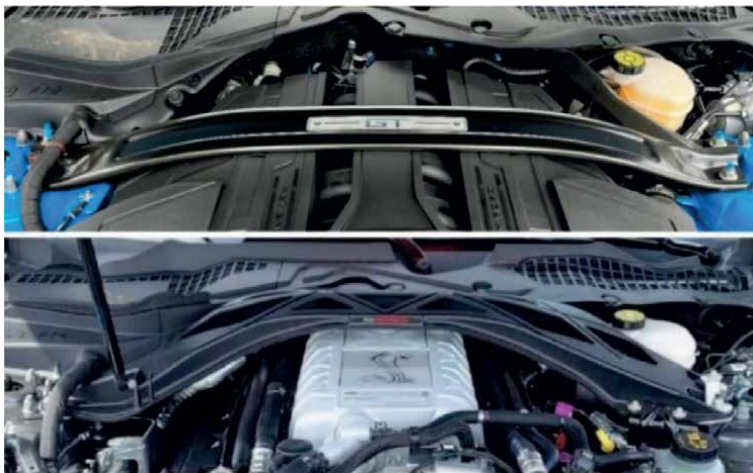
Figure 11.
Evolution of ford mustang GT strut tower mount: (top) steel stamping and aluminum extrusion strut tower mount and (bottom) HPDC magnesium strut tower brace manufactured by Meridian lightweight technologies.

A recent new magnesium die-cast alloy was developed using Mg-Al-Zn-Mn composition which is intended for structural applications [85]. The magnesium alloy chemical composition was tailored to 4 ~ 5% Al and 0.4 ~ 1.2% Zn which demonstrates competitive castability, strength and ductility with conventional AM50 and AM60 magnesium alloys. Other HPDC magnesium automotive applications such as the AM60 JLR Defender driver/passenger side, AM60 JLR left/right hand endcap [45] and 2022 Cadillac CT4-V/CT5-V paddle shifter [86] demonstrate versatile applications in the automotive industry.

2.2 Current EV applications

With recent developments in EV technologies, increasingly more internal combustion engine (ICE) powertrains are being replaced by hybrid, plug-in hybrid and battery electric vehicles. Decreasing the vehicle weight and increasing the battery pack power are two of the primary methods of extending the EV driving range. Therefore, switching existing magnesium components from traditional ICE to EV applications and developing more battery-related magnesium components become significantly important. The majority of HPDC magnesium alloy structural applications are transferrable to EV architectures as much of the body structure of these vehicles is very similar. For instance, an AM60 magnesium CCB is found on Ford's first EV, the 2021 Mustang Mach-E model [87]. An AM60B magnesium front-end carrier was also utilized on the 2013 Tesla Model S sedan, and an AM50 magnesium upper door frame was used on the Tesla Model X made by GF Casting Solutions [88]. The magnesium interior applications like seatback, display bracket, side/back door inner, center console, steering column and many other components are basically same on ICEVs and EVs. Therefore, it is reasonable to expect that more utilizations of those components cast using traditional AM and AZ alloys will be reported.

In newly developed EV-specific applications, an AZ91D onboard charger housing is manufactured by Meridian Lightweight Technologies as shown in **Figure 12(a)** [89–91]. The two-piece magnesium charger housing replaces the previous two-piece aluminum component providing a 25% weight reduction. The charger housing was the first ever HPDC magnesium application in a battery-related component in the EV automotive industry. A prototyped magnesium battery tray is also reported by FUSIUM for automotive applications as shown in **Figure 12(b)** but was not in large-scale production [92].
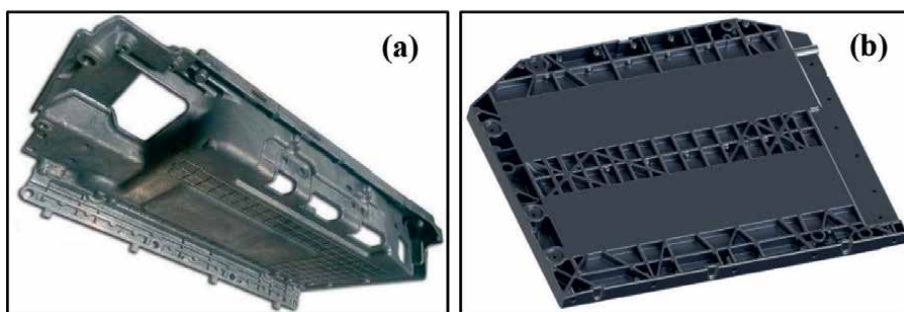
Figure 12.
Battery-related application of magnesium alloys: (a) HPDC AZ91D battery charger housing manufactured by Meridian lightweight technologies [89] and (b) prototyped battery tray [92] (courtesy of Fusium).

Although traditional Mg-Al cast alloys can be utilized to make structural components for EVs, numerous automakers value thermal conductivity properties for battery-related applications. A battery housing application typically requires a lightweight design with the capability for small temperature variations to optimize the battery operations—otherwise known as excellent heat dissipation and thermal conductivity. The conventional cast Mg-Al alloys have relatively low thermal conductivities. **Figure 13** shows the influence of aluminum content of magnesium alloys on the thermal conductivity of magnesium alloys. The experimental thermal conductivities of Mg-Al alloys compare well with the PANDAT simulation results. The addition of RE elements results in improved thermal conductivity compared with the PANDAT predictions aluminum content predictions. For example, DSM-1 alloy developed by Dead Sea Magnesium has a similar thermal conductivity with HPDC aluminum A380 [85]. It is expected that this alloy will have an enormous potential for EV applications owing to its favorable die castability, as well as mechanical and thermal conductivity properties.

Extensive studies and evaluations were conducted to improve the thermal conductivity of traditional Mg-Al alloys through alloying elements like Al [93–96], Zn [94, 97–100], Mn [94, 97], Sn [97, 101], Zr [97], Ca [97, 102, 103], Si [103, 104], Li [101], Sr. [102] and RE elements like Sc [105], Y [106–108], Gd [106, 107, 109], Ce [108, 110–114], La [113, 115, 116], Nd [113, 117] and Sm [108, 113]. The influence of chemical composition, second phase, microstructure, texture and casting processes on the thermal conductivity of magnesium alloys has been discussed in these studies. All alloying elements act to reduce the thermal conductivity from that of pure magnesium. The solute of elements in α-magnesium will distort the original lattice structure, form second phase and act as scattering points for electrons and phonons during thermal transportation. Therefore, the past ways for increasing the thermal conductivity of alloys are mainly focused on minimizing the solute of atoms and fraction of second phase [118]. It was also reported that the thermal conductivity of magnesium alloys is affected by solute
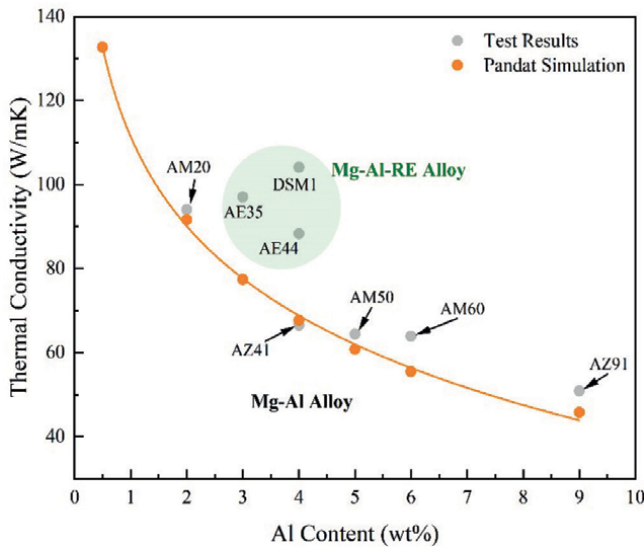
Figure 13.
Influence of aluminum content on thermal conductivity of magnesium alloys: Comparison results from PANDAT simulation and tests on Mg-Al and Mg-Al-RE alloys.

atoms while the second phase only shows very slight effects [108, 109, 117]. Therefore, selecting an alloying element with low solubility in magnesium is critical to improving the thermal conductivity of a magnesium alloy.

Figure 14 shows the solubility of several RE elements in magnesium alloys. The elements La and Ce have relatively low solubility in magnesium and are expected to contribute greater to improving thermal conductivity of a magnesium alloy, e.g., DSM-1. Several other magnesium alloy compositions were also developed using lab scale HPDC machines [119–123] which showed excellent thermal conductivities and good die castability. The Mg-4Al-4Zn-4RE-1Ca magnesium alloy was reported to have good castability for thin-walled components with a thermal conductivity of 94.4 W/mK and desirable mechanical properties (YS = 185 MPa, UTS = 233 MPa and elongation = 4.2%) [121]. The Mg-3RE-0.5Zn alloy is reported to also have good castability, a thermal conductivity of 133.9 W/mK and good mechanical properties (YS = 153 MPa, UTS = 195 MPa and elongation = 4.3%) [122]. Finally, the Mg-4La-2.5Al-0.5Mn alloy with a thermal conductivity of 106.5 W/mK and good strength and ductility (YS = 149 MPa, UTS = 253 MPa and elongation = 11.5%) was reported to have favorable castability as well [103]. However, the evaluation of the castability of these alloys with larger scale die-casting machines is needed upon further consideration in EV applications.

2.3 Aerospace applications

The use of magnesium cast alloys in aerospace applications started as early as the 1930s and peaked two decades later. Several prototype aircrafts were developed containing magnesium, including the XP-56 Black Bullet by Northrop Corporation, with
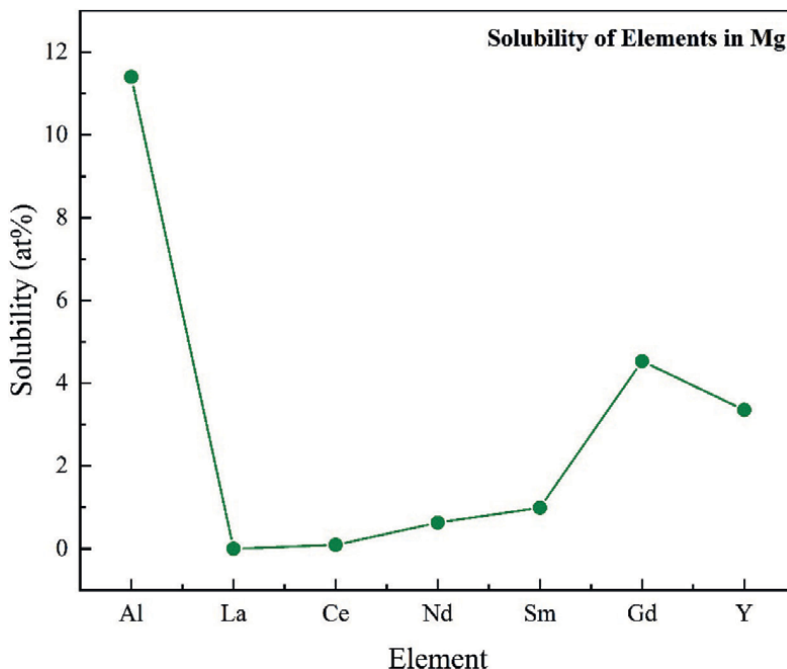
Figure 14.
Solubility of selected RE elements in magnesium [107, 108, 113, 114].

a magnesium airframe and welded skin in 1943, the F-80C (47–171) by Lockheed and the Convair XC-99 by US Air Force [124]. A large volume of magnesium alloy was also found on other aircrafts like the Convair B-36 (~8600 kg), the Boeing B47 (5500 kg), the Soviet Union TU-95MS (1550 kg), the Tupolev TU-134 (780 kg) and the Sikorsky S-56 (115 kg) [125]. Several magnesium cast components were reported on aircrafts, including an AZ92A thrust reverser cascade on the Boeing 737, an EZ33A gearbox on a Rolls Royce and a ZE41 transmission casing on a Sikorsky S92 [124, 126].

However, corrosion and flammability issues restricted further development of magnesium components utilized in the aerospace industry as the use of magnesium components dropped by 95% in mass from the 1966 Tupolev TU-134 to the 1991 TU-304 model [125]. Further, the use of magnesium in aerospace applications was banned in 2005, according to the SAE standard AS8049B. More recently, as the magnesium industry has advanced and with a high demand of lightweighting in the aerospace industry, more attention has been paid to improve the magnesium alloy properties and re-introduce magnesium alloys back into aerospace in the last fifteen years. The Federal Aviation Administration (FAA) developed a flammability standard for magnesium material (FAA Chapter 25) in 2015. As a result, the SAE AS8048 standard was revised to reconsider the use of magnesium alloys in Revision C [127].

Several studies were conducted to improve the flammability resistance of magnesium alloys, mainly through alloying elements such as Al [10, 11], Be [128, 129], Ca [12–19] and REs [130–134]. The addition of Ca and REs are two of the most effective ways of strengthening the magnesium flammability resistance. Minimum addition of REs is well-known to enhance the oxidation resistance of magnesium alloys which can increase their flammability resistance. The FAA completed several tests on the WE43 alloy composition as per Chapter 25 and demonstrated that the flammability characteristics of WE43 were consistent with materials in production and qualified for aircraft interior applications [135]. Some other magnesium alloys that can pass FAA Chapter 25 testing were also reported [136]. However, those alloys are either too expensive or non-castable for large volume production using a HPDC process. Therefore, the focus of the major studies on improving the magnesium flammability resistance was on alloying using Ca which is a more cost-effective and potentially castable solution. The addition of Ca into magnesium alloy was firstly reported in 1911 [137] and was investigated for flammability and ignition resistance in 1924 [14]. Ca can be added to magnesium alloys either through adding pure Ca or calcium compounds like Al_2Ca [138], CaO [139–141] and $Ca(OH)_2$ [142]. The addition of Ca is reported to increase the magnesium flammability resistance through several mechanisms such as increasing the ignition temperature [128, 143], forming more thermal stable second Laves phases [16, 144] and modifying the oxide film [145, 146].

Here, we tested twelve existing magnesium alloys at Meridian Lightweight Technologies which included five Ca-containing alloys and seven non-Ca alloys as per FAA Chapter 25. **Figure 15** shows the testing results with the correlation of mass loss after testing and aluminum content in each alloy. With the additions of calcium above 0.6%, the flammability resistance of magnesium alloys is significantly improved. **Figure 15** also shows the typical cross-section appearance of alloys after FAA testing where the oxide film formed on Ca-containing magnesium alloy is much denser and smoother than the one without Ca.

Increasing the content of Ca is found to negatively affect the castability of magnesium alloys resulting in die sticking, hot tearing, sinks and cold shots [147]. The hot tearing tendency is increased by an elevated precipitation temperature of Al_2Ca addition into AZ91 which affects filling [148]. Ca additions are also reported
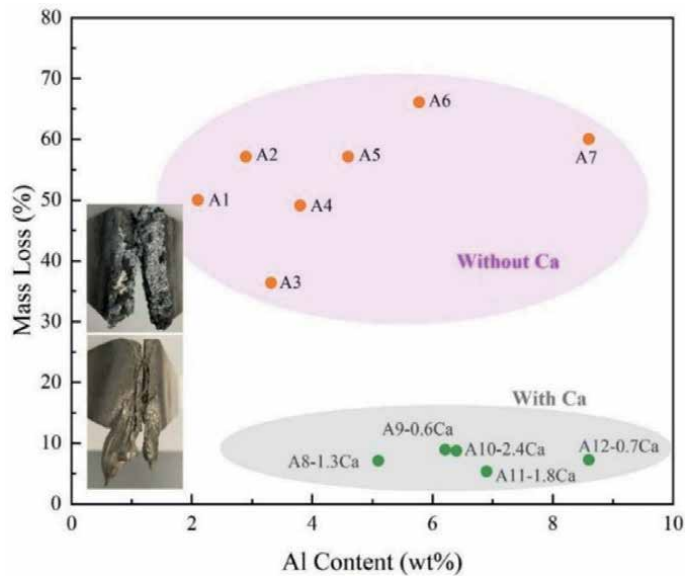
Figure 15.
Influence of alloying on mass loss of magnesium alloys tested as per FAA chapter 25 by Meridian lightweight technologies.

to promote the reaction between die steel and the magnesium melt that results in die sticking [140]. However, Ca-containing magnesium alloys have been reported to have a good combination of flammability resistance and castability through optimization of the alloy composition and casting processes [149–152]. The ZACE05613 magnesium alloy was used to produce transmission cases without hot tearing issues [149]. The Mg-Al-Mn-Ca-Si alloy AMXS6020 was also reported without castability issues [152]. Based on these studies, the development of cast alloys and processes with acceptable flammability resistance is expected to continue with a target for aerospace applications.

3. Conclusions

The applications and developments of HPDC magnesium alloys in the automotive and aerospace industry were reviewed. Attributed to the relatively low density, high strength, good ductility, tunable thermal conductivity as well as extraordinary advantage of greatly decreasing the number of parts and assembly compared to the steel counterparts, HPDC magnesium alloys have been widely used in automotive industry.

HPDC magnesium alloys, e.g., AM50/AM60 have been widely used for interior automotive applications, such as instrument panel (IP), cross-car beam (CCB) and seat frame. They have also been used for automotive body such as roof frames, magnesium radiator support (MRS), front of dash (FOD), spare tire carrier (STC), liftgate or hatchback inners and side door inners.

The powertrain applications of HPDC magnesium alloys started with gearboxes, engine pistons and blocks and were expanded to the use of AZ91D and AE44 which have favorable corrosion and creep properties and are suitable for oil conduits, gearbox house, transfer and transmission cases.

The structural applications of HPDC magnesium alloys are transferrable to EV architectures such as upper door frame and front-end carrier as well as interior applications including seatback, display bracket, side/back door inner, center console, steering column and many other components.

HPDC magnesium alloys also show high potentials for EV-specific applications including onboard charger housing and battery tray. More studies are ongoing to achieve a sweet combination of good castability and thermal conductivity.

The use of HPDC magnesium alloys in aerospace industry has shown prospective potentials with the improvement of the flame resistance of magnesium alloys through alloying elements, e.g., Ca which provides a cost-effective and potentially castable solution.

The future for magnesium alloy applications in these industries, we believe, is quite prospective as evidenced by the development of novel alloy systems combining excellent mechanical properties as well as application-specific tendencies, such as good thermal conductivity or flammability resistance. We foresee a strong market and bright future for magnesium alloys in the automotive as well as aerospace industries.

Author details

Sophia Fan, Xu Wang, Gerry Gang Wang and Jonathan P. Weiler*
Global Technical Center, Meridian Lightweight Technologies, Strathroy, ON, Canada

*Address all correspondence to: jweiler@meridian-mag.com

IntechOpen

References

[1] Calado LM, Carmezim MJ, Montemor MF. Rare earth based magnesium alloys—A review on WE series. Frontiers in Materials. 2022;**8**:1-18. DOI: 10.3389/fmats.2021.804906

[2] Wang GG, Bos J. A study on joining magnesium alloy high pressure die casting components with thread forming fasteners. Journal of Magnesium Alloy. 2018;**6**:114-120

[3] Dargusch MS, Easton MA, Zhu SM, Wang G. Elevated temperature mechanical properties and microstructures of high pressure die cast magnesium AZ91 alloy cast with different section thicknesses. Materials Science and Engineering A. 2009;**523**:282-288

[4] Sheng SD, Chen D, Chen ZH. Effects of Si addition on microstructure and mechanical properties of RS/PM (rapid solidification and powder metallurgy) AZ91 alloy. Journal of Alloys and Compounds. 2009;**470**:L17

[5] Dong X, Feng L, Wang S, Nyberg EA, Ji S. A new die-cast magnesium alloy for applications at higher elevated temperatures of 200-300°C. Journal of Magnesium and Alloys. 2021;**9**:90-101. DOI: 10.1016/j.jma.2020.09.012

[6] Zhu SM, Gibson MA, Nie JF, Easton MA, Abbott TB. Microstructural analysis of the creep resistance of die-cast Mg–4Al–2RE alloy. Scripta Materialia. 2008;**58**:477-480

[7] Su CY, Li DJ, Luo AA, Shi RH, Zeng XQ. Quantitative study of microstructure-dependent thermal conductivity in Mg–4Ce–xAl–0.5Mn alloys. Metallurgical and Materials Transactions A: Physical Metallurgy and Materials Science. 2015;**50A**:1970-1984

[8] Zhang JH, Liu K, Fang DQ, Qiu X, Yu P, Tang DX, et al. Microstructures, mechanical properties and corrosion behavior of high-pressure die-cast Mg–4Al–0.4Mn–xPr (x = 1, 2, 4, 6) alloys. Materials Science and Engineering A. 2009;**480**:810-819

[9] Zhang JH, Zhang DP, Tian Z, Wang J, Liu K, Lu HY, et al. Microstructures, tensile properties and corrosion behavior of die-cast Mg–4Albased alloys containing La and/or Ce. Materials Science and Engineering A. 2008;**489**:113-119

[10] Liu M, Shih DS, Parish C, Atrens A. The ignition temperature of Mg alloys WE43, AZ31 and AZ91. Corrosion Science. 2012;**54**:139-142. DOI: 10.1016/j.corsci.2011.09.004

[11] Kumar NVR, Blandin JJ, Suéry M, Grosjean E. Effect of alloying elements on the ignition resistance of magnesium alloys. Scripta Materialia. 2003;**49**:225-230. DOI: 10.1016/S1359-6462(03)00263-X

[12] Li F, Peh WY, Nagarajan V, Ho MK, Danno A, Chua BW, et al. Development of non-flammable high strength AZ91 + Ca alloys via liquid forging and extrusion. Materials and Design. 2016;**99**:37-43. DOI: 10.1016/j.matdes.2016.03.014

[13] Gneiger S, Gradinger R, Simson C, Kim M, You BS. Investigations on microstructure and mechanical properties of non-flammable Mg-Al-Zn-Ca-Y extruded alloys. In: 7th European Conference for Aeronautics and Space Sciences (EUCASS), Milano, Italia. Bruxelles, Belgium: The EUCASS Association; 2017. pp. 1-7. DOI: 10.13009/EUCASS2017-252

[14] Frank S, Gneiger S. Development of cost-effective non-flammable

magnesium alloys. Light Metal Age. 2017;**75**:54-56

[15] Yi S, Victoria-Hernández J, Kim YM, Letzig D, You BS. Modification of microstructure and texture in highly non-flammable Mg-Al-Zn-Y-Ca alloy sheets by controlled thermomechanical processes. Metals (Basel). 2019;**9**:181. DOI: 10.3390/met9020181

[16] Cheng C, Lan Q, Wang A, Le Q, Yang F, Li X. Effect of Ca additions on ignition temperature and multi-stage oxidation behavior of AZ80. Metals (Basel). 2018;**8**:766. DOI: 10.3390/met8100766

[17] Dvorsky D, Dalibor Vojtech JK, Vojtech D, Minárik P, Straska J. The effect of Y, Gd and Ca on the ignition temperature OF extruded magnesium alloys. Materials and Tehnology. 2020;**54**:669-675. DOI: 10.17222/mit.2019.284

[18] Prasad A, Shi Z, Atrens A. Flammability of Mg-X binary alloys. Advanced Engineering Materials. 2012;**14**:772-784. DOI: 10.1002/adem.201200124

[19] Cheng C, Lan Q, Liao Q, Le Q, Li X, Chen X, et al. Effect of Ca and Gd combined addition on ignition temperature and oxidation resistance of AZ80. Corrosion Science. 2019;**160**:108176. DOI: 10.1016/j.corsci.2019.108176

[20] Joost WJ, Krajewski PE. Towards magnesium alloys for high-volume automotive applications. Scripta Materialia. 2017;**128**:107-112

[21] Luo AA. Magnesium casting technology for structural applications. Journal of Magnesium Alloy. 2013;**1**:2-22. DOI: 10.1016/j.jma.2013.02.002

[22] ASTM B80-15, Standard Specification for Magnesium-Alloy Sand Castings, 2015

[23] ASTM B199-12, Standard Specification for Magnesium-Alloy Permanent Mold Castings, 2012

[24] ASTM B403-12, Standard Specification for Magnesium-Alloy Investment Castings, 2012

[25] ASTM B94-13, Standard Specification for Magnesium Alloy Die Castings, 2013

[26] Bakke P, Westengen H, Wang G, Jekl J, Berkmortel R. Die castability and property evaluation of AE alloys for drive train components. In: 13th Magnesium Automotive and End User Seminar. FH Aalen, Aalen, Germany: European Research Association for Magnesium; 2005

[27] ASTM B85-14, Standard Specification for Aluminum-Alloy Die Castings, 2014. doi:10.1520/B0085

[28] Fackler H. Magnesium cross car beam – 3 generations. In: 5th Annual Global Automotive Lightweight Material Supply, Design & Engineering. Eur., Birmingham: Global Automotive Lightweight Materials (GALM); 2015

[29] SAE-China, Energy-saving and New Energy Vehicle Technology Roadmap 2.0, 2020;1-64. Available from: http://www.sae-china.org/news/society/202010/3957.html

[30] Hector B, Heiss W. Magnesium die-castings as structural members in the integral seat of the new Mercedes-Benz roadster. In: SAE Tech. Pap. Warrendale, PA: SAE International; 1990-02-01. 1990. DOI: 10.4271/900798

[31] Brambilla S, Perotti P. Die casted magnesium front seat frame: An

application for small and medium size cars. In: SAE Tech. Pap. Warrendale, PA: SAE International; 1997-02-24. 1997. DOI: 10.4271/970323

[32] Gerard DA. Materials and process in the Z06 CORV. Advanced Materials and Processes. 2008;**166**:30-33

[33] Kim JJ, Han DS. Recent development and applications of magnesium alloys in the Hyundai and Kia motors corporation. Materials Transactions. 2008;**49**(5):894-897

[34] Wang S, Hu W, Gao Z, Tian P. The application of magnesium alloy in automotive seat design. Applied Mechanics and Materials. 2013;**395-396**:266-270

[35] Abate M, Willman M. Use of cast magnesium Back frames in automotive seating. In: SAE Tech. Pap. Warrendale, PA: SAE International; 2005-01-0723. 2005. pp. 91-98

[36] Cornett K. The Seating Options in the 2014 Corvette Stingray, CORVETTEBlogger.Com. (2013) 1-5

[37] D'Errico F, Tauber M, Just M. Magnesium alloys for sustainable weight-saving approach: A brief market overview, new trends, and perspectives. Current Trends in Magnesium (Mg) Research; 2022:1-33. DOI: 10.5772/intechopen.102777

[38] Caffrey C, Bolon K, Kolwich G, Johnston R, Shaw T. Cost-effectiveness of a lightweight design for 2020-2025: An assessment of a light-duty pickup truck. In: SAE Tech. Pap. Warrendale, PA: SAE International; 2015-01-0559. 2015. DOI: 10.4271/2015-01-0559

[39] R. Conroy, G. Exner, M. Shermetaro, Magnesium Steering Wheel, WO 94/16114, 1994

[40] Kawase Y, Shinto H, Yoshida T. Development of Magnesium Steering Wheel. Warrendale, PA: SAE International; 1991. DOI: 10.4271/910549

[41] Katsunobu S, Mikio K. Steering Wheel, US5070742. Alexandria, VA: United States Patent and Trademark Office (USPTO); 1991

[42] Marşavina L, Krausz T, Tamas Krausz L, Pîrvulescu LR. A methodology for durability of AM50 magnesium alloy steering wheels. Semantic Scholar. 2019;**64**:137-151

[43] Kim SK, Yoo HJ, Kim YJ. Research strategy for AM60 magnesium steering wheel. In: TMS Annu. Meet. Pittsburgh, PA: The Minerals, Metals and Materials Society (TMS); 2002. pp. 247-252

[44] North American Die Casting Association. International die casting design competition winner. Die Casting Congress & Tabletop. 2014;**2014**:63-81

[45] GF Casting Solutions. Innovative Products for you. Schaffhausen, Switzerland: GF Casting Solutions; 2019. pp. 1-83

[46] International Magnesium Association. 2022 IMA Awards of Excellence Showcase. St. Paul, MN: International Magnesium Association; 2022

[47] Balzer JS, Dellock PK, Maj MH, Cole GS, Reed D, Davis T, et al. Structural magnesium front end support assembly. In: SAE Tech. Pap. 2003-01-0186. Warrendale, PA: SAE International; 2003

[48] Riopelle L. Magnesium application. In: International Magnesium Association. Annu. Semin. Livonia; 2004

[49] International Magnesium Association. 2006 IMA Awards of Excellence. St. Paul, MN: International Magnesium Association; 2006

[50] Duke CJ. FCA US LLC-magnesium closures development. SAE Technical Papers. 2021:1-11. DOI: 10.4271/2021-01-0278

[51] Duke CJ, Logan SD. Lightweight magnesium spare Tire carrier. In: 64th Annu. World Magnes. Conf. St. Paul, MN: International Magnesium Association; 2007. pp. 75-80. DOI: 10.1107/s0021889891006921

[52] Schreckenberger H, Papke M, Eisenberg S. The Magnesium Hatchback of the 3-Liter Car: Processing and Corrosion Protection. Warrendale, PA: SAE Technical Papers; 2000. pp. 01-1123

[53] Blawert C, Heitmann V, Höche D, Kainer KU, Schreckenberger H, Izquierdo P, et al. Design of hybrid Mg/Al components for the automotive body - preventing general and galvanic corrosion. In: IMA 67th Annu. World Magnes. Conf. Hong Kong; International Magnesium Association; 2010. p. 9

[54] Automotive News PACE Awards, 2010-PACE Award Winner. 2010. Available from: https://www.autonews.com/awards/2010-winner-meridian-lightweight-technologies-inc-single-piece-cast-magnesium-liftgate-inner

[55] Inside L. International die casting design competition winners. Die Casting Engineering. 2010;**2010**:10-19

[56] American Foundry Society. GM Wins Funding to Develop Magnesium Diecasting Process, Mod. Cast. Schaumburg, IL: American Foundry Society; 2012. pp. 1-23

[57] Weiler JP, Sweet C, Adams A, Berkmortel R, Rejc S, Duke C. Next generation magnesium liftgate - utilizing advanced technologies to maximize mass reduction in a high volume vehicle application. In: International Magnesium Association 73rd Annual World Magnesium Conference. Rome: International Magnesium Association; 2016

[58] Weiler JP. A review of magnesium die-castings for closure applications. Journal of Magnesium Alloy. 2019;7:297-304. DOI: 10.1016/j.jma.2019.02.005

[59] New Car Test Drive, 2000 Mercedes-Benz CL-Class Review, New Car Test Drive. 1999. Available from: https://www.newcartestdrive.com/reviews/2000-mercedes-benz-cl-class/

[60] Kacher G. Mercedes-Benz SL500, Motortrend. 2001. Available from: https://www.motortrend.com/reviews/mercedes-benz-sl500-2/

[61] R.E. Bonnett, G. T. Bretz, P. Blanchard, S. Subramanian, Magnesium Door Assembly for Automobiles, US 2003/0188492 A1, Alexandria, VA: United States Patent and Trademark Office (USPTO); 2003

[62] Blanchard PJ, Bretz GT, Subramanian S, Devries JE, Syvret A, Macdonald A, et al. The application of magnesium die casting to vehicle closures. In: SAE Tech. Pap. Warrendale, PA: SAE International; 2005-01-0338. 2005. DOI: 10.4271/2005-01-0338

[63] Wang GG, MacKenzie K, Sweet C, Carter JT, O'Kane JC, Resch SA, et al. Development of a Thin-Wall magnesium automotive door inner panel. SAE International Journal of Materials and Manufacturing. 2020;**13**:199-208

[64] International Magnesium Association. 2013 IMA Awards of Excellence. St. Paul, MN: International Magnesium Association; 2013

[65] International Magnesium Association. IMA Awards of Excellence Winners, Mg Showc. St. Paul, MN: International Magnesium Association; 2012. pp. 1-4

[66] Friedrich H, Schumann S. The use of magnesium in cars - today and in the future. In: Int. Conf. Exhib. Magnes. Alloy. Their Appl. Wolfsburg: The Minerals, Metals and Materials Society; 1998. pp. 3-13

[67] Bronfin B, Moscovitch N. New magnesium alloys for transmission parts. Metal Science and Heat Treatment. 2006;**48**:479-486. DOI: 10.1007/s11041-006-0121-z

[68] International Magnesium Association. IMA AWARDS OF EXCELLENCE Design. St. Paul, MN: International Magnesium Association; 2014

[69] Beals RS, Tissington C, Zhang X, Kainer K, Petrillo J, Verbrugge M, et al. Magnesium global development: Outcomes from the TMS 2007 annual meeting. JOM. 2007;**59**:39-42. DOI: 10.1007/s11837-007-0102-8

[70] Koike S, Washizu K, Tanak S, Baba T, Kikawa K. Development of lightweight oil pans made of a heat resistant magnesium alloy for hybrid engines. In: SAE Tech. Pap. Warrendale, PA: SAE International; 2000-01-1117. 2000. pp. 1-9

[71] Merens N, NADCA. Competition rewards versatility and innovation. International Die Casting Design and Competition. 2006;**2006**:26-35

[72] Chen X, Wagner D, Heath G, Mehta S, Uicker J. Cast magnesium subframe development-bolt load retention. SAE Technical Papers. 2021:1-8. DOI: 10.4271/2021-01-0274

[73] Chen X, Wagner D, Wedepohl A, Redlin K, Mehta S, Uicker J. Cast magnesium subframe development-corrosion mitigation strategy and testing. SAE Technical Papers. 2021:1-7. DOI: 10.4271/2021-01-0279

[74] North American Die Casting Association. 2018 Die Casting Award Winner. In: 2018 NADCA Die Cast. Congr. Arlington Heights, IL: North American Die Casting Association; 2018. pp. 57-66

[75] Porsche Tequipmenrt. Exclusive Magnesium Wheels. 2021. Available from: https://dealer.porsche.com/za/johannesburg/en-GB/Accessories/Magnesium-Wheels

[76] Ceppos R. 2022 Cadillac V-Series Blackwings to Get Magnesium Wheels, Car Driv. 2020. Available from: https://www.caranddriver.com/news/a34536259/2022-cadillac-v-series-blackwing-magnesium-wheels/

[77] Yamaha Motor Co., Magnesium Die-Cast Wheels. (n.d.). Available from: https://global.yamaha-motor.com/business/cf/example/casting/ex011/

[78] Choudhary VS, Akram W, Yaseen JM, Saifudheen SM. Design and analysis of wheel rim with magnesium alloys (ZK60A) by using Solidworks and finite element method. International Journal of Automotive Technology. 2016;**1**:16-29

[79] Jiang X, Liu H, Lyu R, Fukushima Y, Kawada N, Zhang Z, et al. Optimization of magnesium alloy wheel dynamic impact performance. Advances in Materials Science and Engineering. 2019;**2019**:1-12. DOI: 10.1155/2019/2632031

[80] Frishfelds V, Timuhins A, Bethers U. Benefits of magnesium wheels for consumer cars. In: IOP Conference Series: Materials Science and Engineering. Philadelphia, PA: IOP Publishing; Vol. 355. 2018. pp. 1-9. DOI: 10.1088/1757-899X/355/1/012023

[81] North American Die Casting Association. 2021 Die Casting Award

Winners. In: 2021 Int. Die Cast. Compet. Arlington Heights, IL: North American Die Casting Association, Lexington; 2021. p. 55. DOI: 10.31399/asm.hb.v02a.a0006525

[82] American Foundry Society. Outstanding achievement-magnesium strut tower brace. In: Mod. Cast. Vol. 27. Schaumburg, IL: American Foundry Society; 2020

[83] Lazarz K, Cahill J, Ciccone TJ, Redlin K, Simko S. Corrosion performance of a magnesium tower brace. SAE Technical Papers. 2021:1-7. DOI: 10.4271/2021-01-0276

[84] Ciccone TJ, Kurane A, Delaney R, Ng S, Thai P, Hameedi J. Strut-Tower Brace, US10144456 B1. Alexandria, VA: United States Patent and Trademark Office (USPTO); 2018

[85] Wang GG, Weiler JP. Recent developments in high-pressure die-cast magnesium alloys for automotive and future applications. Journal of Magnesium Alloy. 2022;**11**:78-87

[86] Cadillac CT4-V Blackwing. NetCarShow.Com. (2022). Available from: https://www.netcarshow.com/cadillac/2022-ct4-v_blackwing/

[87] Foote B. 2021 Ford Mustang Mach-E Instrument Panel Analysis Reveals Mystery Space: Video, Ford Auth. 2021. Available from: https://doi.org/https://fordauthority.com/2021/07/2021-ford-mustang-mach-e-instrument-panel-analysis-reveals-mystery-space-video/

[88] 2016 AWARDS OF EXCELLENCE. Automotive Cast Product: Georg Fischer Automotive AG for Upper Door Frame. St. Paul, MN: International Magnesium Association; 2016

[89] American Foundry Society. Outstanding achievement - magnesium charger housing. In: Mod. Cast. Schaumburg, IL: American Foundry Society; 2022. p. 24

[90] North American Die Casting Association. 2022 industry awards casting winners - magnesium battery charger housing. In: 2022 Int. Die Cast. Compet. Arlington Heights, IL: North American Die Casting Association; 2022

[91] International Magnesium Association. 2021 IMA AWARDS OF EXCELLENCE for automotive - AZ91D magnesium charger housing for the Subaru Crosstrek plug-In hybrid. In: 2021 Int. Magnes. Assoc. Conf. St. Paul, MN: International Magnesium Association; 2021

[92] FUSIUM. Magnesium Alloy Battery Tray. n.d. Available from: https://fusium.ca/en/portfolio/battery-tray/

[93] Lee S, Ham HJ, Kwon SY, Kim SW, Suh CM. Thermal conductivity of magnesium alloys in the temperature range from −125 C to 400 C. International Journal of Thermophysics. 2010;**34**:2343-2350. DOI: 10.1007/s10765-011-1145-1

[94] Ying T, Chi H, Zheng M, Li Z, Uher C. Low-temperature electrical resistivity and thermal conductivity of binary magnesium alloys. Acta Materialia. 2014;**80**:288-295. DOI: 10.1016/j.actamat.2014.07.063

[95] Rudajevova OLA, Stanek M. Determination of thermal diffusivity and thermal conductivity of Mg-Al alloys. Materials Science and Engineering A. 2003;**341**:152-157

[96] Ying T, Zheng MY, Li ZT, Qiao XG. Thermal conductivity of as-cast and as-extruded binary Mg-Al alloys. Journal of Alloys and Compounds. 2014;**608**:19-24. DOI: 10.1016/j.jallcom.2014.04.107

[97] Pan H, Pan F, Yang R, Peng J, Zhao C, She J, et al. Thermal and electrical conductivity of binary magnesium alloys. Journal of Materials Science. 2014;**49**:3107-3124. DOI: 10.1007/s10853-013-8012-3

[98] Yuan J, Zhang K, Zhang X, Li X, Li T, Li Y, et al. Thermal characteristics of Mg-Zn-Mn alloys with high specific strength and high thermal conductivity. Journal of Alloys and Compounds. 2013;**578**:32-36. DOI: 10.1016/j.jallcom.2013.03.184

[99] Pan H, Pan F, Peng J, Gou J, Tang A, Wua L, et al. High-conductivity binary Mg-Zn sheet processed by cold rolling and subsequent aging. Journal of Alloys and Compounds. 2013;**578**:493-500. DOI: 10.1016/j.jallcom.2013.06.082

[100] Liu X, Wu Y, Liu Z, Lu C, Xie H, Li J. Thermal and Electrical Conductivity of as-Cast Mg-4Y-xZn Alloys. Philadelphia, PA: IOP Publishing; 2018

[101] Zhou X, Mo L, Du J, Luo G. Microstructure evolution and improvement of thermal conductivity in Mg–2Sn alloy induced by La addition. Journal of Materials Research and Technology. 2022;**17**:1380-1389. DOI: 10.1016/j.jmrt.2022.01.083

[102] Rzychoń T, Kiełbus A. The influence of rare earth, strontium and calcium on the thermal diffusivity of Mg-Al alloys. Defect and Diffusion Forum. 2011;**312-315**:824-829. DOI: 10.4028/www.scientific.net/DDF.312-315.824

[103] Zhou X, Guo T, Wu S, Lü S, Yang X, Guo W. Effects of Si content and Ca addition on thermal conductivity of As-cast Mg-Si alloys. Materials (Basel). 2018;**11**:2376-2387. DOI: 10.3390/ma11122376

[104] Rudajevová A, Lukáč P. Comparison of the thermal properties of AM20

and AS21 magnesium alloys. Materials Science and Engineering A. 2005;**397**:16-21. DOI: 10.1016/j.msea.2004.12.036

[105] Rudajevová A, Von Buch F, Mordike BL. Thermal diffusivity and thermal conductivity of MgSc alloys. Journal of Alloys and Compounds. 1999;**292**:27-30. DOI: 10.1016/S0925-8388(99)00444-2

[106] Yamasaki M, Kawamura Y. Thermal diffusivity and thermal conductivity of Mg-Zn-rare earth element alloys with long-period stacking ordered phase. Scripta Materialia. 2009;**60**:264-267. DOI: 10.1016/j.scriptamat.2008.10.022

[107] Zhong L, Peng J, Sun S, Wang Y, Lu Y, Pan F. Microstructure and thermal conductivity of As-cast and As-Solutionized Mg–rare earth binary alloys. Journal of Materials Science and Technology. 2017;**33**:1240-1248. DOI: 10.1016/j.jmst.2016.08.026

[108] Su C, Li D, Luo AA, Ying T, Zeng X. Effect of solute atoms and second phases on the thermal conductivity of Mg-RE alloys: A quantitative study. Journal of Alloys and Compounds. 2018;**747**:431-437. DOI: 10.1016/j.jallcom.2018.03.070

[109] Zhong L, Wang Y, Gong M, Zheng X, Peng J. Effects of precipitates and its interface on thermal conductivity of Mg–12Gd alloy during aging treatment. Materials Characterization. 2018;**138**:284-288. DOI: 10.1016/j.matchar.2018.02.019

[110] Peng J, Zhong L, Wang Y, Yang J, Lu Y, Pan F. Effect of Ce addition on thermal conductivity of Mg-2Zn-1Mn alloy. Journal of Alloys and Compounds. 2015;**639**:556-562. DOI: 10.1016/j.jallcom.2015.03.197

[111] Peng J, Zhong L, Wang Y, Lu Y, Pan F. Effect of extrusion temperature on the

microstructure and thermal conductivity of Mg-2.0Zn-1.0Mn-0.2Ce alloys. Materials and Design. 2015;**87**:914-919. DOI: 10.1016/j.matdes.2015.08.043

[112] Zhong L, Peng J, Li M, Wang Y, Lu Y, Pan F. Effect of Ce addition on the microstructure, thermal conductivity and mechanical properties of Mg-0.5Mn alloys. Journal of Alloys and Compounds. 2016;**661**:402-410. DOI: 10.1016/j.jallcom. 2015.11.107

[113] Guo H, Liu S, Huang L, Wang D, Du Y, Chu M. Thermal conductivity of As-cast and annealed Mg-RE binary alloys. Metals (Basel). 2021;**11**:1-12. DOI: 10.3390/met11040554

[114] Xie T, Shi H, Wang H, Luo Q, Li Q, Chou KC. Thermodynamic prediction of thermal diffusivity and thermal conductivity in Mg–Zn–La/Ce system. Journal of Materials Science and Technology. 2022;**97**:147-155. DOI: 10.1016/j.jmst.2021.04.044

[115] Zhu WF, Luo Q, Zhang JY, Li Q. Phase equilibria of Mg-La-Zr system and thermal conductivity of selected alloys. Journal of Alloys and Compounds. 2018;**731**:784-795. DOI: 10.1016/j.jallcom.2017.10.013

[116] Liu H, Zuo J, Nakata T, Xu C, Wang G, Shi H, et al. Effects of La addition on the microstructure, thermal conductivity and mechanical properties of Mg-3Al-0.3Mn alloys. Materials (Basel). 2022;**15**:1078. DOI: 10.3390/ma15031078

[117] Su C, Li D, Ying T, Zhou L, Li L, Zeng X. Effect of Nd content and heat treatment on the thermal conductivity of Mg-Nd alloys. Journal of Alloys and Compounds. 2016;**685**:114-121. DOI: 10.1016/j.jallcom.2016.05.261

[118] Li S, Yang X, Hou J, Du W. A review on thermal conductivity of magnesium

and its alloys. Journal of Magnesium Alloy. 2020;**8**:78-90. DOI: 10.1016/j.jma.2019.08.002

[119] Bazhenov VE, Koltygin AV, Sung MC, Park SH, Titov AY, Bautin VA, et al. Design of Mg–Zn–Si–Ca casting magnesium alloy with high thermal conductivity. Journal of Magnesium and Alloys. 2020;**8**:184-191. DOI: 10.1016/j.jma.2019.11.008

[120] Rong J, Zhu JN, Xiao W, Zhao X, Ma C. A high pressure die cast magnesium alloy with superior thermal conductivity and high strength. Intermetallics. 2021;**139**:107350. DOI: 10.1016/j.intermet.2021.107350

[121] Rong J, Xiao W, Zhao X, Ma C, Liao H, He D, et al. High thermal conductivity and high strength magnesium alloy for high pressure die casting ultrathin-walled components. International Journal of Minerals, Metallurgy, and Materials. 2022;**29**:88-96. DOI: 10.1007/s12613-021-2318-y

[122] Rong J, Xiao W, Zhao X, Fu Y, Liao H, Ma C, et al. Effects of Al addition on the microstructure, mechanical properties and thermal conductivity of high pressure die cast Mg–3RE–0.5Zn alloy ultrathin–walled component. Journal of Alloys and Compounds. 2022;**896**:162943. DOI: 10.1016/j.jallcom.2021.162943

[123] Zhao X, Li Z, Zhou W, Li D, Qin M, Zeng X. Effect of Al content on microstructure, thermal conductivity, and mechanical properties of Mg–La–Al–Mn alloys. Journal of Materials Research. 2021;**36**:3145-3154. DOI: 10.1557/s43578-021-00319-x

[124] Czerwinski F. Controlling the ignition and flammability of magnesium for aerospace applications. Corrosion Science. 2014;**86**:1-16. DOI: 10.1016/j.corsci.2014.04.047

[125] Conference I, Ostrovsky I, Henn Y. Present state and future of magnesium application in aerospace industry. In: Int. Conf. New Challenges Aeronaut. ASTEC 07. Moscow: Advanced Surface Technology Exhibition & Conference (ASTEC); 2007. pp. 1-5

[126] Gupta M, Guota N. The promise of magnesium based materials in aerospace sector. International Journal of Aeronautical and Aerospace Research. 2017;**4**:141-149. DOI: 10.19070/2470-4415-1700017

[127] Davis B. The application of magnesium alloys in aircraft interiors - changing the rules. TMS: The Minerals, Metals and Materials Society. 2015;**2015**:5

[128] Bin Huang Y, Chung IS, You BS, Park WW, Choi BH. Effect of Be addition on the oxidation behavior of Mg-Ca alloys at elevated temperature. Metals and Materials International. 2004;**10**:7-11. DOI: 10.1007/BF03027357

[129] Zeng XQ, Wang QD, Lü YZ, Ding WJ, Lu C, Zhu YP, et al. Study on ignition proof magnesium alloy with beryllium and rare earth additions. Scripta Materialia. 2000;**43**:403-409. DOI: 10.1016/S1359-6462(00)00440-1

[130] Lin P, Zhou H, Li W, Li WP, Sun N, Yang R. Interactive effect of cerium and aluminum on the ignition point and the oxidation resistance of magnesium alloy. Corrosion Science. 2008;**50**:2669-2675. DOI: 10.1016/j.corsci.2008.06.025

[131] Lin P, Zhou H, Sun N, Li WP, Wang CT, Wang M, et al. Influence of cerium addition on the resistance to oxidation of AM50 alloy prepared by rapid solidification. Corrosion Science. 2010;**52**:416-421. DOI: 10.1016/j.corsci.2009.09.029

[132] Li W, Zhou H, Zhou W, Li WP, Wang MX. Effect of cooling rate on ignition point of AZ91D-0.98 wt.% Ce magnesium alloy. Materials Letters. 2007;**61**:2772-2774. DOI: 10.1016/j.matlet.2006.10.028

[133] Hongjin Z, Yinghui Z, Yonglin K. Effect of cerium on ignition point of AZ91D magnesium alloy. China Foundry. 2008;**5**:32-35

[134] Fan JF, Yang GC, Chen SL, Xie H, Wang M, Zhou YH. Effect of rare earths (Y, Ce) additions on the ignition points of magnesium alloys. Journal of Materials Science. 2004;**39**:6375-6377. DOI: 10.1023/b:jmsc.0000043613.94027.04

[135] Marker TR. Evaluating the flammability of various magnesium alloys during laboratory- and full-scale aircraft fite tests. Public report published by the Federal Aviation Administration. 2013;**15**

[136] Wang G, Zhao Z, Zhang S, Zheng L. Effects of Al, Zn, and rare earth elements on flammability of magnesium alloys subjected to sonic burner–generated flame by Federal Aviation Administration standards. Proceedings of the Institution of Mechanical Engineers, Part G: Journal of Aerospace Engineering. 2021;**235**:1-12. DOI: 10.1177/0954410020987758

[137] Baar N. Uber die Legierungen des Molybdans mit Nickel, Mangans mit Thallium und des Calcium mit Magnesium, Thallium, Blei, Kupfer und Silber, Zeitschrift Für Anorg. Zeitschrift für anorganische und allgemeine Chemie. 1911;**70**:352-394

[138] Jiang Z, Jiang B, Zhang J, Dai J, Yang Q, Yang Q, et al. Effect of Al2Ca intermetallic compound addition on grain refinement of AZ31 magnesium alloy. Transactions of the Nonferrous Metals Society of China. 2016;**26**:1284-1293. DOI: 10.1016/S1003-6326(16)64229-2

[139] Lee DB. High temperature oxidation of AZ31+0.3wt.%Ca and AZ31+0.3wt.%CaO magnesium alloys. Corrosion Science. 2013;**70**:243-251. DOI: 10.1016/j.corsci.2013.01.036

[140] Wiese B. The Effect of CaO on Magnesium and Magnesium Calcium Alloys. Clausthal-Zellerfeld, Germany: Clausthal University of Technology; 2016. p. 134

[141] Kim SK, Lee J, Yoon Y, Jo H. Development of AZ31 Mg alloy wrought process route without protective gas. Journal of Materials Processing Technology. 2007;**188**:757-760. DOI: 10.1016/j.jmatprotec.2006.11.172

[142] Jang DI, Kim SK. Effect of Ca(OH)2 on oxidation and ignition resistances of pure Mg, Essent. Readings. Readings Magnesium Technology. 2014:145-149. DOI: 10.1002/9781118859803.ch24

[143] Sakamoto M, Akiyama S, Ogi K. Suppression of ignition and burning of molten Mg alloys by Ca bearing stable oxide film. Journal of Materials Science Letters. 1997;**16**:1048-1050. DOI: 10.1023/A:1018526708423

[144] Wu G, Fan Y, Gao H, Zhai C, Zhu YP. The effect of Ca and rare earth elements on the microstructure, mechanical properties and corrosion behavior of AZ91D. Materials Science and Engineering A. 2005;**408**:255-263. DOI: 10.1016/j.msea.2005.08.011

[145] You BS, Park WW, Chung IS. Effect of calcium additions on the oxidation behavior in magnesium alloys. Scripta Materialia. 2000;**42**:1089-1094. DOI: 10.1016/S1359-6462(00)00344-4

[146] Lee DB, Hong LS, Kim YJ. Effect of Ca and CaO on the high temperature oxidation of AZ91D Mg alloys. Materials

Transactions. 2008;**49**:1084-1088. DOI: 10.2320/matertrans.MC200799

[147] Weiler JP. Exploring the concept of castability in magnesium die-casting alloys. Journal of Magnesium Alloy. 2021;**9**:102-111. DOI: 10.1016/j.jma.2020.05.008

[148] Tang B, Li SS, Wang XS, Ben Zeng D, Wu R. An investigation on hot crack mechanism of Ca addition into AZ91D alloy. Scripta Materialia. 2005;**53**:1077-1082. DOI: 10.1016/j.scriptamat.2005.06.039

[149] Anyanwu IA, Gokan Y, Nozawa S, Suzuki A, Kamado S, Kojima Y, et al. Development of new die-castable Mg-Zn-Al-Ca-RE alloys for high temperature applications. Materials Transactions. 2003;**44**:562-570. DOI: 10.2320/matertrans.44.562

[150] Terada Y, Ishimatsu N, Mori Y, Sato T. Eutectic phase investigation in a Ca-added AM50 magnesium alloy produced by die casting. Materials Transactions. 2005;**46**:145-147. DOI: 10.2320/matertrans.46.145

[151] Easton MA, Gibson MA, Gershenzon M, Savage G, Tyagi V, Abbott TB, et al. Castability of some magnesium alloys in a novel castability die. Materials Science Forum. 2011;**690**:61-64. DOI: 10.4028/www.scientific.net/MSF.690.61

[152] Mori Y, Sugimura S, Koshi A, Liao J. Corrosion behavior of die cast Mg-Al-Mn-Ca-Si magnesium alloy. Materials Transactions. 2019;**61**:1-9

Effects of Dimensionality Reduction for High-Efficiency Mg-Based Thermoelectrics

Övgü Ceyda Yelgel

Abstract

Over the past decade, there has been significant interest in the field of thermoelectric materials (TEs) owing to their use in clean and sustainable energy sources for cooling and/or power generation applications. Especially, Mg_2XIV (XIV = Si, Ge, Sn) based TEs are promising candidates for middle-temperature range energy conversion due to their high thermoelectric performance, environmentally harmless, abundant raw materials, non-toxicity, and relatively inexpensive cost of modules. In this book chapter, we present an overview of the theoretical background of the thermoelectric transport properties (Seebeck coefficient, electrical conductivity, thermal conductivity, and thermoelectric figure of merit ZT) of magnesium-based bulk and low dimensional systems (i.e., quantum wells and quantum wires). A detailed description of the temperature-dependent Fermi level both in extrinsic and intrinsic regimes will be provided whereby it is the primary step in deriving the thermoelectric transport parameters of materials. Following the linearized Boltzmann transport equations temperature-dependent electronic transport properties (Seebeck coefficient, electrical conductivity, and electronic thermal conductivity) of materials under the energy-dependent relaxation time approximation will be defined. By employing Debye's isotropic continuum model within the single mode relaxation time approximation including various phonon relaxation rates contributed by different scattering mechanisms the lattice contribution to the thermal conductivity will be included.

Keywords: thermoelectric figure of merit, Mg-based thermoelectrics, thermoelectric transport properties, Boltzmann transport equation, thermal conductivity, phonon scattering mechanisms

1. Introduction

Due to the increasing world's demand for high-efficient clean energy researchers have been looking for environmentally friendly energy technologies. Non-renewable energy sources (nuclear power, coal, oil, and gas) have many disadvantages that can be listed as limited reserves, hazardous environmental risks, acid precipitation, and global climate change. Therefore, renewable energy sources determined as sourced either directly or indirectly from the Sun and solar energy have attracted much attention and scientific

studies have advanced rapidly in renewable energy technologies. As known heat and electricity are two different types of energy and thermoelectricity bridges between them. Thermoelectric materials can directly convert thermal energy (such as waste heat generated by automotive exhaust, domestic heating, and industrial processes) into electrical energy (and vice versa); this property makes them noteworthy for the development of sustainable energy-efficient technologies. Compared with other energy conversion technologies, thermoelectric devices have promising advantages such as having no moving parts, noiseless operation, long service life, stability, and less maintenance. Besides, it needs to be noted that the only major disadvantage of thermoelectric devices is their low efficiency for everyday common use compared to other energy conversion technologies. As summarized in **Figure 1**, thermoelectric devices can be extensively used in many fields such as power generators, cooling devices, sensors, space exploration, solar-based driven thermoelectric technologies, waste heat recovery from automobile engines, and energy harvesting and temperature control [1–6].

Different sectors contributing to huge amounts of waste heat energy (∼66%), the biggest energy problem in the world right now, could be transformed to electrical energy via thermoelectric materials with the help of their ability to convert large amounts of wasted thermal energy into useful energy. **Figure 2a** shows the utilization of waste heat energy from different types of waste energy sources by thermoelectric generator.
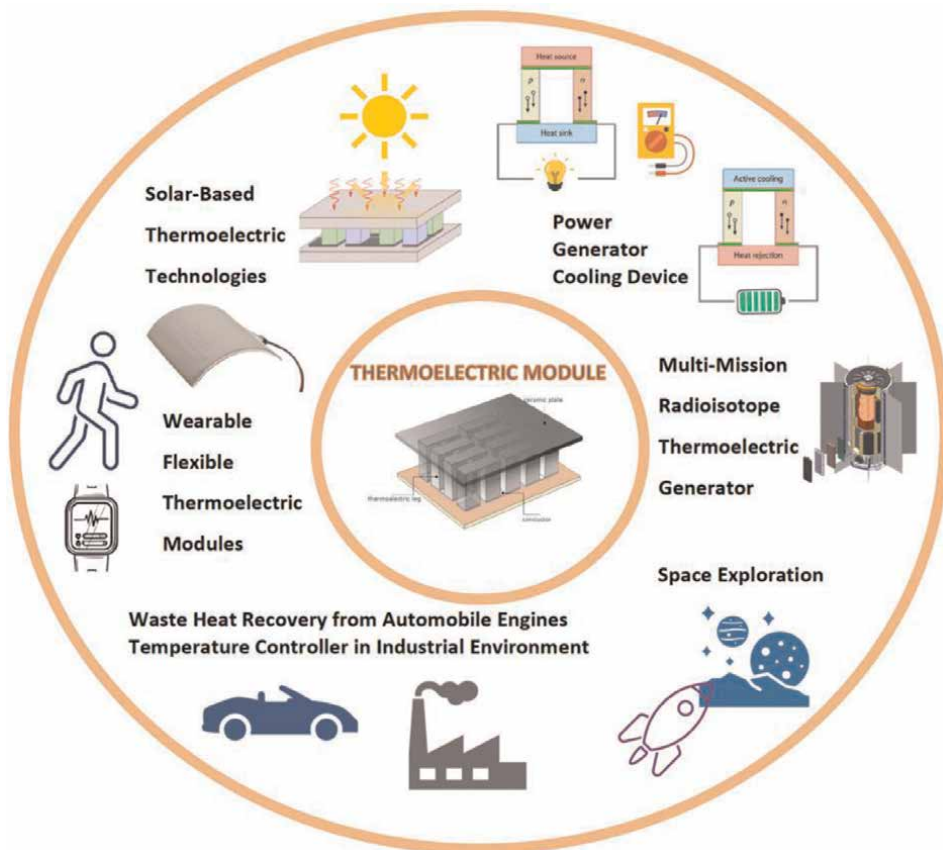
Figure 1.
Overview of application fields of thermoelectric materials.

Thermoelectric generators are built of thermoelectric modules and a single module consists of a thermocouple. In **Figure 2b**, an operation of thermoelectric module working as a power generator mode is given. A single thermocouple generates a small thermoelectric force, and therefore to the formation of one module is used even so many thermocouples in this manner when the thermal energy is supplied the heat is directed to the thermoelectric modules in which a conversion of thermal energy into electricity. As shown in **Figure 3a**, a thermoelectric couple composed of an n-type (electrons are carriers) and a p-type (holes are carriers) semiconductor material connected through metallic electrical contact pads. Both power generation (Seebeck effect) and refrigeration (Peltier effect) can be accomplished using the same module.

The thermoelectric performance of the materials at a certain temperature is ranked by the dimensionless figure of merit ZT. Its definition is $ZT = \frac{S^2 \sigma}{\kappa_{total}} T$ where T is the absolute temperature, S is the Seebeck coefficient, σ is the electrical conductivity, and κ_{total} is the total thermal conductivity ($\kappa_{total} = \kappa_c + \kappa_{bp} + \kappa_{ph}$) which has contributions from carriers (i.e., from electrons for n-type materials or holes for p-type materials, κ_c), electron-hole pairs (bipolar, κ_{bp}), and phonons (κ_{ph}), respectively. The material with a high ZT value has better thermoelectric energy conversion efficiency.
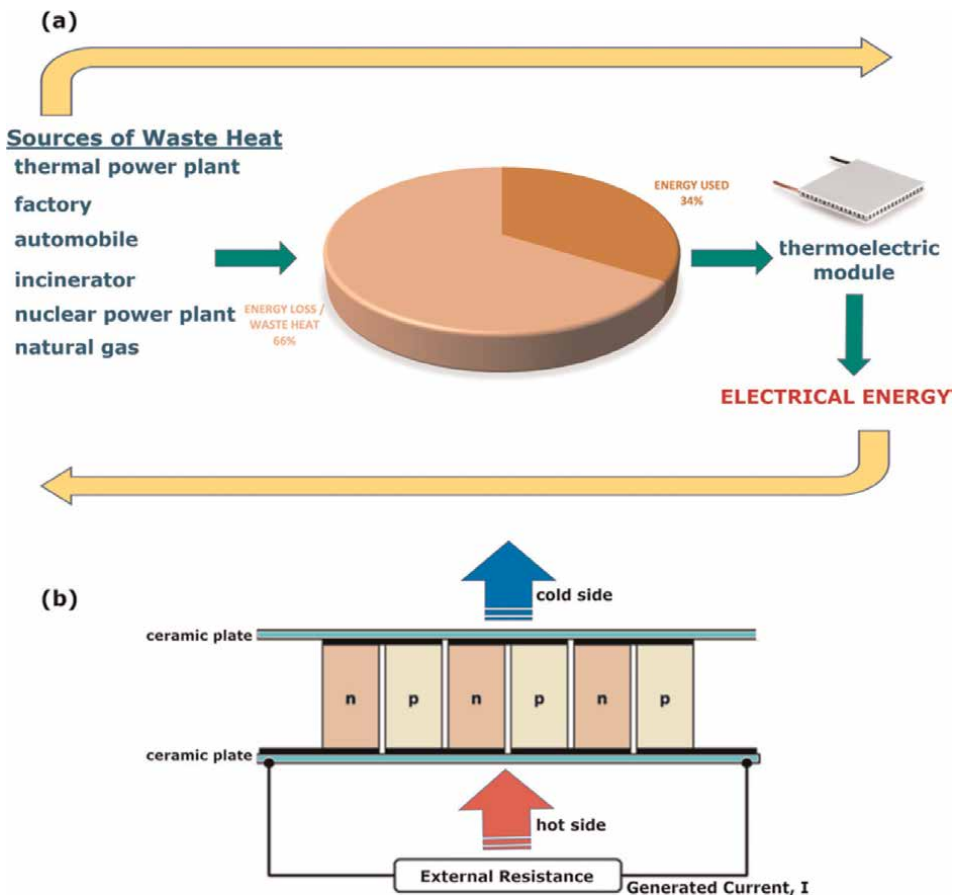
Figure 2.
(a) Utilization of waste heat energy from different types of waste energy sources by thermoelectric generator, and (b) scheme and operation of thermoelectric module working as a power generator.
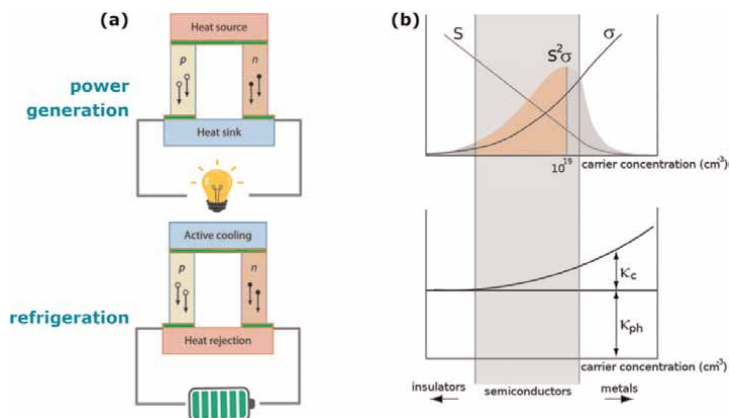
Figure 3.
(a) Operation principle of a power generator (Seebeck effect) and a refrigerator (Peltier effect), and (b) schematic presentation of carrier concentration dependence of electrical transport properties (Seebeck coefficient, electrical conductivity, carrier thermal conductivity) and thermal transport sourced from phonons.

Therefore, efficient thermoelectric materials need to have a large Seebeck coefficient to maximize the conversion of heat to electrical power; high electrical conductivity to minimize Joule heating; and low total thermal conductivity to retain heat at the junctions and maintain a large temperature gradient. However, as presented in **Figure 3b,** these thermoelectric transport properties are strongly coupled with each other and dependent on the material's band and crystal structure parameters. Owing to the complex interdependence among these properties, it is quite challenging to optimize *ZT* value and for this reason, the vast majority of research in this field has been focused on this issue. A desirable goal for everyday practical usage of the thermoelectric device is expected to have their efficiency in the range of *ZT* > 1.5 and *ZT* > 2 for power generation and thermoelectric cooling, respectively [7–9]. In the literature, until the 1990s, the highest value of *ZT* was found to be around 1 which means only 10% conversion efficiency [10–12]. In the last few years, on the other hand, the highest *ZT* values have been recorded with the help of using novel materials, following different processing techniques, and having new mechanisms [2, 13–16]. There are various strategies to improve thermoelectric efficiency; maximizing thermoelectric power factor ($PF = S^2\sigma$) by following different methods such as convergence of electronic band valleys, carrier energy filtering, and generating resonant levels in electronic bands [13, 15, 17–22]; reducing total thermal conductivity with introducing new point defects by making alloys, embedding nano inclusion, anharmonicity, nano/mesoscale grain boundaries [2, 14, 23–28]. Among all these methods we must admit that in the thermoelectric literature Hicks and Dresselhaus made a revolutionary invention by proposing the use of low-dimensionalizing in thermoelectric devices and opened a new pathway in high-efficiency thermoelectric technologies in the early 1990s [29]. In the low dimensionalization method, reduced sizes of materials to the order of a nanometer in one or two directions are used (such as superlattices, nanowires, or quantum dots). Following this strategy allows enhancing *ZT* to a very large extent by optimizing electronic and thermal properties of materials in ways that are not possible in bulk materials. Also, the thermoelectric efficiency of traditional three-dimensional bulk materials can be improved with the help of the low-dimensionalization method. Low dimensional thermoelectric materials with unusual high *ZT* values (which can easily break the limits of unity) have
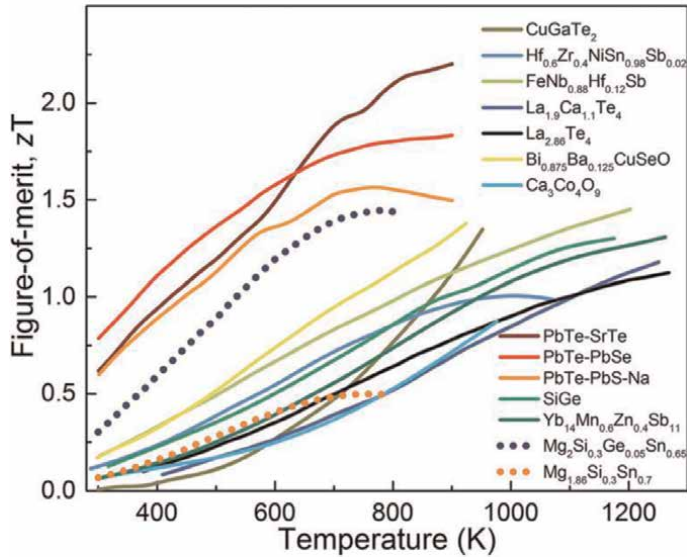
Figure 4.
High-efficient hermoelectric materials working in the middle-to-high temperature range. Reproduced from Ref. [40] with permission from the Royal Society of Chemistry.

been reported by several groups [2, 13, 15, 17, 30–33]. Moreover, there have been significant improvements in portable electronics and intelligent society based on the internet of things (IoTs), and the internet of nano things (IoNTs) however rechargeable lithium-ion batteries are inconvenient for applications. At this point, by generating electricity from the temperature difference between the human body and the environment, high-efficiency nano-based thermoelectric materials can be an ideal solution to replace lithium-ion batteries in IoTs and IoNTs [34–39].

There are so many different thermoelectric materials however among all of them the materials working in the middle-temperature range (namely from 400 K to 800 K) are widely used for thermoelectric applications. Generally, in commercial practice Bi_2Te_3-, $PbTe$-, $CoSb_3$-, and $GeTe$-based thermoelectric compounds are mainly used whereas they have toxic constituent elements and are scarce [40–43]. The present market search for cheap, environmentally friendly, and non-toxic thermoelectric materials due to safety regulations. Compared to other middle-temperature thermoelectric materials Magnesium-based materials (Mg_2X; X = Si, Ge, Sn) have been regarded as promising candidates for high efficiency and large-scale application owing to their high availability, low-cost, reasonable high efficiency, non-toxicity, and low mass density. In **Figure 4**, the highest *ZT* values of the state-of-the-art medium-to-high temperature thermoelectric materials are given to compare with Mg-based thermoelectric materials.

Mg_2X materials are intermetallic alloys that have been investigated for decades as high-efficiency thermoelectric candidates [44, 45]. Mg_2X compounds crystallize in the cubic anti-fluorite structure (space group of $Fm\bar{3}m$ #225) phase with X in face-centered cubic position and Mg in tetrahedral sites with three atoms per primitive unit cell in that one X atom is located at $a(0\ 0\ 0)$ and 2 Mg atoms are located at $a(0.25, 0.25, 0.25)$ and $a(0.75, 0.75, 0.75)$. The crystal structure model of Mg_2X and schematic illustration of the band structures of Mg_2X around $\mathbf{\Gamma}$ and $\mathbf{X}$ points are shown in **Figure 5a** and **b**, respectively.
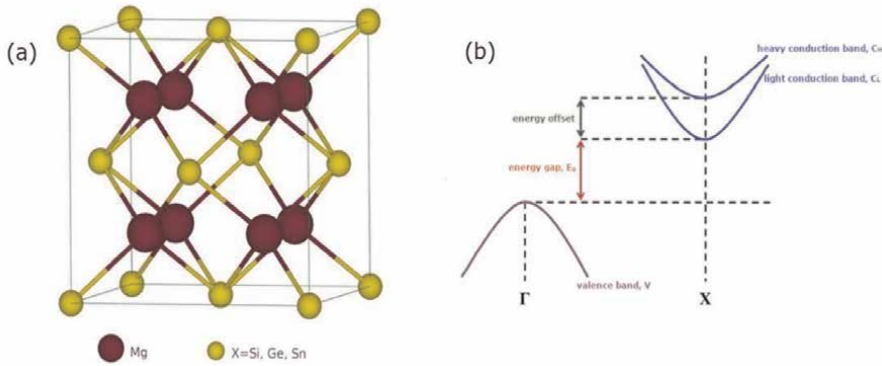
Figure 5.
(a) Crystal structure model of Mg_2X (X = Si, Ge, Sn), and (b) schematic illustration of Mg_2X around Γ and X points.

Properties/Parameters	Mg$_2$Si	Mg$_2$Ge	Mg$_2$Sn
a (Å)	6.338	6.385	6.765
E$_g$ (eV) at 0 K	0.77	0.74	0.35
ΔE (eV) at 0 K	0.4	0.58	0.16
Melting point (K)	1375	1388	1051
γ	1.32	1.38	1.27
κ_{ph} (W m K^{-1})	7.9	6.6	5.9

Table 1.
List of electronic (lattice parameters, band gaps, and energy offsets), physical (melting points), and phononic properties (Grüneissen parameter, and phonon thermal conductivity) of Mg_2X (X = Si, Ge, Sn) binary alloys [46–48].

In addition to that, in **Table 1**, electronic and physical properties are listed for Mg$_2$X-based binary alloys.

The overview of the highest reported *ZT* values for Mg-based thermoelectric materials (in the form of binary, ternary, and quaternary n- and p-type doped) is illustrated in **Figure 6**.
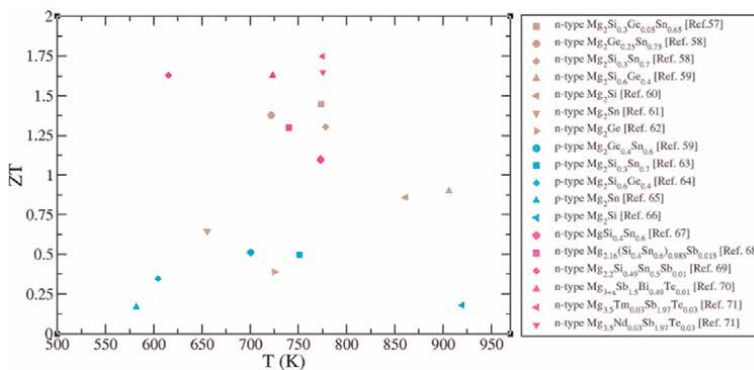
Figure 6.
State-of-the-art ZT values for Mg-based thermoelectric materials from different works in the literature [49–63].

As stated above combining the advantages of using low-dimensionalization and Mg-based thermoelectric materials can lead to highly efficient thermoelectric applications. Despite this, in the literature, there have been very limited theoretical investigations of low-dimensional effects on thermoelectric transport properties of Mg-based materials in detail. Therefore, in this book chapter, unlike the related literature, a comprehensive explanation of the temperature-varied Fermi levels (both at extrinsic and intrinsic regimes) will first be presented for bulk and low-dimensional Mg-based materials. Then, by following the linearized Boltzmann transport equations temperature dependence of electronic transport properties (Seebeck coefficient, electrical conductivity, and carrier thermal conductivity) of bulk and low-dimensional Mg-based materials under the energy-dependent relaxation time approximation will be defined. Also, by employing Debye's isotropic continuum model within the single mode relaxation time approximation including various phonon relaxation rates contributed by different scattering mechanisms the lattice thermal contribution will be explained meticulously. By presenting a detailed theoretical background of the dimensionality effect on thermoelectric efficiency and highlighting the temperature dependencies of transport properties of low-dimensional systems we shed light on the challenges and perspectives for promoting the development of future Mg-based thermoelectric applications.

2. Thermoelectric transport properties of bulk and low-dimensional systems

The theory of transport properties in thermoelectric materials deals with the temperature dependence of electrical and thermal transport properties. Here, we introduce the theoretical background of thermoelectric transport properties in bulk and low-dimensional systems, respectively.

As stated in the above section, the dimensionless figure of merit includes three interdependent transport properties of S, σ, and κ_{total} and which impedes the maximization of ZT in bulk systems. To avoid this problem, in 1993, Hicks and Dresselhaus examined the effects of using low-dimensional structures on the ZT with the assumption of parabolic bands and constant relaxation time in a one-band material [29]. To summarize Hicks and Dresselhaus' approach and describe the effects of dimensionalization as a bird's eye view, by defining a dimensional factor N (N = 1, 2, and 3 for 1 dimensional (1D), 2 dimensional (2D), and 3 dimensional (3D) systems, respectively) the dimensionality dependence of ZT can be written for the case of conduction along the x direction as [29, 64],

$$Z_N T = \frac{\frac{N}{2}\left(S_N \frac{F_{N/2}}{F_{N/2-1}}\zeta^*\right)^2 F_{N/2-1}}{\frac{1}{B_N} + \left(\frac{N+4}{2}\right)F_{N/2+1} - \beta_N \frac{F_{N/2}^2}{F_{N/2-1}}} \tag{1}$$

where ζ^* is the reduced chemical potential, $S_N = \frac{14-6N+N^2}{3}$, $\beta_N = \frac{34-9N+2N^2}{6}$, and the Fermi-Dirac function F_i is given by $F_i(\zeta^*) = \int_0^\infty \frac{x^i dx}{\exp(x-\zeta^*)+1}$. The material property dependent parameter B_N is expressed as,

$$B_N = \gamma_N \left(\frac{2k_B T}{\hbar^2}\right)^{N/2} \frac{k_B^2 T \mu_x}{e \kappa_{\text{ph}}} \tag{2}$$

where k_B is the Boltzmann constant and $\hbar$ is the reduced Planck's constant, $\gamma_{1=\frac{2}{\pi a^2}}(m_x)^{1/2}$ for 1D systems, $\gamma_{2=\frac{1}{2\pi a}}(m_x m_y)^{1/2}$ for 2D systems, and $\gamma_{3=\frac{1}{3\pi^2}}(m_x m_y m_z)^{1/2}$ for 3D systems, respectively. Here m_x, m_y, and m_z are the effective mass components for the x, y, and z directions, μ_x is the mobility in the x direction, and a is the width of a 2D quantum well or 1D nanowire. From these equations, we can conclude that ZT depends on ζ^* and B_N parameters. For bulk materials, ZT can be improved by optimizing ζ^* with suitable doping and B_N with reducing κ_{ph} and/or increasing μ_x. From the above equations, it is seen that in low-dimensional systems, ZT can be enhanced by adjusting the width/thickness of wells and wires, respectively. Decreasing the width/thickness of the quantum well or nanowire gives rise to boundary scattering mechanisms which lead to a dramatic reduction in phonon thermal conductivity. In **Figure 7**, the quantum well thickness and quantum wire diameter dependences of ZT are represented for quantum wells and wires of Bi_2Te_3 fabricated along the x, y, and z directions [64].

After emphasizing the importance of using low-dimensional materials briefly, we can now move on to examine the detailed transport properties of thermoelectric materials both in bulk and low-dimensional structures to understand the detailed physical background behind these temperature-dependent transport properties and carrier scattering mechanisms. Based on the semiclassical model we follow the Boltzmann transport equation approach to investigate the thermoelectric transport phenomena quantitatively and explain how the temperature variations of carriers and phonons. All the electronic transport properties of thermoelectric materials are dependent on temperature-varied Fermi levels (E_F) in extrinsic and intrinsic regimes. Therefore, simpler schemes leading to expressions for the Fermi level in bulk semiconductors have been given in the book by McKelvey [65],

$$E_F^{\mathrm{ext}}(\mathrm{n-type}) = \frac{1}{2}(E_c + E_d) + \frac{k_B T}{2}\ln\frac{N_d}{2U_c} - k_B T \sinh^{-1}\left[\sqrt{\frac{U_c}{8N_d}}\, exp\left(-\frac{\Delta E_i}{2k_B T}\right)\right]$$

(3)

$$E_F^{\mathrm{ext}}(\mathrm{p-type}) = \frac{1}{2}(E_a + E_v) + \frac{k_B T}{2}\ln\frac{N_a}{2U_v} - k_B T \sinh^{-1}\left[\sqrt{\frac{U_v}{8N_d}}\,\exp\left(-\frac{\Delta E_i}{2k_B T}\right)\right]$$

(4)
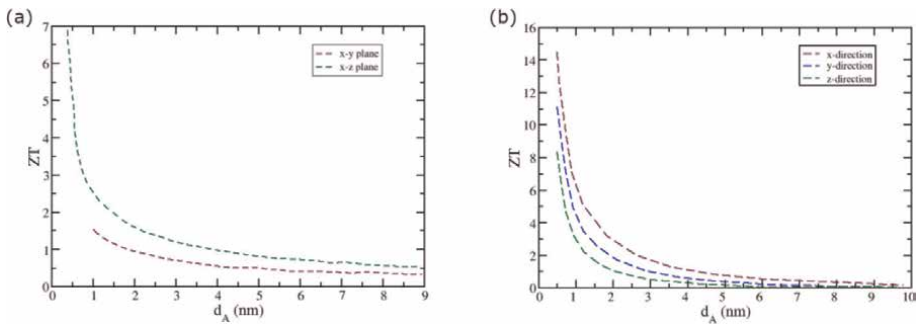
Figure 7.
Enhanced ZT values as a function of (a) the quantum well thickness, and (b) the quantum wire diameter. Here quantum wells are fabricated in the x-y plane and the x-z plane while quantum wires are fabricated along the x, y, and z directions (data are read from Ref. [64]).

where E_c is the conduction band edge, E_v is the valence band edge, E_d is the donor energy level, and E_a is the acceptor energy level, ΔE_i is given as $(E_c - E_d)$ for the donor ionization and expressed as $(E_a - E_v)$ for the acceptor ionization energies. Also, N_d and N_a are the concentrations of donor impurity and acceptor impurity atoms, respectively. U_c and U_v parameters are given as $U_c = 2\left((m_n^* k_B T)/(2\pi\hbar^2)\right)^{3/2}$ and $U_v = 2\left(\left(m_p^* k_B T\right)/\left(2\pi\hbar^2\right)\right)^{3/2}$ where m_n^* is for the electron mass and m_p^* is for the hole mass. At high enough temperatures donors at the E_d or acceptors at the E_a levels become ionized and the material turns out to be an intrinsic semiconductor. The temperature dependence of EF for both types of doped semiconductors is expressed as [65],

$$E_F^{\text{int}}\left(\text{n} - \text{and p} - \text{types}\right) = \frac{1}{2}\left(E_v + E_c\right) + \frac{3}{4}k_B T \ln\left(\frac{m_p^*}{m_n^*}\right). \qquad (5)$$

The temperature dependence of the Fermi level for semiconductors can be summarized as; in n-type doped semiconductors, the E_F is in the middle of the E_d and E_c at 0 K, and when the temperature rises the E_F first rises slowly and then decreases through the E_d and reaches the center of the gap; similarly, in p-type doped semiconductors the E_F is in the middle of the E_a and E_v at 0 K and when the temperature rises the E_F first goes down slightly and then increases through the E_a. For both types of doped semiconductors when the donor/acceptor levels are almost completely ionized the E_F approaches to E_F^{int}. Moreover, the energy dispersion function at the Brillouin zone center is determined as

$$E\left(k_x, k_y, k_z\right) = \frac{\hbar^2 k_x^2}{2m_x^*} + \frac{\hbar^2 k_y^2}{2m_y^*} + \frac{\hbar^2 k_z^2}{2m_z^*} \qquad (6)$$

where k_x, k_y, and k_z are the propagation vector component along the x, y, and z axes, respectively. The effective mass tensor components of the constant energy surfaces are denoted as m_x^*, m_y^*, and m_z^*.

In this book chapter, we consider low-dimensional systems as 2D quantum wells and 1D quantum wires and present the theoretical modeling of the temperature dependence of thermoelectric transport properties in these systems. First, in 2D quantum well systems, we assume that the system has B/A/B layers of material A (as a well material with nA atomic layers of thickness a each and total thickness d_A) and material B (as a barrier with nB atomic layers of thickness b each and total thickness d_B) also band gap differences materials A and B to confine the current carriers to the well material and system is grown in the z-direction. The electronic dispersion in the z-direction is given as,

$$E\left(k_x, k_y\right) = \frac{\hbar^2 k_x^2}{2m_x^*} + \frac{\hbar^2 k_y^2}{2m_y^*} + E_j, \qquad (7)$$

where the quantum confinement term E_j in the jth quantum sublevel is expressed as

$$E_j = \frac{\hbar^2 \pi^2}{2m_z^* d_A^2} j. \qquad (8)$$

Assuming the carrier concentration does not change whereas the well thickness varies and up to jth quantum sub-level is occupied by carriers the temperature variation of E_F for 2D quantum wells can be defined as

$$E_f^{\text{ext/int}}\left(2\text{D}_{\text{QWL}}\right) = E_f^{\text{ext/int}}(3\text{D}_{\text{BULK}}) - E_j. \tag{9}$$

in both extrinsic and intrinsic regimes [66]. Moreover, the energy band gap of this 2D system is given as

$$E_g\left(2\text{D}_{\text{QWL}}\right) = E_g(3\text{D}_{\text{BULK}}) + \frac{\hbar^2\pi^2}{2d_A^2}\left(\frac{1}{m_{z,e}^*} + \frac{1}{m_{z,h}^*}\right) \tag{10}$$

where $E_g(3\text{D}_{\text{BULK}}) = E_c - E_v$ and $m_{z,e}^*$ and $m_{z,h}^*$ are electrons and holes effective masses in the growth direction, respectively.

In 1D quantum wire systems, we assume that carrier confinement in the y and z directions and free-electron-like motion in the x direction also a is the width of the wire considered to have a square cross-section. The electronic dispersion relation for the 1D system is given as,

$$E(k_x) = \frac{\hbar^2 k_x^2}{2m_x^*} + E_{i,j}, \tag{11}$$

where the quantum confinement terms $E_{i,j}$ in the ith and jth quantum sublevel are expressed as

$$E_{i,j} = \frac{\hbar^2\pi^2}{2m_y^* d_A^2}i + \frac{\hbar^2\pi^2}{2m_z^* d_A^2}j, \tag{12}$$

with the width of the wire d_A assumed to have a square cross-section. Similar to 2D quantum wells, for 1D quantum wire systems the temperature dependence of E_F can be written as

$$E_f^{\text{ext/int}}\left(1\text{D}_{\text{QWR}}\right) = E_f^{\text{ext/int}}(3\text{D}_{\text{BULK}}) - E_{i,j} \tag{13}$$

both in extrinsic and intrinsic regimes. Additionally, the band gap of 1D systems is given as

$$E_g\left(1\text{D}_{\text{QWR}}\right) = E_g(3\text{D}_{\text{BULK}}) + \frac{\hbar^2\pi^2}{2d_A^2}\left(\frac{1}{m_{y,e}^*} + \frac{1}{m_{y,h}^*}\right) + \frac{\hbar^2\pi^2}{2d_A^2}\left(\frac{1}{m_{z,e}^*} + \frac{1}{m_{z,h}^*}\right). \tag{14}$$

As shown in **Figure 8**, the carrier energy dependence of the density of states (DOS) per unit volume for a single bad with the subband in bulk, quantum well, and quantum wire systems by assuming transport is along the direction of the x-axis. Compared to the 3D system $g(E)$ enhances at E_0 owing to the rise of carriers both with confinement effect in 2D and 1D systems.

The theoretical expressions of electronic transport properties for thermoelectric materials (namely the Seebeck coefficient, electrical conductivity, and electronic thermal conductivity) are explained by following the Boltzmann transport equation.
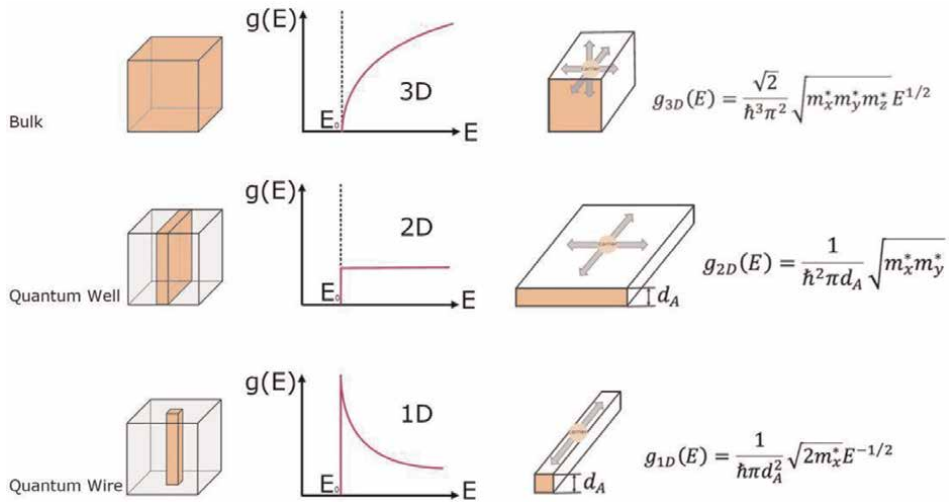
Figure 8.
The electronic density of states for 3D, 2D, and 1D systems in relation to carrier energy (E_0 corresponds to the energy at the bottom of the conduction band).

Presenting the theoretical background of each transport coefficient can help to understand the physical origin of these properties in relation to temperature and carrier concentration for bulk, quantum well, and quantum wire systems.

Assuming an isotropic solid within the nearly free electron/hole model under the consideration of an electric field and a temperature gradient is applied the thermo-electric transport properties can be determined by solving the linearized Boltzmann equation. Here, considering both heat and electricity currents flow in the x-direction, the electric current density i_x and the rate of flow of heat per unit cross-sectional area (carried by carriers) w_x are given [65–70].

$$i_x = \mp \int_0^\infty e v_x f(E) g(E) dE \qquad (15)$$

$$w_x = \int_0^\infty v_x (E - E_f) f(E) g(E) dE \qquad (16)$$

where $-e$ is the electronic charge, v_x is the velocity of charge carriers in the x direction for an isotropic conductor, $f(E)$ is the Fermi distribution function, $g(E)$ is the density of state function, and $E - E_f$ represents the total energy transported by a carrier. At equilibrium, carrier distribution follows the Fermi Dirac statistics through $f_0(E) = \left[\exp\left(\frac{E - E_f}{k_B T}\right) + 1 \right]^{-1}$ where E_f is the Fermi energy. The above equations can be re-written by replacing f with $f - f_0$ (since there is no transport $i_x = w_x = 0$ when $f = f_0$) as

$$i_x = \mp \int_0^\infty e v_x^2 \tau g(E) \frac{\partial f_0}{\partial E} \left(\frac{\partial E_f}{\partial x} + \frac{E - E_f}{T} \frac{\partial T}{\partial x} \right) dE \qquad (17)$$

$$w_X = \pm \frac{E_f}{e} i_x + \int_0^\infty E v_x^2 g(E) \tau \frac{\partial f_0}{\partial E} \left[\frac{\partial E_f}{\partial x} + \frac{E - E_f}{T} \frac{\partial T}{\partial x} \right] dE. \qquad (18)$$

Here, the assumptions are $\tau_x = \frac{\mu_x m_x^*}{e}$ with μ_x is the carrier mobility in the x-direction and $v_x^2 = \frac{2E}{3m_x^*}$. By taking the condition $i_x = 0$ as the Seebeck coefficient is written

$$S = -\frac{\Delta V}{\Delta T} = \frac{\varepsilon_x}{\nabla T} = \frac{1}{e}\frac{\partial E_f/\partial x}{\partial T/\partial x} \tag{19}$$

where the electric field $\mathcal{E}_x$ is given as $\varepsilon_x = \pm\frac{1}{e}\frac{\partial E_f}{\partial x}$ and S is expressed as

$$S = \pm\frac{1}{e}\left[\int_0^\infty v_x^2 \tau_x g(E)\frac{\partial f_0}{\partial E}\frac{E - E_f}{T}dE \Big/ \int_0^\infty v_x^2 \tau_x g(E)\frac{\partial f_0}{\partial E}dE\right] \tag{20}$$

here + sign and − sign represent p- and n-type semiconductors, respectively. The electrical conductivity expression in the extrinsic regime can be defined by setting the temperature gradient as $\partial T/\partial x = 0$ and expressed as

$$\sigma_{\text{ext}} = \frac{i_x}{\varepsilon_x} = -\int_0^\infty e^2 v_x^2 \tau_x g(E)\frac{\partial f_0}{\partial E}dE. \tag{21}$$

Additionally, in the intrinsic regime, the electrical conductivity of semiconductors is given by

$$\sigma_{\text{int}} = eN_i\left(\mu_n + \mu_p\right) = Ae^{-E_g/2k_B T} \tag{22}$$

where N_i is the equilibrium carrier density, A is a temperature-independent adjustable parameter, μ_n and μ_p is the electron and hole mobility, respectively. Lastly, the total thermal conductivity is the sum of three contributions from carriers (electrons or holes), bipolar (electron-hole pairs), and phonons. The electronic thermal conductivity is related to the electrical conductivity by the Wiedemann-Franz law as $\kappa_c = L\sigma T$ where L is the Lorenz number namely a relatively complex transport parameter. The carrier thermal conductivity comes from monopolar carriers (electrons or holes), is determined under the condition of $i_x = 0$, and is given as [71].

$$\kappa_c = -\frac{w_x}{\partial T/\partial x} = -\int_0^\infty v_x^2 E_g(E)\tau_x \frac{\partial f_0}{\partial E}\left(\frac{\partial E_f/\partial x}{\partial T/\partial x} + \frac{E - E_f}{T}\right)dE. \tag{23}$$

By determining these integrals we can now write expressions for the temperature dependence of electronic transport properties of 3D, 2D, and 1D systems. As the dimension of a system changes the above integrals need to be varied by the electronic density of states. In **Table 2**, the expressions for temperature-varied electronic transport properties are listed for bulk, quantum well, and wire systems.

In **Figure 9a–d**, the electronic transport properties of bulk and quantum wire structures (with wire widths taken as $d_A = 6, 7$, and 8 nm) of $\text{Mg}_{3.2-y}\text{Co}_y(\text{Sb}_{0.3}\text{Bi}_{0.7})_{1.99}\text{Te}_{0.01}$ (y = 0.05) are presented in the temperature ranges between 300 and 850 K. Additionally the experimental measurements of the temperature dependence of See beck coefficient and electrical conductivity results for bulk system reported by Ref. [72] are included to compare our theoretical results with experiments. As seen from the Fermi level results in **Figure 9a**, both bulk and quantum wire systems show extrinsic and intrinsic regimes in the whole temperature

Electronic transport property	3D bulk system	2D quantum well system	1D quantum wire system
S (V/K)	$\pm\dfrac{k_B}{e}\left[\dfrac{5F_{3/2}}{3F_{1/2}} - \dfrac{E_f}{k_BT}\right]$	$\pm\dfrac{k_B}{e}\left[\dfrac{2F_1}{F_0} - \dfrac{E_f}{k_BT}\right]$	$\pm\dfrac{k_B}{e}\left[\dfrac{3F_{1/2}}{F_{-1/2}} - \dfrac{E_f}{k_BT}\right]$
σ_{ext} (Ω.m)	$\dfrac{1}{2\pi^2}\left(\dfrac{2k_BT}{\hbar^2}\right)^{3/2}\left(m_x^*m_y^*m_z^*\right)^{1/2}e\mu_xF_{1/2}$	$\dfrac{k_BT}{\hbar^2\pi d_A}\sqrt{m_x^*m_y^*}\,e\mu_xF_0$	$\dfrac{\sqrt{2k_BT}}{\hbar^2\pi d_A^2}\sqrt{m_x^*}\,e\mu_xF_{-1/2}$
σ_{int} (Ω.m)	$Ae^{-E_g^{3D}/2k_BT}$	$Ae^{-E_g^{2D}/2k_BT}$	$Ae^{-E_g^{1D}/2k_BT}$
κ_c (W/K.m)	$\dfrac{\tau_x\hbar^2}{6\pi^2}\left(\dfrac{2k_BT}{\hbar^2}\right)^{5/2}\dfrac{\left(m_y^*m_z^*\right)^{1/2}}{\left(m_x^*\right)}k_B\left[\dfrac{7}{2}F_{5/2} - \dfrac{25F_{3/2}^2}{6F_{1/2}}\right]$	$\dfrac{\tau_x k_B\left(2k_BT\right)^2}{4\pi\hbar^2 d_A}\dfrac{\sqrt{m_y^*}}{\sqrt{m_x^*}}\left[3F_2 - \dfrac{4F_1^2}{F_0}\right]$	$\dfrac{\tau_x k_B\left(2k_BT\right)^{3/2}}{\pi^2\hbar d_A^2}\sqrt{m_x^*}\left[\dfrac{5F_{3/2}}{2} - \dfrac{9F_{1/2}^2}{2F_{-1/2}}\right]$

Table 2.
Temperature variation of electronic transport properties (Seebeck coefficient S, electrical conductivity in extrinsic σ_{ext} and intrinsic σ_{int} regimes, and carrier thermal conductivity κ_c) of 3D, 2D, and 1D systems as a function of Fermi integrals described as $F_i = \int_0^\infty \dfrac{x^i dx}{\left(e^{x-\zeta^*}+1\right)}$ where energy (x) and the reduced Fermi energy (ζ^*) of carriers normalized to the thermal energy are $x = E/k_BT$ and $\zeta^* = E_f/k_BT$, respectively.
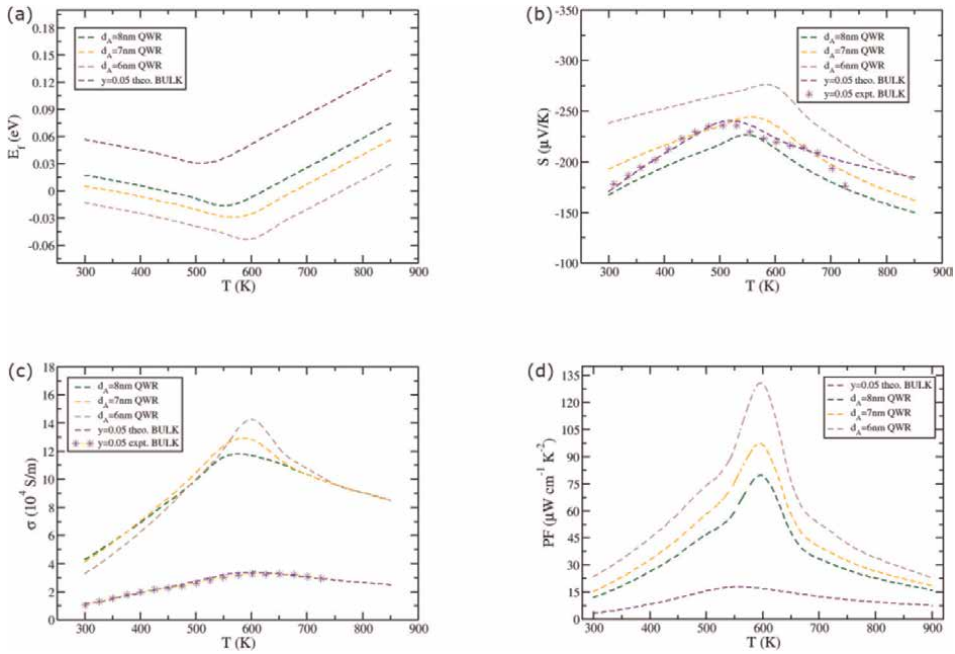
Figure 9.
The electronic transport properties of bulk $Mg_{3.2-y}Co_y(Sb_{0.3}Bi_{0.7})_{1.99}Te_{0.01}$ *(y = 0.05) and its quantum wire structure with the wire widths of d_A = 6 nm, 7 nm, and 8 nm. The temperature variation of (a) Fermi level, (b) Seebeck coefficient, (c) electrical conductivity, and (d) power factor. Dashed lines are theoretical calculations and the star symbol is the experimental measurements read from ref. [72].*

range. While the critical extrinsic-to-intrinsic turnover temperature is around 500 K for bulk sample, the temperature shifts to around 600 K for nanowire systems. In **Figure 9b**, the temperature variations of Seebeck coefficients are illustrated for both 3D and 1D systems. From these results, it is clearly seen that by decreasing the quantum wire width the maximum value of $|S|$ can be improved from 241.1 $(\mu V/K)$ at 510 K upto 276.2 $(\mu V/K)$ at 593 K by using $d_A = 6$ nm quantum wire instead of bulk structure. The temperature dependence of electrical conductivity for all systems is seen in **Figure 9c**. From theoretical calculations, it is seen that a dramatic enhancement can be gained in electrical conductivity by choosing low-dimensional systems. The maximum value of σ at 600 K is found to be 3.4×10^4 S/m for bulk sample whereas it is found as 14.2×10^4 S/m for $d_A = 6$ nm quantum wire sample. Lastly, the temperature variation of the thermoelectric power factor for all samples is shown in **Figure 9d** and the highest PF values are 18.5 $\mu Wcm^{-1}K^{-2}$ at 550 K for the bulk sample and 130.1 $\mu Wcm^{-1}K^{-2}$ at 590 K for $d_A = 6$ nm quantum wire sample.

In **Figure 10a** and **b**, the temperature dependence of electronic thermal conductivity of bulk and quantum wire structures (with different quantum wire widths taken as $d_A = 6, 7$, and 8 nm) of $Mg_{3.2-y}Co_y(Sb_{0.3}Bi_{0.7})_{1.99}Te_{0.01}$ (y = 0.05) samples are represented in the temperature range of 300–850 K. From our theoretical calculations at room temperature it is found that while the minimum value of κ_c is 0.051 $Wm^{-1}K^{-1}$ for bulk sample, a dramatic decrease is gained for quantum wire samples with the minimum value of κ_c is 2.1×10^{-5} $Wm^{-1}K^{-1}$ for $d_A = 6$ nm sample. As seen from these temperature-varied electronic properties calculations, choosing low dimensional structured thermoelectric materials rather than bulk leads to enhanced
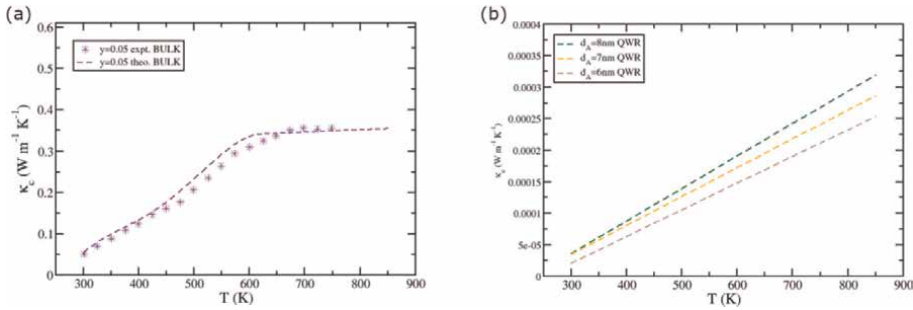
Figure 10.
Temperature variation of the electronic thermal conductivity of (a) bulk $Mg_{3.2-y}Co_y(Sb_{0.3}Bi_{0.7})_{1.99}Te_{0.01}$
(y = 0.05) and (b) its quantum wire structure with the wire widths of d_A = 6, 7, and 8 nm. Dashed lines are
theoretical calculations and the star symbol is the experimental measurements done by Ref. [72].

thermoelectric power factor values which will help to get a more efficient thermo-
electric material with a higher thermoelectric figure of merit.

The bipolar diffusion process is determined as at sufficiently high temperatures
electron-hole pairs occur by excitation across the forbidden gap hence a continuous
stream of charges flows in the direction of temperature gradient. High-efficiency
thermoelectric materials are heavily doped narrow-band gap semiconductors and κ_{bp}
plays a crucial role above room temperature in these small-band-gap thermoelectrics.
In the assumption of an idealized semiconductor, has parabolic valence and conduc-
tion bands in that carriers only undergo acoustic mode lattice scattering, the κ_{bp} is
defined by Glassbrenner and Slack

$$\kappa_{bp} = \frac{b}{(1+b)^2}\left[\frac{E_g}{k_B T}+4\right]^2\left[\frac{k_B}{e}\right]^2\sigma_{int}T \qquad (24)$$

here the ratio of electron to hole mobility is determined with the parameter b. This
expression is simplified by Yelgel and Srivastava [65].

$$\kappa_{bp} = F_{bp}T^p\exp\left(-E_g/2k_B T\right) \qquad (25)$$

where F_{bp} and p are adjustable parameters vary with doping level and dopant type.
When a material's dimension is changed to low dimensional structures in the expres-
sion of κ_{bp} the band gap property should be updated.

The most dominant contribution on the total thermal conductivity is sourced from
lattice vibrations namely the phonon thermal conductivity κ_{ph} in degenerately doped
and small-band-gap semiconductors. In thermal equilibrium condition, the average
number of phonons in the qth mode and at temperature T is defined by the Bose-
Einstein distribution function given as $\overline{n}_q = \frac{1}{\exp(\hbar\omega(q)/k_B T)-1}$ where $\omega(q)$ is the angular
frequency of phonons, q is phonons wae vector, and $\overline{n}_q$ is the average number of
phonons in the qth mode. At low temperatures ($\hbar\omega \gg k_B T$), there is an exponentially
small probability for a phonon to be present with $\overline{n} \simeq \exp(-\hbar\omega/k_B T)$. Besides, as the
temperature rises and reaches the high temperatures ($k_B T \gg \hbar\omega$), the number of
phonons increases linearly with temperature as $\overline{n} \simeq k_B T/\hbar\omega$. Following the linearized
phonon Boltzmann equation, the phonon contribution can be expressed by employing
Debye's isotropic continuum model within the single-mode relaxation time approxi-
mation as [73].

$$\kappa_{\text{ph}} = \frac{\hbar^2 q_D^5}{6\pi^2 k_B T^2} \sum_s c_s^4 \int_0^1 x^4 \tau_{qs} \bar{n}_{qs} (\bar{n}_{qs} + 1) dx \tag{26}$$

where τ is the phonon relaxation time, c_s is the velocity of phonons for polarization branch s, q_D is the Debye radius, and $x = q/q_D$ is the reduced wave number. Within the Matthiessen's rule, the total contribution to the phonon lifetime is given by

$$\tau_{qs}^{-1} = \sum_i \tau_{qs,i}^{-1} \tag{27}$$

with $\tau_{qs,i}^{-1}$ represents contributions from the ith scattering mechanism. Different scattering rates considered for Mg-based bulk and low-dimensional structured thermoelectric materials can be written as

$$\tau_{qs}^{-1}(\text{total}) = \tau_{qs}^{-1}(\text{bs}) + \tau_{qs}^{-1}(\text{md}) + \tau_{qs}^{-1}(\text{dp}) + \tau_{qs}^{-1}(\text{anh}) + \tau_{qs}^{-1}(\text{ims}) + \tau_{qs}^{-1}(\text{ids}) \tag{28}$$

where scattering mechanisms are sourced from boundary $\tau_{qs}^{-1}(\text{bs})$, mass-defect $\tau_{qs}^{-1}(\text{md})$, deformation potential $\tau_{qs}^{-1}(\text{dp})$, anharmonic $\tau_{qs}^{-1}(\text{anh})$, interface-mass-mixing $\tau_{qs}^{-1}(\text{ims})$, and interface-dislocation $\tau_{qs}^{-1}(\text{ids})$. Theoretical expressions for these phonon scattering mechanisms in bulk, quantum well, and quantum wire structured materials are listed in **Table 3**.

The temperature dependence of thermoelectric figure of merit for bulk $Mg_{3.2-y}Co_y(Sb_{0.3}Bi_{0.7})_{1.99}Te_{0.01}$ (y = 0.05) and its quantum wire structure with the wire widths of d_A = 6, 7, and 8 nm is represented in **Figure 11** with the experimental measurements reported by Ref. [72] for bulk $Mg_{3.2-y}Co_y(Sb_{0.3}Bi_{0.7})_{1.99}Te_{0.01}$ (y = 0.05) sample. As seen from our theoretical results, our thermoelectric transport modeling can successfully explain the experimental measurement of *ZT*; while for the bulk sample the maximum value of *ZT* is theoretically found to be 1.07 at 550 K, its experimental measured value reported as 0.96 at 575 K by Ref. [72]. Additionally, using low dimensional quantum wires structure of $Mg_{3.2-y}Co_y(Sb_{0.3}Bi_{0.7})_{1.99}Te_{0.01}$ (y = 0.05) with different wire widths, the highest value of *ZT* at 600 K can be reached to 5.5, 3.7, and 2.7 for d_A = 6 nm, d_A = 7 nm, and d_A = 8 nm, respectively. Therefore low structured thermoelectric materials warrant dramatically enhanced thermoelectric efficiency compared to bulk materials.

In **Figure 12**, for the comparison the temperature-varied dimensionless figure of merits of n- and p-type Zn_4Sb_3 and Bi_2Te_3 nanowire-based thermoelectric materials, the state-of-the-art bulk and layered structured Sn(Se,S) and Mg-based thermoelectric materials and our theoretical Mg-based quantum wire systems are presented together.

2.1 Summary and future perspectives

Thermoelectric materials are very useful in various types of applications owing to their advantages as already discussed above. One of the current goals in thermoelectric research area is to find new and innovative thermoelectric material systems. During the last decades, a significant advancement in both theoretical and experimental studies has been achieved in the progress of high-efficient thermoelectric materials. Especially, recent advances in nanotechnology have brought with

Scattering mechanism	Expression
Boundary scattering	$\tau_{qs}^{-1}(\text{bs}) = c_s/L$; ($L$: phonon mean free path)
Mass defect scattering	$\tau_{qs}^{-1}(\text{md}) = \dfrac{\Gamma_{\text{md}}\Omega}{4\pi\bar{c}^3}\omega^4(qs)$; $\Gamma_{\text{md}} = \sum_i f_i\left(\dfrac{\Delta M_i}{\overline{M}}\right)^2$ ($\bar{c}$: average phonon speed; f_i: the percentage of ith isotope present in the crystal; $\Delta M_i = M_i - \overline{M}$; $\overline{M} = f_i M_i$)
Deformation potential scattering	$\tau_{qs}^{-1}(\text{dp}) = \dfrac{3}{8\sqrt{\pi}}\dfrac{E_{\text{df}}^2}{\rho c_l^2 \hbar^4}\left(2m_c^* k_B T\right)^{3/2}$ (E_{df}: deformation potential; ρ: mass density; c_l: longitudinal acoustic phonon velocity; m_c^*: effective mass of a charge carrier)
Anharmonic scattering	$\tau_{qs}^{-1}(\text{anh, BULK}) = \dfrac{\hbar q_D^5 \gamma^2}{4\pi\rho\bar{c}^2}\sum_{s's''\epsilon} c_s c_{s'}$ $\left[\left[\displaystyle\int dx' x'^2 x''_+[1 - \epsilon + \epsilon(Cx + Dx')]\dfrac{\bar{n}_{q's'}(\bar{n}''_+ + 1)}{(\bar{n}_{qs}+1)} + \dfrac{1}{2}\int dx' x'^2 x''_-[1 - \epsilon + \epsilon(Cx - Dx')]\dfrac{\bar{n}_{q's'}\bar{n}''_-}{\bar{n}_{qs}}\right]\right]$ (γ: Grüneisen constant; $x' = q'/q_D$; $x''_\pm = Cx \pm Dx'$; $\bar{n}''_\pm = \bar{n}(x''_\pm)$, $C = c_s/c_{s''}$; $D = c_{s'}/c_{s''}$) $\tau_{qs}^{-1}(\text{anh, QWL}) = \tau_{qs}^{-1}(\text{anh, BULK})(n_A + n_B)^{2/3}$ (n_A: number of well layers; n_B: number of barrier layers) $\tau_{qs}^{-1}(\text{anh, QWR}) = 1/A(T)\omega^2$ $A(T) = \dfrac{k_B}{2\pi^2 c \kappa_{\text{ph}}^{\text{BULK}}}\displaystyle\int_0^{\omega_D}\dfrac{(\hbar\omega/k_B T)^2 e^{\hbar\omega/k_B T}}{(e^{\hbar\omega/k_B T}-1)^2}d\omega$
Interface dislocation scattering	$\tau_{qs}^{-1}(\text{ids, QWL}) = \dfrac{\Gamma_{\text{ids}}\Omega}{8\pi\bar{c}^3}\omega_0^4$ $\Gamma_{\text{ids}} = \dfrac{2\beta_0'}{n_A + n_B}\sum_i \exp\left(-\left|\dfrac{l_i - l_0}{d}\right|\right)\left(\dfrac{\Delta M_i}{\overline{M}}\right)^2\left[1 + \left(\dfrac{e_A^2}{e_B^2}\right)^2 + 1 + \left(\dfrac{e_B^2}{e_A^2}\right)^2\right]$ (β_0': the fraction of broken bonds in the interface region.)
Interface mass-mixing scattering	$\tau_{qs}^{-1}(\text{ims, QWL}) = \dfrac{\Gamma_{\text{ims}}\Omega}{4\pi\bar{c}^3}\omega^4(qs)$ $\Gamma_{\text{ims}} = \dfrac{2\beta_0}{n_A + n_B}\sum_i \exp\left(-\left|\dfrac{l_i - l_0}{d}\right|\right)\left(\dfrac{\Delta M_i}{\overline{M}}\right)^2\left[\left(1 - \dfrac{e_A^2}{e_B^2}\right)^2 + \left(1 - \dfrac{e_B^2}{e_A^2}\right)^2\right]$ (d: interlayer distance; l_i: layer distance from interface; $l_0 z$ coordinate of the interface; β_0: mass-mixing fraction at the interface; e_B/e_A the ratio of the amplitudes of eigenvectors in materials B and A.) $\dfrac{e_B}{e_A} = \dfrac{\left[\dfrac{1}{M_0} - \Delta\left(\dfrac{1}{M}\right)\right]\cos(l_z q_z)}{\left\{\left(\dfrac{1}{M_0}\right)^2\cos^2(l_z q_z) + \left[\Delta\left(\dfrac{1}{M}\right)\right]^2\sin^2(l_z q_z)\right\}^{1/2} - \Delta\left(\dfrac{1}{M}\right)}$ $\dfrac{1}{M_0} = \dfrac{1}{2}\left(\dfrac{1}{M_A} + \dfrac{1}{M_B}\right)$; $\Delta\left(\dfrac{1}{M}\right) = \dfrac{1}{2}\left(\dfrac{1}{M_A} - \dfrac{1}{M_B}\right)$; $l_z = d_A + d_B$

Table 3.
Expressions for different phonon scattering mechanisms [65, 73–76].

promising methods that cause fundamental mechanisms to get enhanced thermoelectric efficiencies. In particular, low dimensional quantum well and quantum wire systems are niche applications in electronics as micro- and nano-generators due to a lower energy requirements. Although a tremendous progress has been achieved in the past few years, a number of fundamental questions about theoretical background on thermoelectric transport properties in low-dimensional systems still need to be
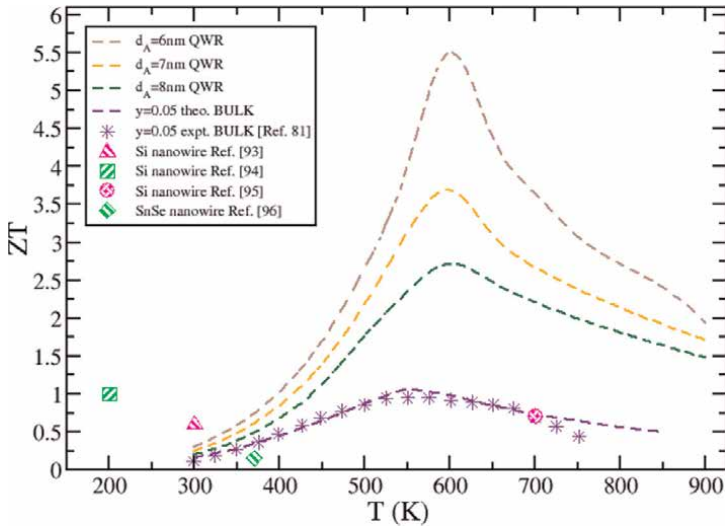
Figure 11.
Temperature dependence of thermoelectric figure of merit ZT for bulk $Mg_{3.2-y}Co_y(Sb_{0.3}Bi_{0.7})_{1.99}Te_{0.01}$ (y = 0.05) and its quantum wire structure with the wire widths of d_A = 6, 7, and 8 nm. Dashed lines are our theoretical calculations and the symbols are the experimental measurements done by Refs. [72, 77–80].
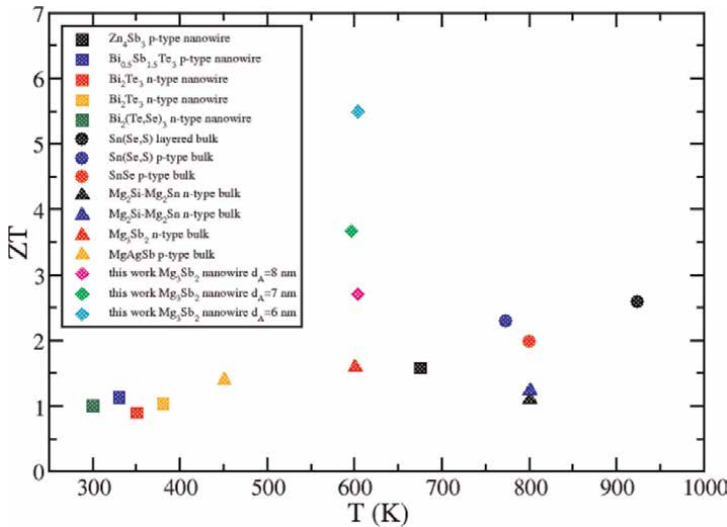
Figure 12.
Comparison of the dimensionless figure of merit for Mg-based nanowire structured thermoelectric materials reported in this work with n- and p-type Zn_4Sb_3 and Bi_2Te_3 nanowire-based thermoelectric materials [81–85], and the state of the art bulk and layered structured Sn(Se,S) and Mg-based thermoelectric materials [25, 47, 86–90] in the literature.

investigated. Therefore, in this book chapter, we aim to explore the temperature variation of the thermoelectric transport properties of bulk and low dimensional materials systematically. We first start our theoretical investigation with the temperature-dependent Fermi level both in extrinsic and intrinsic regimes. Following the linearized Boltzmann transport equations the temperature variant electronic transport properties under the energy-dependent relaxation time approximation are

discussed for bulk and low dimensional systems. The thermal conductivity contributions from bipolar and phonon mechanisms are also discussed in detail. Phonon scattering rates sourced from boundaries, mass defects, anharmonicity, deformation potential, interface mass-mixing, and dislocation are given rigorously.

Among thermoelectric materials Mg-based thermoelectric materials have attracted intense interests owing to their enhanced *ZT* values at low-to-medium temperature range, together with the non-toxic, low-cost, earth abundant, low-density, and environmentally friendly. Here some major outlooks are listed:

    i. Mg-based compounds show highly degenerated conduction bands and can be alloyed and/or doped to form a wide range of compositions, providing enhanced *ZT* values.

    ii. Thermoelectric devices, applied for both power generation and refrigeration, have been successfully fabricated using Mg-based materials and can obtain high conversion efficiency.

    iii. Low-dimensional Mg-based systems (quantum wells and quantum wires) suggest even more enhanced *ZT* values than bulk systems with the help of quantum confinement effect.

    iv. As stated above, the main reason having higher ZT values in low-dimensional systems is having extremely low phonon thermal conductivity and high thermoelectric power factor at the same time.

    v. Since there are more intensely experimental studies in Mg-based thermoelectric materials in the literature it is essential to imply further theoretical investigations on Mg-based thermoelectric devices. Therefore, this chapter will be a possible guide to focus on thermoelectric transport properties of Mg-based bulk and low-dimensional systems.

Investigations on thermoelectric transport properties both in bulk and low-dimensional materials are becoming more prominent for solving today's energy challenges. Collabrations from scientists among different areas such as materials science, physics, and chemistry will have clear advantages in this global competition owing to interdisciplinary nature of thermoelectric research. In the light of these outlooks, developing Mg-based thermoelectric devices are well worthy of systematic study which should speed up their practical applications for energy harvesting. Hereby, the present book chapter comprises an overview of fundamental attainments and breakthroughs in experimental and theoretical thermoelectric research based on Mg-based materials. By presenting a detailed theoretical background on Mg-based 3D, 2D, and 1D systems it is clear that using low-dimensional systems certainly helps us to reach higher thermoelectric efficiencies. This also encourages experimentalists to use low dimensional structured Mg-based systems more often in new-generation thermoelectric devices.

Acknowledgements

Conflict of interest

The authors declare no conflict of interest.

Author details

Övgü Ceyda Yelgel
Department of Electrical-Electronics Engineering, Recep Tayyip Erdoğan University, Rize, Turkey

*Address all correspondence to: oceyda.yelgel@erdogan.edu.tr

IntechOpen

References

[1] Rowe DM. Thermoelectrics Handbook. Boca Raton: CRC Press; 2005

[2] Poudel B, Hao Q, Ma Y, Lan Y, Minnich A, Yu B, et al. High-thermoelectric performance of nanostructured bismuth antimony telluride bulk alloys. Science. 2008;**320**:634

[3] Uher C. Materials Aspect of Thermoelectricity. USA Boca Raton: CRS Press Taylor & Francis Group; 2017

[4] Kraemer D, Poudel B, Feng H-P, Caylor JC, Yu B, Yan X, et al. High performance flat-panel solar thermoelectric generators with high thermal concentration. Nature Materials. 2011;**10**:532

[5] Mahan G, Sales B, Sharp J. Thermoelectric materials: New approaches to an old problem. Physics Today. 1997;**50**:42

[6] Zhang Y, Chu Y, Xing W, Zheng L, Cao Y. Mechanical properties of thermoelectric Mg_2Si using molecular dynamics simulations. Mechanics of Advanced Materials and Structures. 2017;**0**:1-6

[7] DiSalvo FJ. Thermoelectric cooling and power generation. Science. 1999;**285**:703

[8] Bell LE. Cooling, heating, generating power, and recovering waste heat with thermoelectric systems. Science. 2008;**321**:1457

[9] Szczech JR, Higgins JM, Jin S. Enhancement of the thermoelectric properties in nanoscale and nanostructured materials. Journal of Materials Chemistry. 2011;**21**:4037

[10] Rowe DM. Applications of nuclear-powered thermoelectric generators in space. Applied Energy. 1991;**40**:241

[11] Vandersande JW, Fleurial JP. Thermal management of power electronics using thermoelectric coolers. In: Fifteenth International Conference of Thermoelectrics Proceedings—ICT '96. Vol. **252**. Pasadena, CA. 1996. p. 255

[12] Majumdar A. Materials science: Enhanced: Thermoelectricity in semiconductor nanostructures. Science. 2004;**303**:777

[13] Heremans JP, Jovovic V, Toberer ES, Saramat A, Kurosaki K, Charoenphakdee A, et al. Enhancement of thermoelectric efficiency in PbTe by distortion of the electronic density of states. Science. 2008;**321**(5888):554

[14] Biswas K, He J, Blum ID, Wu CI, Hogan TP, Seidman DN, et al. High-performance bulk thermoelectrics with all-scale hierarchical architectures. Nature. 2012;**489**(7416):414

[15] Pei Y, Shi X, LaLonde A, Wang H, Chen L, Snyder GJ. Convergence of electronic bands for high performance bulk thermoelectrics. Nature. 2011; **473**(7345):66

[16] Heremans JP, Thrush CM, Morelli DT. Thermopower enhancement in lead telluride nanostructures. Physical Review B. 2004;**70**(11):115334

[17] Liu W, Tan X, Yin K, Liu H, Tang X, Shi J, et al. Convergence of conduction bands as a means of enhancing thermoelectric performance of n-type $Mg_2Si_{1-x}Sn_x$ solid solutions. Physical Review Letters. 2012;**108**:166601

[18] Zhao LD, Wu HJ, Hao SQ, Wu CI, Zhou XY, Biswas K, et al. All-scale hierarchical thermoelectrics: MgTe in PbTe facilitates valence band convergence and suppresses bipolar thermal transport for high performance. Energy and Environmental Science. 2013;**6**:3346

[19] Banik A, Shenoy US, Anand S, Waghmare UV, Biswas K. Mg alloying in SnTe facilitates valence band convergence and optimizes thermoelectric properties. Chemistry of Materials. 2015;**27**:581

[20] Bahk J-H, Bian Z, Shakouri A. Electron energy filtering by a nonplanar potential to enhance the thermoelectric power factor in bulk materials. Physical Review B. 2013;**87**:75204

[21] Shakouri A, LaBounty C, Abraham P, Piprek J, Bowers JE. Enhanced thermionic emission cooling in high barrier superlattice heterostructures. MRS Proceedings. 1998;**545**:449

[22] Zhang Q, Liao B, Lan Y, Lukas K, Liu W, Esfarjani K, et al. High thermoelectric performance by resonant dopant indium in nanostructured SnTe. Proceedings of National Academy of Sciences. 2013;**110**:13261

[23] Biswas K, He J, Zhang Q, Wang G, Uher C, Dravid VP, et al. Strained endotaxial nanostructures with high thermoelectric figure of merit. Nature Chemistry. 2011;**3**:160

[24] Zhao L-D, Hao S, Lo S-H, Wu C-I, Zhou X, Lee Y, et al. High thermoelectric performance via hierarchical compositionally alloyed nanostructures. Journal of the American Chemical Society. 2013;**135**:7364

[25] Zhao L-D, Lo S-H, Zhang Y, Sun H, Tan G, Uher C, et al. Ultralow thermal conductivity and high thermoelectric figure of merit in SnSe crystals. Nature. 2014;**508**:373

[26] Morelli DT, Jovovic V, Heremans JP. Intrinsically minimal thermal conductivity in cubic $I-V-VI_2$ semiconductors. Physical Review Letters. 2008;**101**:35901

[27] Guin SN, Chatterjee A, Negi DS, Datta R, Biswas K. High thermoelectric performance in tellurium free p-type $AgSbSe_2$. Energy and Environmental Science. 2013;**6**:2603

[28] Guin SN, Pan J, Bhowmik A, Sanyal D, Waghmare UV, Biswas K. Temperature dependent reversible p–n–p type conduction switching with colossal change in thermopower of semiconducting AgCuS. Journal of American Chemical Society. 2014;**136**: 12712

[29] Hicks LD, Dresselhaus MS. Effect of quantum-well structures on the thermoelectric figure of merit. Physical Review B. 1993;**47**:12727

[30] Venkatasubramanian R, Siivola E, Colpitts T, O'Quinn B. Thin-film thermoelectric devices with high room-temperature figures of merit. Nature. 2001;**413**:597

[31] Harman TC, Taylor PJ, Walsh MP, LaForge BE. Quantum dot superlattice thermoelectric materials and devices. Science. 2002;**297**:2229

[32] Harman T, Walsh M, Turner G. Nanostructured thermoelectric materials. Journal of Electronic Materials. 2005;**34**:L19

[33] Heremans JP, Wiendlocha B, Chamoire AM. Resonant levels in bulk thermoelectric semiconductors. Energy & Environmental Science. 2012;**5**:5510

[34] Miraz MH, Ali M, Excell PS, Picking RA. Review on internet of things (IoT). In: Internet of Everything (IoE) and Internet of Nano Things (IoNT). Internet Technologies and Applications (ITA). New York, USA: IEEE; 2015. p. 219

[35] Hiremath S, Yang G, Mankodiya K. Wearable internet of things: Concept, architectural components and promises for person-centered healthcare. In: 4th International Conference on Wireless Mobile Communication and Healthcare-Transforming Healthcare through Innovations in Mobile and Wireless Technologies (MOBIHEALTH). New York, USA: IEEE; 2014. p. 304

[36] Hung NT, Nugraha AR, Yang T, Saito R. Confinement effect in thermoelectric properties of two-dimensional materials. MRS Advances. 2020;**5**(10):469

[37] Haras M, Skotnicki T. Thermoelectricity for IoT—A review. Nano Energy. 2018;**54**:461

[38] Suarez F, Nozariasbmarz A, Vashaee D, Öztürk MC. Designing thermoelectric generators for self-powered wearable electronics. Energy & Environmental Science. 2016;**9**(6):2099

[39] Hyland M, Hunter H, Liu J, Veety E, Vashaee D. Wearable thermoelectric generators for human body heat harvesting. Applied Energy. 2016;**182**: 518

[40] Santos R, Yamini SA, Dou SX. Recent progress in magnesium-based thermoelectric materials. Journal of Materials Chemistry A. 2018;**6**:3328

[41] Pei YZ, Wang H, Snyder GJ. Band engineering of thermoelectric materials. Advanced Materials. 2012;**24**:6125

[42] Zhang Q, Li X, Kang Y, Zhang L, Yu D, He J, et al. High pressure synthesis of Te-doped $CoSb_3$ with enhanced thermoelectric performance. Journal of Materials Science: Materials in Electronics. 2014;**26**:385

[43] Gelbstein Y, Davidow J, Girard SN, Chung DY, Kanatzidis M. Controlling metallurgical phase separation reactions of the $Ge_{0.87}Pb_{0.13}Te$ alloy for high thermoelectric performance. Advanced Energy Materials. 2013;**3**:815

[44] Morris RG, Redin RD, Danielson GC. Semiconducting properties of Mg_2Si single crystals. Physical Review. 1958;**109**:1909

[45] Heller MW, Danielson GC. Seebeck effect in Mg_2Si single crystals. Journal of Physics and Chemistry of Solids. 1962;**23**: 601

[46] Zaitsev VK, Fedorov MI, Gurieva EA, Eremin IS, Konstantinov PP, Samunin AY, et al. Thermoelectrics of n-type with ZT>1 based on Mg_2Si-Mg_2Sn solid solutions. In: ICT 2005 24th International Conference on Thermoelectrics. 2005. p. 204

[47] Zaitsev VK, Fedorov MI, Gurieva EA, Eremin IS, Konstantinov PP, Samunin AY, et al. Highly effective $Mg_2Si_{1-x}Sn_x$ thermoelectrics. Physical Review B. 2006;**74**:045207

[48] Zhou Z, Han G, Lu X, Wang G, Zhou X. High-performance magnesium-based thermoelectric materials: Progress and challenges. Journal of Magnesium and Alloys. 2022;**10**:1719

[49] Tani J, Kido H. Thermoelectric properties of Bi-doped Mg_2Si semiconductors. Physica B: Condensed Matter. 2005;**364**:218

[50] Gao HL, Zhu TJ, Zhao XB, Deng Y. Influence of Sb doping on thermoelectric properties of Mg_2Ge materials. Intermetallics. 2015;**56**:33

[51] Mars K, Ihou-Mouko H, Pont G, Tobola J, Scherrer H. Thermoelectric properties and electronic structure of Bi- and Ag-doped $Mg_2Si_{1-x}Ge_x$ compounds. Journal of Electronic Materials. 2009;**38**: 1360

[52] Zhang Q, Yin H, Zhao XB, He J, Ji XH, Zhu TJ, et al. Thermoelectric properties of n-type $Mg_2Si_{0.6-y}Sb_ySn_{0.4}$ compounds. Physica Status Solidi A. 2008;**205**:1657

[53] Liu W, Kim HS, Chen S, Jie Q, Lv B, Yao M, et al. N-type thermoelectric material $Mg_2Sn_{0.75}Ge_{0.25}$ for high power generation. In: Proceedings of the National Academy of Sciences of U.S.A. 2015;**112**:3269

[54] Yin K, Su X, Yan Y, You Y, Zhang Q, Uher C, et al. Optimization of the electronic band structure and the lattice thermal conductivity of solid solutions according to simple calculations: A canonical example of the $Mg_2Si_{1-x-y}Ge_xSn_y$ ternary solid solution. Chemistry of Materials. 2016;**28**:5538

[55] An T-H, Park C, Seo W-S, Choi S-M, Kim I-H, Kim S-U. Enhancement of p-type thermoelectric properties in an Mg_2Sn system. Journal of Korean Physical Society. 2012;**60**:1717

[56] Ihou-Mouko H, Mercier C, Tobola J, Pont G, Scherrer H. Thermoelectric properties and electronic structure of p-type Mg_2Si and $Mg_2Si_{0.6}Ge_{0.4}$ compounds doped with Ga. Journal of Alloys and Compounds. 2011;**509**:6503

[57] Zhang Q, Cheng L, Liu W, Zheng Y, Su X, Chi H, et al. Low effective mass and carrier concentration optimization for high performance p-type $Mg_{2(1-x)}Li_{2x}Si_{0.3}Sn_{0.7}$ solid solutions. Physical Chemistry Chemical Physics. 2014;**16**:23576

[58] De Boor J, Saparamadu U, Mao J, Dahal K, Müller E, Ren Z. Thermoelectric performance of Li doped, p-type $Mg_2(Ge,Sn)$ and comparison with $Mg_2(Si,Sn)$. Acta Materialia. 2016;**120**:273

[59] Zhang Q, He J, Zhu TJ, Zhang SN, Zhao XB, Tritt TM. High figures of merit and natural nanostructures in $Mg_2Si_{0.4}Sn_{0.6}$ based thermoelectric materials. Applied Physics Letters. 2008; **93**:102109

[60] Liu W, Tang XF, Li H, Yin K, Sharp J, Zhou XY, et al. Enhanced thermoelectric properties of n-type $Mg_{2.16}(Si_{0.4}Sn_{0.6})_{1-y}Sb_y$ due to nano-sized Sn-rich precipitates and an optimized electron concentration. Journal of Materials Chemistry. 2012;**22**: 13653

[61] Ning H, Mastrorillo GD, Grasso S, Du B, Mori T, Hu C, et al. Enhanced thermoelectric performance of porous magnesium tin silicide prepared using pressure-less spark plasma sintering. Journal of Materials Chemistry A. 2015;**3**: 17426

[62] Ozen M, Yahyaoglu M, Candolfi C, Veremchuk I, Kaiser F, Burkhardt U, et al. Enhanced thermoelectric performance in $Mg_{3+x}Sb_{1.5}Bi_{0.49}Te_{0.01}$ via engineering microstructure through melt-centrifugation. Journal of Materials Chemistry A. 2021;**9**:1733

[63] Zhang JW, Song LR, Iversen BB. Probing efficient n-type lanthanide dopants for Mg_3Sb_2 thermoelectrics. Advanced Science. 2020;**7**:2002867

[64] Mao J, Liu Z, Ren Z. Size effect in thermoelectric materials. NPJ Quantum Materials. 2016;**1**:16028

[65] Yelgel ÖC, Srivastava GP. Thermoelectric properties of n-type $Bi_2(Te_{0.85}Se_{0.15})_3$ single crystals doped with CuBr and SbI_3. Physical Review B. 2012;**85**:125207

[66] Yelgel ÖC, Srivastava GP. Thermoelectric properties of $Bi_2Se_3/Bi_2Te_3/Bi_2Se_3$ and $Sb_2Te_3/Bi_2Te_3/Sb_2Te_3$ quantum well systems. Philosophical Magazine. 2014;**94**:2072

[67] Ziman JM. Electrons and Phonons: The Theory of Transport Phenomena in Solids. Great Britain: Oxford University Press; 2001

[68] Richard F. Semiconductor Physics and Applications. Great Britain: Oxford University Press; 2000

[69] Tritt TM. Thermal Conductivity: Theory, Properties, and Applications. New York: Kluwer Academic/Plenum Publishers; 2004

[70] Yu PY, Cardona M. Fundamentals of Semiconductors : Physics and Materials Properties. London: Springer; 2010

[71] Wilson AH. The Theory of Metals. Great Britain: Cambridge University Press; 2011

[72] Chen Y, Wang C, Ma Z, Li L, Li S, Wang J. Improved thermoelectric performance of n-type Mg_3Sb_2-Mg_3Bi_2 alloy with Co element doping. Current Applied Physics. 2021;**21**:25

[73] Srivastava GP. The Physics of Phonons. Bristol: Adam Hilger; 1990

[74] Yelgel ÖC. Chapter6: Recent Advances on Mg_2X^{IV} based Thermoelectric Materials: A Theoretical Approach. U.S.A: John Wiley & Sons, Inc; 2019

[75] Landry ES, McGaughey AJH. Effect of interfacial species mixing on phonon transport in semiconductor superlattices. Physical Review B. 2009;**79**:75316

[76] Hepplestone SP, Srivastava GP. Theory of interface scattering of phonons in superlattices. Physical Review B. 2010;**82**:144303

[77] Al H, Chen R, Delgado RD, Liang W, Garnett EC, Najarian M, et al. Enhanced thermoelectric performance of rough silicon nanowires. Nature. 2008;**451**(7175):163

[78] Al B, Bunimovich Y, Tahir-Kheli J, Yu JK, Goddard WA III, Heath JR. Silicon nanowires as efficient thermoelectric materials. Nature. 2008;**451**(7175):168

[79] Yang L, Huh D, Ning R, Rapp V, Zeng Y, Liu Y, et al. High thermoelectric figure of merit of porous Si nanowires from 300 to 700 K. Nature Communications. 2021;**12**:3926

[80] Hernandez JA, Ruiz A, Fonseca LF, Pettes MT, Yacaman MJ, Benitez A. Thermoelectric properties of SnSe nanowires with different diameters. Scientific Reports. 2018;**8**:11966

[81] Liu Y-B, Zhou S-M, Yuan X-Y, Lou S-Y, Gao T, Shi X-J, et al. Synthesis and high-performance thermoelectric properties of beta-Zn_4Sb_3 nanowires. Materials Letters. 2012;**84**:116

[82] Li L, Xu S, Li G. Enhancement of thermoelectric properties in Bi–Sb–Te alloy nanowires by pulsed electrodeposition. Energy Technology. 2015;**3**:825

[83] Chen C-L, Chen Y-Y, Lin S-J, Ho JC, Lee P-C, Chen C-D, et al. Fabrication and characterization of electrodeposited bismuth telluride films and nanowires.

Journal of Physical Chemistry C. 2010;
114:3385

[84] Zhang G, Kirk B, Jauregui LA, Yang H, Xu X, Chen YP, et al. Rational synthesis of ultrathin n-type Bi_2Te_3 nanowires with enhanced thermoelectric properties. Nano Letters. 2011;**12**:56

[85] Tan M, Deng Y, Wang Y. Ordered structure and high thermoelectric properties of $Bi_2(Te, Se)_3$ nanowire array. Nano Energy. 2014;**3**:144

[86] Peng KL, Zhang B, Wu H, Cao XL, Li A, Yang DF, et al. Ultra-high average figure of merit in synergistic band engineered $Sn_xNa_{1-x}Se_{0.9}S_{0.1}$ single crystals. Materials Today. 2018;**21**:501

[87] Peng KL, Lu X, Zhan H, Hui S, Tang XD, Wang GW, et al. Broad temperature plateau for high ZTs in heavily doped p-type SnSe single crystals. Energy & Environmental Science. 2016;**9**:450

[88] Tan XJ, Liu W, Liu HJ, Shi J, Tang XF, Uher C. Multiscale calculations of thermoelectric properties of n-type $Mg_2Si_{1-x}Sn_x$ solid solutions. Physical Review B. 2012;**85**:205212

[89] Zhang JW, Song LR, Sist M, Tolborg K, Iversen BB. Chemical bonding origin of the unexpected isotropic physical properties in thermoelectric Mg_3Sb_2 and related materials. Nature Communications. 2018;**9**:4716

[90] Zhao HZ, Sui JH, Tang ZJ, Lan YC, Jie Q, Kraemer D, et al. High thermoelectric performance of MgAgSb based materials. Nano Energy. 2014;**7**:97

Chapter 4

Dissolvable Magnesium Alloys in Oil and Gas Industry

Lei Zhao, Timothy Ryan Dunne, Jiaxiang Ren and Peng Cheng

Abstract

Invented and continuously optimized during two decades of the shale revolution that completely transformed the global energy market, dissolvable magnesium (DM) alloy technology has advanced significantly in both performance improvement and cost reduction, and thousands of tons of Mg alloy are consumed annually by oil and gas industry to fabricate downhole tools, including dissolvable hydraulic frac plugs. In this book chapter, every aspect of this technology will be reviewed, including history, development routes, manufacturing process, dissolving mechanism and control, failure analysis and prevention, influence of environments, delayed coating, field experience, etc., and outlook will be provided at the end for future development.

Keywords: dissolvable magnesium, temporary coating, frac plug, hydraulic fracturing, high-temperature magnesium alloy

1. Introduction

The world's first oil well was drilled in Titusville, Pennsylvania by Edwin Drake in 1859, producing a mere 40 barrels a day [1]. Drake's success inspired the continued exploration of oil in the United States as well as globally. A period from the 1930s to the 1960s led to the discovery of many of the world's largest oilfields. However, from 2000 to 2022, no discovered oilfield has exceeded the proven reserves of any existing top 20 giant conventional oilfields [2]. The International Energy Agency (IEA) shows all conventional global oil production plateaued around 2005. Despite the global decline from conventional oilfields, global supply has increased and actually outstripped increased demand in the past 20 years [3].

Aside from advancements in enhanced oil recovery (EOR) methods increasing production, unconventional resources became a major source of global oil supply in the past two decades. Previously disregarded unconventional shale oilfields with permeabilities magnitudes less than conventional oilfields became economical by hydraulically fracturing horizontal wells [4]. Drilling through oil-bearing shale layers increases the reservoir exposure to the wellbore. Hydraulic fracturing involves an array of reciprocating positive displacement pumps over-pressuring the reservoir in the vicinity of the wellbore to create new fractures or open existing ones. Sand is pumped into the resultant fractures to create high permeability pathways in shale. Shale has permeabilities orders of magnitude less than conventional formations [5].

Permeability is a controlling factor on how much fluid may be produced from the reservoir; a higher permeability leads to higher production. The fracturing operation is repeated along the wellbore in targeted zones, increasing the overall production of the well, thus creating economically viable wells from previously marginal formations. During fracturing, zones are isolated from one another by a plug, which is conveyed downhole and allows the over-pressuring [6].

The first plugs were made of cast iron that needed coiled tubing to drill through after fracturing to reestablish communication downhole and start production at the wellhead. Composite plugs supplanted cast iron plugs as composite mills quicker than iron [7]. A major advancement was made during the past decade in the creation of dissolvable frac plugs, which react in situ, thus eliminating the need for coiled tubing. Eliminating coiled tubing also allows for zonally isolating longer horizontal sections that would otherwise be impossible to mill [8]. This technology has reshaped the market landscape of shale oil/gas development, and its success is the result of invention of advanced dissolvable magnesium alloy (**Figure 1**).

Development and application of dissolvable Mg alloy is a relatively new technology in oil and gas business. It was invented by US service companies and optimized worldwide by research institutions and alloy companies to improve property and reduce cost. The first mainstream application reported is a dissolvable ball, developed by Baker Hughes in 2010 to activate downhole equipment [9]. Before that, this ball must be milled out or flow back to start well production, and the application of this self-disappearing technology saves operators significant amount of lead time and thus operation cost. In the early stage, expensive powder metallurgy (PM) method is used to form the perfect galvanic cell structure. In a typical manufacturing process, high chemical potential metals, such as Ni, Fe, etc., are coated on the Mg alloy powder surface and then sintered together through an industrial hot isostatic pressing (HIP) process. Since Mg alloys are soft, certain enhancement phases are added to improve mechanical strength. As shown in **Figure 2**, Mg and Ni alloy phase form nearly perfect galvanic cell structures. Its physical properties and dissolving speed can be systematically tuned. This technology achieved significant commercial success, and lots of
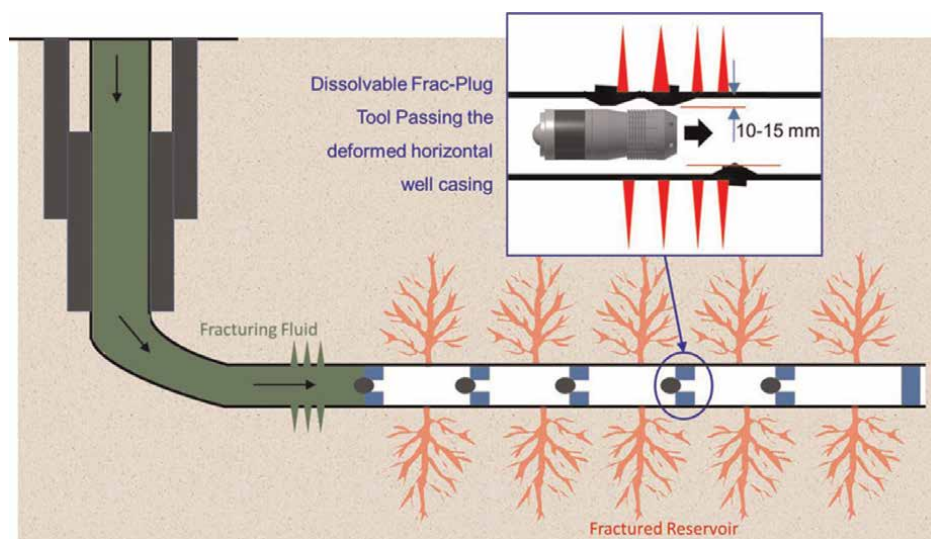
Figure 1.
Schematic of a hydraulically fractured horizontal well [9].
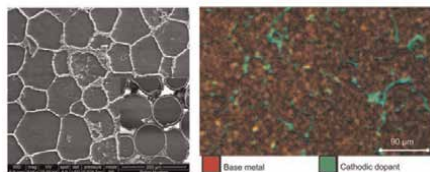
Figure 2.
SEM micrograph of DM material made by powder metallurgy method (left image, [10]). The inset shows a cross-section view of as coated matrix powders before compaction. SEM-EDS image of DM alloy developed by Halliburton (right image, [11]).

companies followed with their own formulations and process method. Given its success, this method still suffers from following issues:

1. High cost: This technology requires atomization of Mg alloys, advanced coating method, and HIP process, all of which are not cost-efficient for oil and gas business where product is a commodity.

2. Low ductility: DM made from PM method usually have low elongation (typically <3%), which is not an issue for ball shape product that does not requires plastic deformation but is not applicable for other parts of plug that requires much higher ductility (**Figure 3**).

With the frame of powder metallurgy, another low-cost processing method was used to reduce the cost. For example, powder mixing method is used to replace chemical vapor deposition (CVD) coating, cold compaction followed by hot extrusion is used to replace expensive HIP process, etc. Product price of DM alloy quickly drops thanks to the consolidation and severe competition between oil and gas service providers. However, these alloys can still not be used by other mechanical parts that require reasonable amount of ductility until a cheap casting method was introduced into market by Halliburton. Their work shows that DM alloy can be made by traditional direct casting and post-heat treatment. The galvanic cell is formed by controlled phase segregation of high chemical potential metals at Mg alloy grain boundaries (**Figure 2**). Therefore, atomized metal powder is no longer needed, and cost of DM alloy is close to other commercial-grade Mg alloys. Most importantly, reasonable ductility is finalized and achieved, and all dissolvable plugs (**Figure 4**) are introduced by various oil and gas providers including Baker Hughes, Halliburton, NOV, etc.

Like most commercial Mg alloys, DM alloy also suffers from strength loss when temperature is above 120°C and cannot be used for high-temperature wells that could reach 220°C. Therefore, various kinds of a rare-earth elements were further
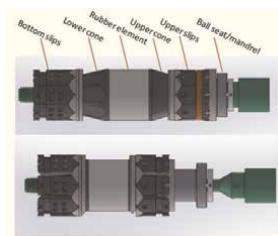
Figure 3.
Labeled plug before actuation (top) and actuated (bottom).

Company	Schlumberger	Halliburton[10]	Baker Hughes[31]	Vitai Oil and Gas Energy Group	MAGNUM	Petrochina Exploration Institute[32]	Petro-king oil	New dissolvable frac plug
Product	Infinity	Illusion	SPECTRE	WIZARD /CHAMELEON™	MVP	SHARK	Thunder Cloud series II	Y257R-103-70
Materials	Aluminum-based metal	Aluminum base + dissolvable rubber cartridge	Electrolytic nano metal + polyurethane rubber cylinder	Magnesium aluminum alloy + dissolvable rubber or plastic rubber cylinder[33]	Biodegradable material + ethylene glycol polymer/polymer cartridge	Magnesium base metal+dissolvable rubber.	Magnesium aluminum alloy + dissolvable rubber	Magnesium base alloy + composite coating + water dissolvable/degraded rubber cylinder
Mechanical structure	Single slip+tee +ball	Bidirectional slip + partitioned inlaid ceramic grain slip	Unidirectional slip + integral non - valves nickel - base alloy coated tile	Single/bi-directional slip + split inlaid cast iron slip	Bidirectional slip + partitioned inlaid alloy grain slip	Bidirectional slip + partitioned prefabricated fragment slip	Bidirectional slip + partitioned slip	Unidirectional slip + integral half petal inserts ceramic grain slip
Sealing element structure	Tee/ball metal seal		Barrel type single rubber drum seal			Barrel type three rubber drum seal	Barrel type single rubber drum seal	Recessed single rubber drum seal
Product dimensions	Φ112.7xΦ 82.30x240	Φ111.1xΦ44x4 43	Φ111.1xΦ38x 550	CHAMELEON™ Φ111xΦ35x460	Φ104.8xΦ2 2.4x437	Φ110xΦ28x680	Φ110xΦ35x6 00	Φ103xΦ43x430
Matter								

Figure 4.
Comparison of characteristics of similar dissolvable frac plugs [12].

introduced from thermally stable precipitates. Certain rare metals have been found to increase elongation of DM alloy to almost 30%, making metal-to-metal seal application possible. To answer oil price downturn from since, manufacturing of DM alloy started to move to China, where rare-earth resource is abundant and Mg production is dominated. DM alloy is no longer an expensive high-end material but a commodity accessible for all oil and gas service providers around the world to develop various kinds of applications besides hydraulic fracturing plugs.

2. Dissolvable magnesium design, processing, and mechanism

2.1 Dissolvable frac plug

Dissolvable plugs are composed of one or more materials that react when in the wellbore. The current generation of polymers used in plugs, mostly polyglycolic acid (PGA), are limited from 80 to 130°C. Magnesium is the typical choice for metallic plug components in windows of 40 to 175°C. Operators generally require plug functionality for eight hours, with complete dissolution occurring within 15 days [12]. The general operating principles of a frac plug are to convey it from the surface to the targeted zone, actuate it to set in the casing, and achieve a tight seal that is to be held for one to 24 hours, after which it is left to dissolve so that production may start. Pressure is built by conveying a ball down to the plug, where it will seat, blocking the inner diameter that is the final possible path of communication between the surface and the area below the plug.

Generally, a plug will have an angled recess at the top of the plug, which operates as the ball seat. Many designs integrate the ball seat into the mandrel, a hollow tube that the other components are assembled on. The setting tool is connected to the plug through this component. The setting tool supplies the force that pushes the parts

together on the mandrel, increasing the plug diameter due to a ramp design that forces the slips and elements into contact with the casing (**Figure 3**). The slips have small hard teeth that penetrate the casing, anchoring the plug to the casing. Petal designs of slips can come in an upper and lower pair. Other designs may utilize a barrel slip design. The element is typically made of dissolvable rubber, although some plugs utilize a metal-to-metal seal design (**Figure 3**). The element seals the outer diameter between the casing and the plug. A bottom cap is used to secure all components on the assembly during deployment.

Requirements for the plug material vary widely depending on the operator, design, temperature, fluid, and individual component requirements. At a given temperature on a plug, one component may require high ductility whereas another requires high strength. The same plug design functioning at 95°C may be inadequate at 175°C due to deteriorated mechanical properties or accelerated corrosion of the base alloy. Materials with a wide array of properties must be available to match the varying wellbore conditions. The rate of development for new formulations can be outstripped by delivery dates for product. That is why each oil service providers have their own material grades or plug designs to meet requirements of specific well conditions or markets (**Figure 4**).

2.2 Dissolution mechanism and dissolving dynamics

2.2.1 Galvanic cell structure

Dissolvable magnesium alloys rely on intercellular galvanic corrosion induced by noble impurities in chloride-bearing wellbore fluids. The dissolution rate is controlled by the type and fraction of secondary phases in the matrix. Beyond determining mechanical properties, the secondary phases are more cathodic than the magnesium matrix, causing hydrogen gas and magnesium ions to form as a byproduct of the reaction [13]. The reaction proceeds as follows, typically in a brine solution:

$$Mg + 2H_2O \rightarrow Mg(OH)_2 + H_2 \text{ (gas)} + \text{heat} \tag{1}$$
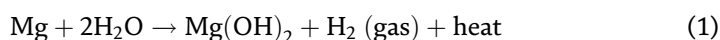
Figure 5 shows galvanic series of various metals and alloys, which determines their nobility. When two metals are submerged in an electrolyte, while also electrically connected by some external conductor, the less noble (base) will experience galvanic corrosion. Magnesium is the least noble structural metal and can form a galvanic cell with almost any of the metals/alloys in the series. Therefore, it is possible to mix it with noble metals to form dissolvable alloys based on galvanic corrosion. It is reported that Fe powder [15] or Ni powder [16] can be mixed during melting and casting process to make dissolvable alloys for oil and gas industry. Also, a powder-metallurgy-like structure including a relatively reactive metal or alloy can be combined with other compositions to develop galvanic couples [17]. Additions of copper and/or nickel to magnesium will create a meaningful accelerated corrosion rate that may be tuned to the application temperature and salinity. For example, a composition can include an alloy of magnesium or aluminum that is combined with one or more of Cu, Fe, and Ni, among a few transition-metal elements to develop galvanic couples. Copper and nickel form high electropotential intermetallic compounds along the grain boundaries of the magnesium matrix phase. These noble intermetallic act as an archipelago of cathodes, accelerating the corrosion of the magnesium alloy.
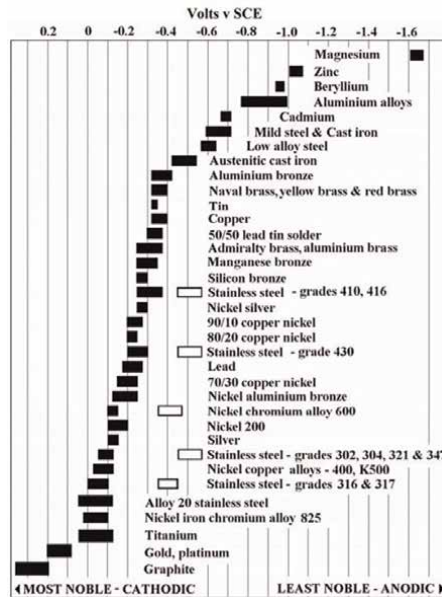
Figure 5.
Galvanic series (or electropotential series) of metals and alloys [14].

2.2.2 Environmental dynamics: influence of temperature, salinity, and dissolved gas

The reaction kinetics of the dissolution mechanism of magnesium has a clear dependence on temperature and salinity. Taking one of our dissolvable magnesium alloy grades AZ31–1, for example, for the reaction to proceed, some chloride must be present, as evidenced in **Figure 6**. Tap water has a very small amount of chloride that allows the reaction to proceed, albeit at a slow rate. Increasing the chloride concentration leads to a nonlinear increase in the dissolution rate. For a given chloride
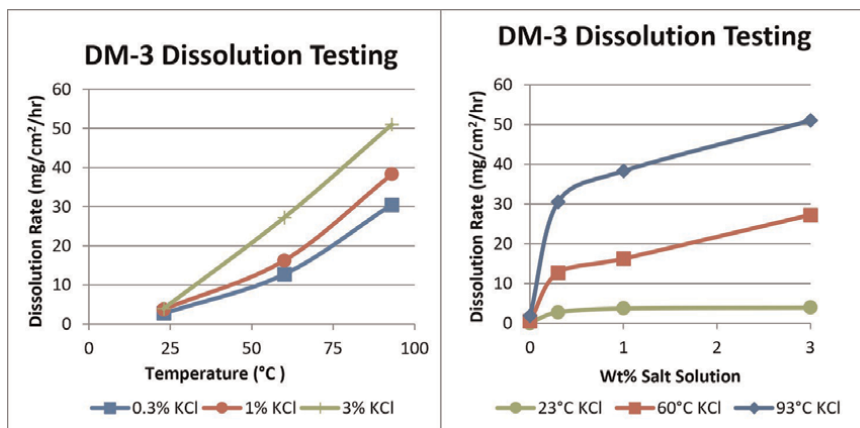
Figure 6.
Dissolution of alloy AZ31–1 in tap water, 0.3 wt% KCl, 1 wt% KCl, and 3 wt% KCl at 23°C, 60°C, and 93°C, respectively. The chart on the left shows the dissolution rate as a function of salinity. The righthand chart demonstrates the dissolution rate as a function of temperature. Measurements performed by CNPC USA.

concentration, the reaction rate is close to linear with increasing temperature. Due to the increasing rate, material is developed for different temperature applications, or specialized coating is applied to ensure sufficient operational life.

Besides salinity and temperature of fluids, dissolved gas also plays a key role but is often ignored by application engineers. Estimates on how quickly a plug will dissolve in the lab are often much shorter than what is measured in the field. After years of studying the dissolution rate in the traditional water bath method, that is measuring weight loss after soaking in water bath for a certain period of time, a comparison was made for testing an alloy in several ways while maintaining a temperature of 95°C and a salinity of 1 wt% KCl. The water bath test dissolution rate fell within the range of the unpurged autoclave, pressurized or not. There was a substantial decrease in the dissolution rate of the autoclave where the nitrogen was used for purging entrapped air. The delayed dissolution rate of the material in the purged autoclave appears to be more representative of the deoxygenated downhole environment. If a plug takes 50% longer than estimated to dissolve based on calculations made from water bath testing, every stage of every well that uses dissolving magnesium is taking longer to come online, thus reducing time to full production.

2.3 Dissolvable magnesium alloy design

Each well is unique in certain ways, for example temperature, pressure, fluid conditions, operational procedures, etc., and the dissolvable plug is also an assembly of various complex parts that bear different stress and strain during application. Therefore, one grade of DM cannot fit for all **DMs**, that is, a great variety of DMs must be developed with different dissolving rates to satisfy well conditions, as well as mechanical properties to meet requirements of plug design. Balanced by application requirements and supply chain, DM is usually categorized first by temperature (low-temperature grade, medium temperature grade, high-temperature grade), by corrosion rate (low rate, general rate, fast rate), by strength (low yield, general, high yield), or by ductility (general and high elongation).

As discussed in introduction, DM technology is developed by an oil service company in the US, and they keep the cost and production scale in mind even at the beginning because of low price of the final product. Since core technology of DM is to form galvanic cell microstructure, the most natural way to achieve industrial goal is to modify the formulation of mature Mg alloy grades through micro alloying. Different from other dissolvable alloy technology developed by academic community like those used in bio or medical field, detail formulation of each commercial DM grade typically kept confidential, but the technical route is similar and open to public. In this section, the general technique routes are illustrated on how magnesium can be alloyed with many elements to enhance properties such as strength, castability, workability, and corrosion rate.

2.3.1 Alloying for mechanical properties

For the traditional Mg alloy grades, aluminum is commonly added to magnesium alloys to form the β phase ($Mg_{17}Al_{12}$) above two weight percent, increasing the strength at the expense of ductility. Alloying with zinc increases both strength and ductility [18], leading to many alloys such as ZK60 being developed as a high-strength low-cost commercial alloy. The addition of zirconium acts as a grain refiner through heterogeneous nucleation in the melt, resulting in further increases in mechanical

properties. However, zirconium will react in situ with aluminum so that the two cannot be used together. Various rare earth elements (neodymium, cerium, gadolinium, yttrium, etc.) are added to create high-strength, thermally stable alloys such as WE43. Rare earth added to aluminum-alloyed magnesium has a positive effect on mechanical properties [19]. Others have reported the addition of sufficient rare earth creates a long-period stacking ordered (LPSO) structure that significantly increases the mechanical properties and thermal stability of an alloy [20]. For commercial DM in oil and gas industry, this microalloying technology or microstructure is still utilized in the exact same way. The only difference is to add suitable noble impurities at reasonable content to make conventional magnesium alloy "dissolvable" without interfering with microstructures that give alloy its mechanical properties.

2.3.2 Alloying for dissolution rate

After an existing commercial alloy or internally developed magnesium formulation has been selected, elements promoting the galvanic cell effect are selected. In one instance, one or more alloying elements are added to create a galvanically-active intermetallic particle. These are created during the casting phase where bulk magnesium alloy melt temperature is less than the temperature of the introduced alloying elements. Solid particles of any unalloyed elements are cooled, and an *in situ* precipitate of any solid particle forms. While avoided in typical applications due to the decrease in corrosion resistance, these intermetallic particles are intentionally created to accelerate the dissolution of the resulting alloy. The type and amount of alloying elements added are modified to obtain the desired corrosion rate in the magnesium alloy.

Another method of creating a dissolvable magnesium alloy is to select elements that prevent the naturally occurring passive MgO surface layer from reforming in a corrosive media. Mercury and gallium both possess this ability and have a high solubility within a magnesium matrix. Above the eutectic point, these elements and their precipitates will form along the grain boundaries, creating areas with vast electropotential differences.

The most common method of appreciably accelerating the corrosion rate of a magnesium alloy is the addition of copper, nickel, and tin. An addition of <4 weight percent copper or < 1 weight percent nickel is adequate to create secondary cathodic phases that accelerate corrosion of the alloy.

2.3.3 Cast magnesium alloy base

Traditionally, cast Mg alloys often contain Al, Mn, Zn, Ag, or rare-earth (RE) elements as one of the major alloying additions. Aluminum is the major alloying element for common casting alloys made in sand, permanent mold, and high-pressure die casting. High-integrity castings for aerospace applications are made with other casting alloys based on Ag, Zn, and Y rather than Al [21]. Very few manufacturers utilize cast method to make magnesium dissolvable component because the casted product cannot achieve mechanical strength required by applications. However, high-quality casting is the first step to make high-quality wrought products. During our development, several groups of elements are found essential during casting step.

The first group of low-melting-point alloying elements (Li, Bi, Ga, In, Pb, and Sn) reduces the liquidus temperatures of the binary alloys, which is generally good for castability of the binary alloys. Alloying with these elements increases the dissolvability of the alloys. The second group of alloying elements (Ca, Si, and Zn) forms various intermetallic phases, which often provide strengthening to the alloys. Zirconium is an effective grain-

refiner for aluminum-free magnesium alloys due to a peritectic reaction in Mg-Zr system. Cerium is also a good grain refiner and can randomize the texture of wrought magnesium alloys while increasing the corrosion resistance. Iron does not form any intermetallic phases within the matrix. Iron is considered as impurity element because it causes micro-galvanic corrosion in Mg alloys. When iron content is high, Mg-Fe-based alloys become dissolvable. It has been reported that degradable alloys can include Mg-Li alloys enriched with tin, bismuth, or other low-solubility alloying elements [22].

2.3.4 Wrought magnesium alloy base

Of commercial extrusion alloys, AZ31 is most widely used in nonautomotive applications. With higher aluminum contents, AZ61 and AZ80 offer higher strength than AZ31 alloy, but at much lower extrudability. The high-strength Zr-containing ZK60 was designed for applications in racing cars and bicycles, such as wheels and stems. WE43 and WE54 have exceptional high-temperature strength and creep performance and can be used up to 260°C. These alloys form the baseline compositions for many compositions of dissolvable magnesium alloys. To take full advantage of well-established manufacturing facilities of these commercial grades, most DM alloy grades are modified from these matures traditional grades for cost reduction or short development time. For example, AZ31 is the basic system to develop general DM grades, AZ61 or ZK 60 are the base for high-strength DM grades, and WE series are typically referenced to make high-temperature DM grades.

Cold working, solutionizing, and heat treatment all have an influence on not just the mechanical properties, but the resulting dissolution rates. The precipitation of phases of varying electropotential may be accomplished through thermomechanical processing. For a given chemistry, grain refinement will create a multiplicity of smaller cells that on the net have more surface area. As corrosion occurs, grains detach from the bulk of the material. Smaller grains detaching due to corrosion result in less mass loss per unit volume than one large grain, thus leading to a measurably smaller corrosion rate.

2.4 Dissolvable magnesium alloy processing

Due to cylindrical shape of final products (**Figures 2** and **3**) and high strength requirements, casting and subsequent extrusion into bar or tubular shape has been finalized by industrialists as the most cost-efficient route to manufacture dissolvable Mg alloy raw material on large scale after over a decade of technology iteration, as discussed in the introduction. High-quality melting and casting could significantly reduce the content of impurities and defects, while hot extrusion and related heat treatment in well-controlled processes are essential to achieve desired microstructures and mechanical properties. All these two steps will be illustrated in this section.

Melting and casting of dissolvable magnesium alloys are the same as non-dissolvable alloys. Many manufacturers utilize the same equipment to create both types of alloys. Of note is the preference for direct chill (DC) semicontinuous casting alloys (**Figure 7**). Molten metal is poured into the open mold from the top. As the partially solidified billet/slab emerges from the mold, water impinges directly on the casting surface. Steady-state casting conditions are achieved when the sump profile ceases to evolve with time relative to the mold. The casting process stops when the desired cast length is obtained or the bottom of the pit is reached. For magnesium alloys, billets up to 500 mm in diameter and 2000 mm in height are produced. The
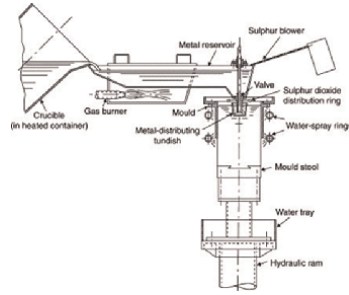
Figure 7.
Schematic of the DC cast process for magnesium alloys, indicating the different heat-transfer regimes [23].
Figure reproduced with permission from Elsevier.

advantages of DC products are high cooling rates due to water spray and no visible cracks as compared to castings in a mold. Also, the DC casting method reduces the internal stress in the cooled material by allowing contractions on all sides, as opposed to only on the top of the ingot in a traditional trough mold [23].

Experientially, of the various methods for shaping magnesium, direct chill casting is the preferred route. In our work, three DM alloy grades, AZ91–1, MS-RE-1 (medium strength rare earth), and HD-RE-1 (high ductility rare earth), were cast by two different methods, vacuum induction melting (VIM) and direct chill (DC) casting, and extruded by the same 6:1 reduction ratio. Sampling tensile from the quarter radius longitudinal direction allowed for a comparison between the two materials. In all but one instance (HD-RE-1 UTS), the mechanical properties of the DC cast material are superior to the VIM cast equivalents (**Figure 8**). The dissolution rate is also found to decrease for each alloy manufactured by DC cast (**Figure 9**). The increased
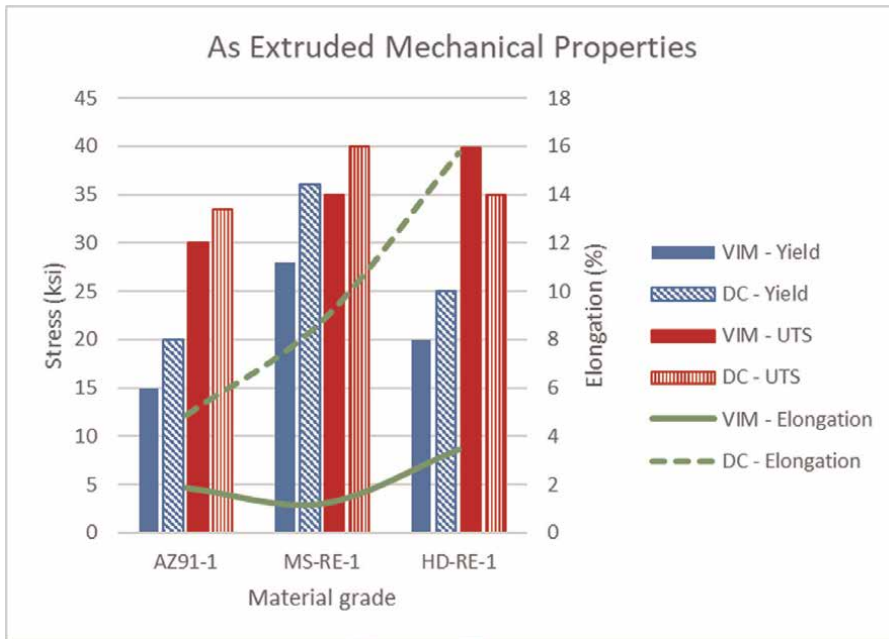
Figure 8.
Comparison of the as-extruded mechanical properties from two casting techniques: VIM and DC.
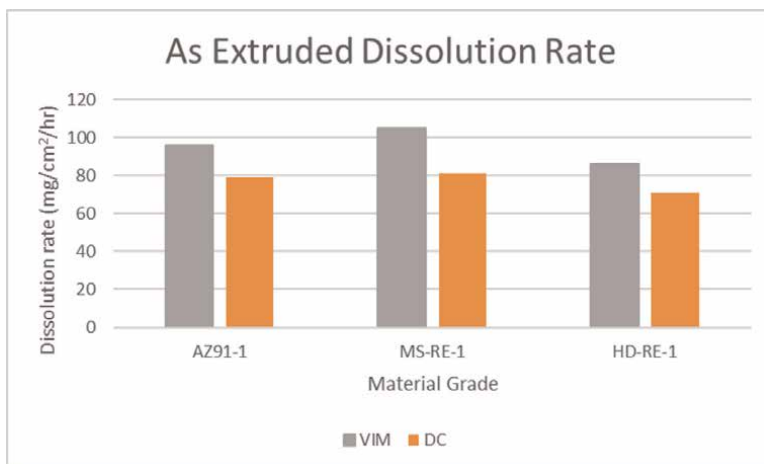
Figure 9.
Comparison of the dissolution rate of material cast by VIM and DC.

mechanical properties and decreased dissolution rate indicate a finer grain structure of DC castings. The melt agitation and fast cooling from DC casting make it the first technical choice for producing dissolvable magnesium alloys.

Casted billet is typically full of defects and does not exhibit enough strength or elongation required by dissolvable plug application. To meet these high requirements, the next step is to hot extrude them into bar or tubular shape. In detail, a billet is pushed or drawn through a die of the desired cross-section in hydraulic presses to produce bars, tubes, and a wide variety of profiles with an excellent surface finish, improved mechanical properties, and hollow sections. High-strength magnesium alloys are more difficult to extrude and need to be extruded at higher temperatures and/or lower speeds, thus lower productivity with a greater risk of failure.

While hollow extrusions can be made with a mandrel and a drilled or pierced billet, it is generally more economical (higher productivity) to use a bridge die where the metal stream is split into several branches and recombined before the die exit. **Figure 10** is schematic illustration of the extrusion setup for the semi-hollow, hollow (using port-hole dies), and solid profiles. It should be pointed out that hollow extrusions produced from port-hole dies have solid-state seams (formed during extrusion)
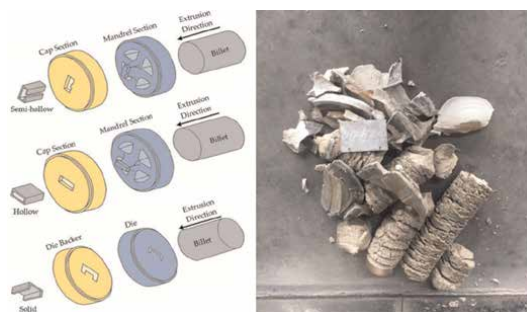
Figure 10.
Schematic illustration of the extrusion setup for the semi-hollow, hollow, and solid profiles (left, [24]) and rare earth-containing magnesium alloy extruded at too high a rate (right).

in the parts. If the components require high-pressure tightness, seamless extrusions produced using mandrel-die are recommended.

Temperature and extrusion rate are two critical parameters for hot extrusion process. They are correlated and strongly dependent on alloy compositions and microstructure of casted billet. For example, 350°C is found to be the optimized temperature in our work to extrude magnesium alloys without rare earth, while those with rare earth require a higher temperature of 400°C. An extrusion rate of 0.6 mm/s is typical for those alloys without rare earth; rates as low as 0.1 mm/s are required for rare-earth magnesium alloys. For development of each new grade as illustrated in Section 2.5, lots of production trials are needed to optimize these two parameters in a costly trial and error process (right, **Figure 10**).

2.5 Grades of dissolvable magnesium

Alloys reported herein cover a wide range of suppliers from the whole dissolvable magnesium industry, including material developed and commercialized internally.

2.5.1 Fast dissolvable alloys

Reaction kinetics are slowed with decreasing well temperature. While the magnesium alloy will eventually dissolve, client requirements of complete dissolution in 15 days force reformulation of alloys. It is simple to take a known alloy and modify the inclusion of impurities that accelerate dissolution. For example, developing AZ31–2 for accelerated dissolution at low-temperature low salinity. Increasing copper by 50% only increased dissolution rate by 36% in AZ31–2A. Increasing the nickel content by 25% in AZ31–2B resulted in an increase of 61%. Increasing both copper and nickel content by 50% for AZ31–2C results in a 115% increase in dissolution rate (**Figure 11**).

The addition of indium to a magnesium-aluminum alloy will also allow for an accelerated corrosion mechanism. Aluminum, despite being a very reactive element, is well known to form a passivating film that makes it corrosion-resistant. Aluminum will inhibit corrosion of magnesium alloys due to the β phase protecting the magnesium matrix phase through a passive surface film. The addition of indium will destabilize the protective aluminum oxide surface film, accelerating the corrosion of the alloy. It has been reported that the indium redeposits back onto the surface, which further deteriorates the film, leading to a corrosion rate increase of 350% in 25°C 3.5% NaCl by adding 3.5 wt% indium [25].
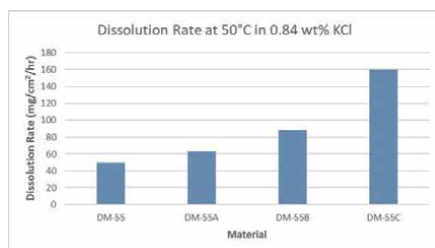
Figure 11.
Dissolution rate response change of a low-temperature magnesium alloy based on AZ31 with increasing noble alloying element inclusion. Measurements performed by CNPC USA.

2.5.2 High-temperature dissolvable alloys

Magnesium experiences a precipitous decline in mechanical properties at 95°C, which is the maximum operational temperature for many US shale wells. Internationally, some shale reservoirs reach temperatures of 175°C, which creates a significant challenge for using dissolvable magnesium (**Figure 12**).

A common solution to stabilize mechanical properties for high-temperature magnesium alloys is to utilize rare earth elements that create secondary precipitates. The addition of rare earth will not only increase the high-temperature stability but also increase the mechanical properties. Apart from the Orowan strengthening of precipitates, strong basal texture and grain size refinement strengthening lead to improved tensile properties at room and elevated temperatures. As previously mentioned, the reaction kinetics accelerate with increasing temperature. Ideally, the number of noble impurities will be decreased to slow the reaction rate to ensure sufficient operational isolation downhole. It can be impractical for manufacturers to manage multiple serializations of a given alloy for various temperatures, so long-duration coatings are often used to provide additional lifetime in situ.

2.5.3 High elongation dissolvable alloys

There exists a need for high elongation alloys, defined as having an elongation of 16 to 28%, for components like foldback rings or metal seals that must deform during the course of setting to support the element or actually create the seal with the casing (**Figure 3**). It is challenging because magnesium has a relatively low ductility due to limited slip planes in the material due to its HCP structure.

An ultra-high elongation magnesium alloy possesses a measured ductility greater than 28%. In our work, Lithium is added to increase ductility with a simultaneous decrease in mechanical strength. Additions of 14% or more lithium will result in a BCC structure that is expressed with high ductility and low mechanical properties. HD-1, HD-2, and HD-3 are high ductility (HD) alloys with no additions of rare earth or lithium. HD-RE-1, HD-RE-2, and HD-RE-3 are high-ductility alloys alloyed with rare earth, without the addition of lithium. **Figure 13** demonstrates the transition starting
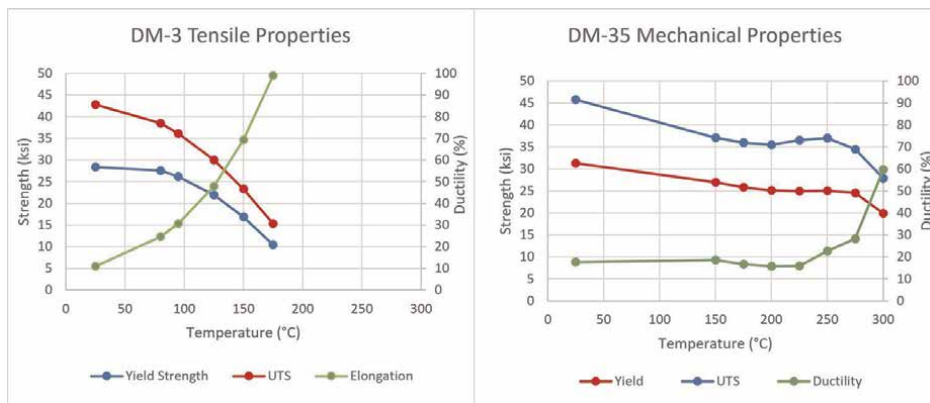
Figure 12.
Degradation of dissolvable magnesium alloy properties as a function of temperature. (left) alloy AZ31–1 formulated without rare earth demonstrates steep strength decline with increasing temperature while (right) alloy with rare earth shows only modest strength decrease even to 300°C. Measurements performed by company CNPC USA.
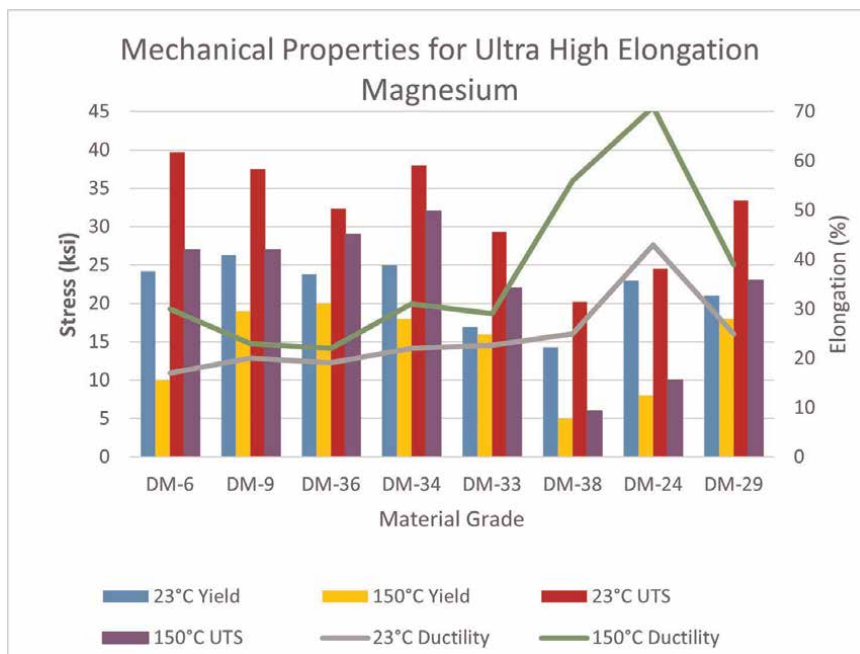
Figure 13.
Plotted mechanical properties of five high elongation magnesium alloys and three ultra-high elongation magnesium alloys. Measurements were performed by CNPC USA.

with a low amount of lithium in UHD-RE-1 that increases in UHD-RE-2. The ductility of UHD-RE-3 decreased despite a similar amount of lithium to UHD-RE-2 due to the addition of more rare earth elements to increase the strength. A passive surface film begins to form, which advantageously slows the corrosion rate for critical high-temperature sealing applications. Additions of yttrium will further reduce the corrosion rate to allow the sealing element to function for the entirety of the fracturing operation. Combining gadolinium and yttrium with lithium and magnesium also leads to particle dispersed strengthening due to phases like Al2Y and microstructure refinement.

3. Dissolvable magnesium failure analysis

Different from conventional Mg alloy, dissolvable magnesium alloy is doomed to "failure", that is, dissolving. Besides qualifying issues from manufacturing process, for example, material cleanliness, micro-cracks or other defects, quality consistency, etc., most common failure of DM is a selection of grade with unsuitable dissolving rate based on wrong testing method (**Table 1**) or ineffective delay coating (Section 4). DM

Condition (1% KCl, 95ºC)	Dissolution rate, mg/cm^2/hour (average)
Autoclave, air	33 ± 1.5
Autoclave, N$_2$ purge	21.5 ± 1.5
Waterbath	32.6 ± 1.0

Table 1.
Comparison of the dissolution rate of AZ31–1 in the same temperature fluid in three different test methods.

simply dissolves too fast, and parts lost mechanical strength (i.e., over-stressed) due to mass loss before hydraulic fracturing finishes. As one of the pioneering operators to develop extremely high-temperature wells, we also found unique stress corrosion cracking (SCC) failure mode when DM is used at elevated temperatures [26].

During a hydraulic fracture operation in a 125°C shale well in our previous operation, a sudden, premature failure was recorded with a plug utilizing rare-earth magnesium alloys HT-RE-1 and HT-RE-2 (high-temperature grade). Due to the nature of the tool, it could not be retrieved to perform a failure analysis. Tests on high-temperature plugs, made from rare earth-containing magnesium alloys, were performed in simulated well conditions where temperature > 140°C and pressure in tap water at pressures exceeding 50 MPa. A plug with HT-RE-1 slips failed suddenly. Subsequent inspection revealed significant fracturing of the HT-RE-1 slips (**Figure 14**). Repeating the test with HT-RE-2 slips resulted in a similar failure, with close investigation, showing an initial crack in at least one slip formed and propagated early into testing. Testing a plug with HT-RE-1 slips in 140°C oil was successful. Despite very low dissolution rates in unstressed conditions, an unknown mechanism involving tap water caused accelerated corrosion and rapid failure of HT-RE-1 and HT-RE-2.

Scanning electron microscopy (SEM) found characteristics of stress corrosion cracking (SCC). A nonobvious alloy, HT-RE-3, was selected as a potential replacement due to the higher elongation, despite a lower yield. Slow strain rate testing (SSRT) was performed in 140°C tap water at a rate of 4.00×10^{-6} in/in/s for HT-RE-1, HT-RE-2, and HT-RE-3 (ASTM G129), there is a substantial decline in mechanical properties when conducting SSRT at 140°C when compared to the results from standard tensile testing at 140°C (**Figure 15**). The extreme decrease in ductility demonstrates water is the factor accelerating the fracture via SCC [26]. Subsequent 140°C tap water plug testing with HT-RE-3 slips was crack-free and successful. A clear
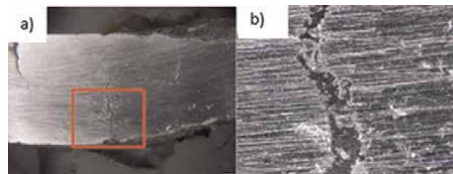
Figure 14.
A cross-sectioned fractured HT-RE-1 slip with (a) an evident crack and (b) a closeup of the fracture.
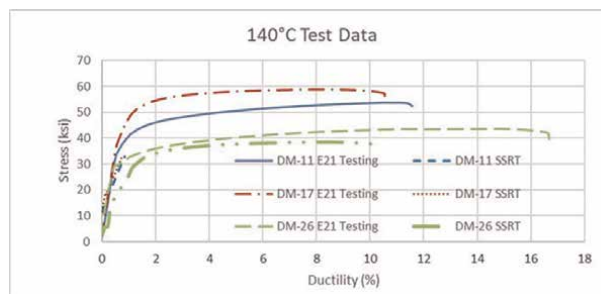
Figure 15.
Comparison of high-temperature tensile testing to SSRT at 140°C for HT-RE-1, HT-RE-2, and HT-RE-3. HT-RE-1 and HT-RE-2 experienced a precipitous decline in properties, whereas only a moderate decline in mechanical properties was measured in HT-RE-3. Measurements were performed by CNPC USA.

relationship between SCC, material microstructure, and chemical formulation was established so that a new grade of alloy with well-designed microstructure was developed to avoid SCC and successfully prevented sudden cracking issues of HT dissolvable plugs used in ultra-HPHT shale well development.

4. Protection and coating for dissolvable magnesium

During field application, degradable plugs are required to keep mechanical integrity under high stress during hydraulic fracturing process in the first 6–24 h (depending on operation design) and to be dissolved as quickly as possible without large solid residual to put wells into production quickly (i.e., high operation efficiency). The former requirement demands DM to have lower dissolving rate so that plug can maintain reliable strength during operation, while the latter requires DM to have dissolving rate as high as possible. A conflicting requirement leads to two kinds of broadly observed failure in field, either "premature" disintegration or not dissolving at all at the end due to wrapping of oily contamination when dissolving rate is too low [27]. To circumvent these contradictory requirements for the DM alloys, delayed surface coating (or "temporary coating"), such as polymer spray coating, has been utilized on a fasting dissolving DM (typically >20 mg/cm^2/hour) to delay its initial dissolving process.

Since all polymers are permeable to gas or water molecules to certain level [28], for immersion application, the rate of base metal corrosion where such coatings are used should not exceed approximately 1.3 mm/year (50 mils/year) according to industrial standards [29]. For typical magnesium DM, corrosion rate is several orders of high than this criteria, and ordinary coatings (typically <500 μm) are doomed to be unreliable. Liner (>2 mm) or inorganic cladding might be an option, but they are typically too thick to protect complex DM parts with tight tolerance in real applications. Since delay coating is just "temporary" (i.e., 6–24 hours.), it is still an effective option as long as coating materials and application process are well-engineered and broadly tested. Since DM plug technology in oil and gas is mainly led by companies, this section will illustrate industrial's common practice of delayed coating on DM plugs, especially the application experience from author's group.

4.1 Low-to-medium temperature coating technology

Low-to-medium temperature typically means the temperature at which DM alloy does not deteriorate in mechanical strength (typically <120°C). Ductility of these DM grades can be typically maintained above 8%, that is, categorized as ductile material in oil and gas industry [28] since heavy precipitation enhancement can be avoided. In this scenario, DM typically fails in the form of general corrosion (i.e., gradual material loss), instead of catastrophic crack failures such as stress corrosion cracking or hydrogen embrittlement. It has a low requirement on coating quality as long as it can provide barrier effect to certain level. Therefore, delay coating that is found effective in protecting DM plugs is typically cost-efficient polymers, such as acrylic, epoxy, and polyurethane, or their combinations. Their selection and coating parameters depend on the downhole environments, including temperature, pressure, fluid salinity, etc., and they are typically trading secrets for each service provider. For example, Kumar et al. reported the usage of phenolic-based and aliphatic-based epoxy on their dissolving Mg products to delay disintegration [30].

The only concern for these spray coatings is uneven protection on different geometries. As reported by Zhao et al., for a typical failure process, coating first breaks at an edge or corner, where coating thickness is typically low (**Figure 16b**) or full of defects such as holidays and pinholes [31]. Fluids then not only corrode the exposed DM substrate immediately under these areas but more importantly infiltrates between the coating/DM interface in the form of film filiform corrosion (Under-film Corrosion, **Figure 16a**), causing material loss. Finally, blistering occurs all over the coating and causes complete breakage of the coating. Therefore, DM parts with sharp edges or corners fail much quicker than those with only smooth surface area (e.g., fracture ball, **Figure 3**), special effort, either an advanced coating or strip coating, needs to be applied to these difficult areas [32] to prevent "premature" disintegration on certain complex parts.

4.2 High-temperature coating technology

In stark contrast to low-temperature fail mechanism, DM alloy typically fails in the form of environmental assistant cracking (EAC) at high temperatures (usually >120°C), instead of a predictable general corrosion process. As discussed above, mechanical strength of traditional Mg alloys typically drops significantly around 120°C due to the degradation of dispersion phases. To maintain reasonable strength (>270 MPa) for high temperature (>140°C) DM plug applications, the so-called HT grades are heavily precipitation-enhanced through rare earth microalloying at cost of alloy ductility [27, 28]. Even though the detailed cracking mechanism, such as stress corrosion cracking (SCC), hydrogen embrittlement (HE), and formation of hydride, is still under debate, however, it is unanimously believed that the loss of elongation of HT grades (typically drop from 15–20% to 5–12%) make that material more susceptible to SCC failures [33–35]. Based on industrial standards [35] and various research [36], coatings, especially organic coating, cannot eliminate the SCC of base metal due to inevitable film defects and gas/moisture permittivity, but it is still an effective option as delay coating, if the stressed DM parts are efficiently isolated from the service environment for 6–24 hours.

Grease and thin polymer coating have been reported to have a synergistic effect to address EAC issue of DM by Zhao et al. [27]. In this combination, HT grease is applied on top of thin polymer coatings, for example, epoxy coatings, silicone coatings, and fluoropolymer coatings, to cover any defects (pinholes, holidays, etc.) within (**Figure 17a**). The effectiveness of this combination was proven by SSRT at 140°C as shown in **Figure 17b**. Compared with the uncoated sample, this coating increased cracking strength from 200 MPa to 352 MPa (76% increase) and doubled elongation (from 0.9–2%). Based on test results it is believed that below a certain strain range,
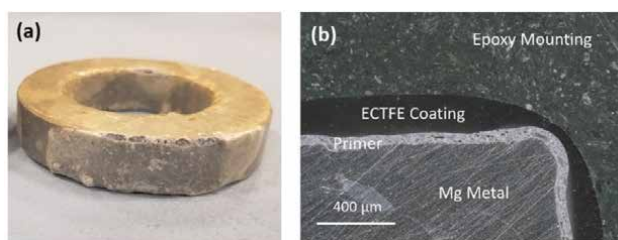
Figure 16.
Photo of (a) failed polymer coating after aging and (b) OM image of ECTFE coating at sample edge area [31].
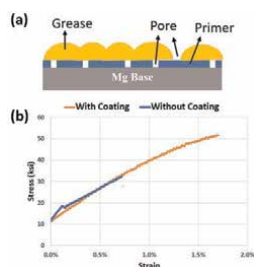
Figure 17.
Schematic illustration of (a) synergistic effect between grease and polymer coating and (b) its effectiveness examined by SSRT. figure reproduced with permission from TMS [27].

the grease coating can prevent SCC of Mg alloy by isolating it totally from corrosive fluids. After further deformation, the grease coating breaks, leaving bare areas unprotected for SCC to initiate. The key technology of this technology is suitable grease material formulation or section (i.e., high-temperature rating, proper consistency, high bonding strength to both metal and polymer base, hydrophobic, with excellent thermal/chemical resistance, and resistant to shearing and impacts, etc.), and its compatibility with polymer coatings. This method is broadly accepted by fields also because of its high "flexibility" in delay time; thicker grease coating always leads to longer delay time, which could provide the operators with a choice at the last-minute change to accommodate unpredictable field requirements if they choose to apply final greasing step on job site manually. This could lead to a significant cost reduction from the perspective of supply chain management.

Given its effectiveness in preventing EAC, grease/polymer combination has been found by Zhao et al., not powerful enough to deal with extremely corrosive environments (i.e., reduced delay time), and extra layer protection is necessary [38]. In his work, failure analysis of grease/polymer combined coatings shows that blistering still occurs near its end stage, therefore, an extra inorganic layer (i.e., surface pretreatment) needs to be added, not only to provide extra barrier but most importantly to prevent filiform corrosion (thus blistering). Among these inorganic coatings, plasma electrolytic oxidation (PEO) coating is tested to be the most effective solution thanks to its dense protective inner layer, high mechanical strength, and most importantly strong affinity to polymers because of its porous top profiles. Since both inorganic PEO layer (15–25 μm) and polymer coating can be controlled thin enough not to interfere with tool assembly and function. Failure analysis on broken areas showed that the blistering issue had been eliminated, and delay time can be doubled due to the existence of inorganic PEO pretreatment [37].

5. Outlook and future direction for dissolvable magnesium

Dissolvable magnesium plugs have had a proven field history over the past decade. Intense effort in dissolvable magnesium alloy development has advanced magnesium alloying and processing as a whole. Driven by several factors like increasing production of oil & gas, the dissolvable frac plugs market size is projected to reach an estimated value of US$ 1178.8 million in 2024 [38]. As more applications are found for DM than hydraulic plugs, oil & gas industry could become of major consumption section of global Mg production. In less than two decades, DM technology evolves

from a concept in lab to a commodity with hundreds of commercial grades. This unique application is obviously a success story to take full advantage of high reactivity of Mg materials. However, there is still lot to be done to further advance this technology.

To deal with increased scarcity of traditional easy oil/gas resources, whole industry moving to more HTHP and unconventional reservoirs, where DM fails in the form of stress corrosion cracking instead of general corrosion process, as illustrated in Chapter 5. High strength and ductility must be achieved simultaneously for this scenario, which has been a significant challenge for current DM industry and requires intensive research effort on both formulation and processing. The most cost-efficient route is still exploring new alloying element systems to form effective precipitation phase. It has been under intensive R&D by both industrial and academic communities [39]. The difficulty of this route is forming thermal stable precipitation phase, which typically requires usage of expensive rare earth elements. Rare earth-free micro alloy technology is reported but its performance is not satisfactory. An alternative route is directly adding advanced filers, with different sizes and geometries, to form the so-called composite or nanocomposite materials [40]. These fillers include but are not limited to inorganic powders (SiC, Al_2O_3, TiO_2, etc.), nanotubes, graphene, etc. Significantly improvement has been reported in various research papers, but this technology is not ready for industrial application because of not only cost but also manufacturing difficulties. It is very challenging in manufacturing scale-up to mix fillers, especially in nanosized, uniformly into DM melt, and solidify/cast them without filler aggregation or introducing defects [41], such as voids, cracks, and detrimental inclusions. PM is a more controlled route to address this issue but has proven to be unsuitable technology due to its low ductility and high cost in mixing. Therefore, more efforts need to spend to scale up the composite fabrication technology from material lab to manufacturing line in mill. The last but least technical route is advanced plastic-deforming technology to reduce current grain size of DM significantly, which obviously increases strength and ductility at same time without modifying formulation. However, these technologies, such as equal channel angular extrusion (ECAE) and friction stir extrusion [42], are still limited to lab research, and there is a long route before industrialization.

In the field application, the by-product of Mg dissolving process, that is, $Mg(OH)_2$, reacts with downhole silicate (either from formation or hydraulic frac sand) to form hard magnesium silicate or aluminum silicate if Al is used as alloying element [43]. The basic mechanism is still under investigation, but formation of this so-called recrystallized material is detrimental to dissolvable plug application because it either warp around DM to prevent it from dissolving or forms a strong cement block *in situ*, blocking the well bore. This recrystallization is strongly related to downhole temperature and fluid conditions and is found even severe in HTHP wells. For example, over 60% failure rate of DM plugs is reported in developing a high-temperature gas well recently, which makes DM plus unsuitable to use. Therefore, a new formulation or dissolving mechanism needs to be developed to prevent recrystallization reaction downhole.

After two decades of intensive R&D on 3D printing technology worldwide, this technology is mature for oil and gas applications from both performance-wise and cost-wise. Various downhole tools and parts are reported to be manufactured from industrial 3D printing process [44], as it brings obvious benefits, such as reduced size (i.e., eliminating joints or connections) and complex shapes not achievable by traditional machining. Given many works have been published in 3D printed Mg alloy [45],

especially dissolvable Mg alloys used in biomedical fields, there is no 3D printing of dissolving metal reported so far in oil & gas industry, probably due to recent downside of the oil market. More R&D efforts need to be invested to bring these benefits to DM downhole tools.

Acknowledgements

Author details

Lei Zhao*, Timothy Ryan Dunne, Jiaxiang Ren and Peng Cheng
CNPC USA, Houston, USA

*Address all correspondence to: lei.zhao@cnpcusa.com

IntechOpen

References

[1] Saltzman D. The art of distillation and the Dawn of the hydrocarbon society. Bulletin for the History of Chemistry. 1999;**24**:53-60

[2] Höök M, Hirsch R, Aleklett K. Giant oil field decline rates and their influence on world oil production. Energy Policy. 2009;**37**:2262-2272. DOI: 10.1016/j.enpol.2009.02.020

[3] IEA. World Energy Outlook 2020. Paris: IEA; 2020. License: CC BY 4.0

[4] Andreas J. The shale revolution in the U.S. and its impact on energy markets, energy security, and the U.S. energy transition. In: International Report of the Konrad-Adenauer-Stiftung. Berlin: Konrad-Adenauer-Stiftung; 2015

[5] Helms D. Horizontal Drilling. North Dakota Department of Mineral Resources Newsletter. 2008;**35**:1-3

[6] U.S. Government Accountability Office. Oil and Gas Information on Shale Resources, Development, and Environmental and Public Health Risks. U.S. Government Accountability Office; 2012

[7] Durey A, Degner D. Bridge-plug Millout with coiled tubing-case histories. In: Paper Presented at the SPE/ICoTA Coiled Tubing Roundtable. Houston, Texas. Richardson, Texas: SPE; 2000

[8] Walton Z, Fripp M, Porter J, Vargus G. Evolution of Frac plug technologies – Cast iron to composites to dissolvable. In: Paper Presented at the SPE Middle East Oil and Gas Show and Conference. Manama, Bahrain. Richardson, Texas: SPE; 2019

[9] Xu ZY, Zhang ZH. The art of disintegration – Ten years in review of disintegrable metals and downhole tools. In: Paper Presented at the Offshore Technology Conference. Houston, Texas. Richardson, Texas: SPE; May 2019

[10] Xu ZY, Agrawal G, Salinas BJ. Smart nanostructured materials deliver high reliability completion tools for gas shale fracturing. In: Paper Presented at the SPE Annual Technical Conference and Exhibition. Denver, Colorado, USA. Richardson, Texas: SPE; October 2011

[11] Fripp M, Walton Z. Degradable metal for use in a fully dissolvable Frac plug. In: Paper Presented at the Offshore Technology Conference. Houston, Texas, USA. Richardson, Texas: SPE; May 2016

[12] Zhang P, Chunsheng P, Jingyang P, Wang Z. Study and field trials on dissolvable Frac plugs for slightly deformed casing horizontal well volume fracturing. ACS Omega. 2022;7:10292-10303. DOI: 10.1021/acsomega.1c06928

[13] Gradl C. Review of recent unconventional completion innovations and their applicability to EGS Wells. In: Proceedings of 43rd Workshop on Geothermal Reservoir Engineering. Stanford, California: Stanford Geothermal Program; February 2018

[14] Galvanic series noble metals By Tugsataydin – Own work (CC BY-SA 4.0) via Commons Wikimedia

[15] Hu H, Nie X, Ma Y. Corrosion and surface treatment of magnesium alloys. In: Czerwinski A, editor. Magnesium Alloys Properties in Solid and Liquid States. London, UK: Intechopen; 2014. DOI: 10.5772/58929

[16] Sherman A, Doud B, Farkas N, Manufacture of controlled rate

dissolving materials, US Patent # 9,757,796, September 12, 2017

[17] Sherman A, Doud B, Farkas N, Galvanically-active in situ formed particles for controlled rate dissolving tools, US Patent # 9,903,010, February 27, 2018

[18] He SM, Peng LM, Zeng XQ, Ding WJ, Zhu YP. Comparison of the microstructure and mechanical properties of a ZK60 alloy with and without 1.3 wt.% gadolinium addition. Materials Science and Engineering A. 2006;**433**:175-181. DOI: 10.1016/j. msea.2006.06.063

[19] Pourbahari B, Emamy M, Mirzadeh H. Synergistic effect of Al and Gd on enhancement of mechanical properties of magnesium alloys. Progress in Natural Science: Materials International. 2017;**27**:228-235. DOI: 10.1016/j.pnsc.2017.02.004

[20] Liu Y, Yang Y, Yi M, Yu J, Li B, Zhang Z. The formation of 14H-LPSO in Mg-9Gd-2Y-2Zn-0.5Zr alloy during heat treatment. Materials (Basel). 2021;**14**(19):1-13, 5758. DOI: 10.3390/ma14195758

[21] Davis J. Metals Handbook Desktop Edition. 2nd ed. Materials Park, OH: ASM International; 1998

[22] Patel D. "Downhole dissolvable plug", US Patent 8,276,670 B2. October 2, 2012

[23] Grandfield JF. Direct chill casting of magnesium extrusion billet and rolling slab. In: Bettles C, Barnett M, editors. Advances in Wrought Magnesium Alloys. Sawston: Woodhead Publishing; 2012. 229 p. DOI: 10.1533/9780857093844.2.229

[24] Qamar SZ, Pervez T, Chekotu JC. Die defects and die corrections in metal extrusion. Metals. 2018;**8**:380. DOI: 10.3390/met8060380

[25] Wang XW, Wang W, Chen W, Chen DM. Effects of indium on corrosion behavior of Mg-Al-Cu alloy. Materials Characterization. 2021;**177**: 111157. DOI: 10.1016/j. matchar.2021.111157

[26] Dunne TR, Yue WH, Zhao L, Nettles D, Cheng P, Ren JX, et al. Addressing corrosion stress cracking issue of magnesium Frac plugs used in ultra HPHT shale well development. In: Paper Presented at the Abu Dhabi International Petroleum Exhibition & Conference. Abu Dhabi, UAE. Richardson, Texas: SPE; November 2021

[27] Zhao L, Yue WH, Ren JX, Dunne TR, Cheng P, Liu HL. Flexible surface treatment technology to enable temporary SCC prevention for Mg dissolvable alloys. In: Proceedings of Magnesium Technology 2022; 05 February 2022. New York: Springer; 2022. pp. 241-248

[28] Heidersbach R. Metallurgy and Corrosion Control in Oil and Gas Production. 2nd ed. Chichester: Wiley; 2011. DOI: 10.1002/9780470925782

[29] Bahadori A. Essentials of Coating, Painting, and Lining for the Oil, Gas and Petrochemical Industries. Amsterdam: Elsevier; 2015. DOI: 10.1016/C2013-0-19127-1

[30] Kumar D, Hernaez ED, Sanchez JS, Xu ZY. Temporary coating for dissolving Frac-balls used in multi-stage fracturing systems. In: Paper Presented at the Offshore Technology Conference. Houston, Texas, USA. Richardson, Texas: SPE; April 2018

[31] Zhao L, Song Y, Dunne T, Ren JX, Yue WH, Yang L, et al. Advanced compound coating for delaying corrosion

of fast-dissolving alloy in high temperature and corrosive environment. International Scholarly and Scientific Research & Innovation. 2021;**15**:71-75

[32] Tekumalla S, Seetharaman S, Almajid A, Gupta M. Mechanical properties of magnesium-rare earth alloy systems: A review. Metals. 2014;**5**:1-39. DOI: 10.3390/met5010001

[33] Xu DK, Han EH, Xu YB. Effect of long-period stacking ordered phase on microstructure, mechanical property and corrosion resistance of Mg alloys: A review. Progress in Natural Science. 2016;**5**:117-128. DOI: 10.1016/j. pnsc.2016.03.006

[34] Song GL, editor. Corrosion of Magnesium Alloys. Amsterdam: Elsevier; 2011. p. 299

[35] NACE MR 0175/ISO15156-1:2020. Petroleum, Petrochemical, and Natural Gas Industries-Materials for Use in H2S-Containing Environments in Oil and Gas Production. Houston: NACE; 2020

[36] Srinivasan PB, Blawert C, Dietzel W, Kainer KU. Stress corrosion cracking behavior of a surface-modified magnesium alloy. Scripta Materialia. 2008;**59**:43-46. DOI: 10.1016/j. scriptamat.2008.02.032

[37] Zhao L, Dunne T, et.al. Route to optimize temporary seal for downhole dissolvable magnesium plug application in HT: Failure analysis and learnings. Paper Presented at AMPP Annual Conference and Expo. Denver, USA. Houston, TX: AMPP; Mar 2023

[38] Stratview Research. Dissolvable Frac Plugs Market Size, Share, Trend, Forecast, & Competitive Analysis: 2019-2024. Jun, 2019. Available from: https://www.stratviewresearch.com/491/dissolvable-frac-plugs-market.html

[39] Saal JE, Wolverton C. Thermodynamic stability of Mg-based ternary long-period stacking ordered structures. Acta Materialia. 2014;**68**: 325-338. DOI: 10.1016/j. actamat.2013.10.055

[40] Nie KB, Wang XJ, Deng KK, Hu XS, Wu K. Magnesium matrix composite reinforced by nanoparticles – A review. Journal of Magnesium and Alloys. 2021; **9**:57-77. DOI: 10.1016/j.jma.2020.08.018

[41] Surappa MK. Microstructure evolution during solidification of DRMMCs (discontinuously reinforced metal matrix composites): State of art. Journal of Materials Processing Technology. 1997;**63**:325-333. DOI: 10.1016/S0924-0136(96)02643-X

[42] Shunmugasamy VC, Khalida E, Mansoor B. Friction stir extrusion of ultra-thin wall biodegradable magnesium alloy tubes -microstructure and corrosion response. Materials Today Communications. 2019;**26**:102-129. DOI: 10.1016/j.mtcomm.2021.102129

[43] Li M, Chen L, Wei R, Liao CL, Fu T. The application of fully dissolvable Frac plug technique in Weiyuan Gasfield. In: Paper Presented at the SPE Kingdom of Saudi Arabia Annual Technical Symposium and Exhibition. Dammam, Saudi Arabia. Richardson, Texas: SPE; April 2018

[44] Deng GJ, Kendall A, Wakefield J. The ultra-expansion completion packer integrated with additive manufacturing technology. In: Paper Presented at the SPE Annual Technical Conference and Exhibition. Dallas, Texas, USA. Richardson, Texas: SPE; September 2018

[45] Karunakaran R, Ortgies S, Tamayol A, Bobaru F, Sealy MP. Additive manufacturing of magnesium alloys. Bioactive Materials. 2020;**5**:44-54. DOI: 10.1016/j.bioactmat.2019.12.004

Chapter 5

Development of Mg-Based Bulk Metallic Glasses and Applications in Biomedical Field

Kun Li and Guoqiang Xie

Abstract

Mg and its alloys have attracted much attention recently as a biomaterial due to their excellent biocompatibility, similar mechanical properties to bone and biodegradability. However, the rapid degradation proved to be challenging to act as an implant. To improve the corrosion resistance and overcome rapid degradation of Mg-based alloys, researchers have been working on the synthesis of Mg-based bulk metallic glasses (BMGs). The first research on Mg-Cu-Y BMG was conducted by Inoue in 1991. Since then, Mg-based BMGs with different systems have been developed. Compared to the crystalline metallic Mg-based implants, the structure of Mg-based BMGs without any regular pattern offers low corrosion reactivity and increase passivity. Mg-based BMGs exhibit a good combination of biological, mechanical and corrosion properties and ease of fabrication. Thus, Mg-based BMGs can be considered an efficient candidate in the biomedical field.

Keywords: Mg-based bulk metallic glasses, mechanical properties, corrosion resistance, biodegradability, biocompatibility

1. Introduction

Bulk metallic glasses (BMGs) can be considered a new group of engineering materials in the field of biomedical materials. As crystallize, the molecules have to find the right place in the lattice and position themselves at the right angle relative to their neighbors. Once the position of the molecule is confused or missing, it will cause defects that affect the comprehensive properties of the material. For glass state, due to fast supercooling the liquid from melting temperature (T_m) to glass transition temperature (T_g) inhibits the crystalline phase to nucleate and grow. Liquid-like disorder is "frozen" to solid BMGs structure due to the fast supercooling rate. This fast-growing new class of materials is known as BMGs. BMGs present more homogeneous structures without microstructural defects like dislocations, grain boundaries, or precipitates, thus exhibiting better and more stable mechanical properties. Comparing to the conventional crystalline metallic counterparts, BMGs exhibit higher strength, lower Young's modulus, improved wear resistance, good fatigue endurance, and excellent corrosion resistance due to the unique amorphous structures. For this

purpose, BMGs have recently attracted much attention for biomedical applications. BMGs such as Ti-based [1–3], Zr-based [4], Mg-based [5, 6], and Ca-based [7] are popular in the biomedical field. Ti-based and Zr-based BMGs are almost impervious to corrosion in the human body; hence they are suitable for permanent implant. And Mg-based and Ca-based BMGs for temporary due to be easily corroded by body fluids [5, 7]. Compared to other materials, Mg is exceptionally light in weight with a density of around 1.74 g/cm^3, and the elastic modulus of Mg is similar to that of natural bone [6]. Further, the ability for magnesium alloys to undergo biodegradation eliminates the requirement for a second surgery to remove the implant. Here, Mg seems to be the promising candidate for biodegradable implants. As a natural element in human body, Mg shows good biocompatibility with no systemic inflammatory reaction or effects on cellular blood composition [8]. Additionally, its degradation releases Mg^{2+} ion and is a cofactor in numerous numbers of enzymes. And the products such as MgO and Mg (OH)$_2$ are expected to be nontoxic to the surrounding tissue. Therefore, researchers viewed Mg-based BMGs as alternative biomaterials for implant applications. Despite the advantages of Mg alloys, the rapid degradation act as a challenge as the implant is unable to retain its structural integrity during the implantation period. To improve the corrosion resistance of Mg alloys, Mg-based bulk metallic glasses have been synthesized and characterized, which can significantly improve the corrosion resistance of Mg-based alloys. In addition to the aforementioned properties, the development of the Mg-based BMGs is of great economic interest as magnesium is abundantly available in land and seawater.

In this chapter, the development of Mg-based BMGs and their application in the biomedical field are introduced. In addition, the high strength, suitable corrosion rate, and biocompatibility of the Mg-Zn-Ca BMGs, which can be considered the most potential system in biomedical field, are described in detail of the mechanical properties, corrosion resistance, and biocompatibility.

2. Development of Mg-based BMGs

2.1 The formation of Mg-based BMGs

The most conventional approach for the development of bulk metallic glasses is through the rapid cooling technique at very low critical cooling rates (<100 K/s). Examples of methods involved in rapid cooling are liquid quenching methods such as injection casting, tilt casting, and melt spinning. The working principle of these processes is that rapid quenching causes the freezing of atoms and does not allow rearrangement and diffusion of an atom. Thus, materials can maintain the glassy structure because of no order or short-range order as rapid quenching freezes the liquid-like atomic arrangement. Cooling rate and degree of crystallization have an important role in dictating the microstructure of the Mg-based BMGs. So the critical cooling rate determines the critical casting thickness—the maximum thickness for glass formation. One can speak of a material's glass-forming ability (GFA) as being either inversely proportional to its critical cooling rate or proportional to its critical casting thickness [8].

The formation of BMG can be concluded as three criteria [9, 10]: (1) Requiring a multicomponent alloy with three or more elements; (2) Exhibit mismatch of atomic size ratio greater than 12% among major constituents; (3) Having a negative heat of mixing between major constituents. This rule signifies the range of glass forming

composition, which often tallies with low melting temperature and eutectic region. It reduced the glass transition temperature according to Eq. (1) as follows [11]:

$$T_{rg} = \frac{T_g}{T_m} \tag{1}$$

T_g is the glass transition temperature and T_m is the melting temperature of the alloy. This is for easy glass-forming alloys where a reduced glass transition temperature (T_{rg}) is normally equal to or higher than 0.6.

2.2 Introduction of Mg-based BMGs

In 1980s, Mg-based metallic glass has been studied. The initial research on Mg-based metallic glass mainly focused on the physical properties such as glass-forming ability, resistivity, hall-coefficient, thermopower, and electron transport properties. In 1991, Inoue et al. [12] first developed Mg-based BMGs, which proved the system of Mg-Cu-Y BMG. It exhibited excellent GFA and a wide supercooled liquid region. The diameter amorphous cylinder (D_c) of prepared Mg-Cu-Y BMG is 1.5 mm with the length of 50 mm (as shown in **Figure 1**).

Copper mold casting method is the most conventional of preparing the Mg-based BMG [13], however, the bulkier a sample is, the more slowly its interior cools. The sample size thus will be limited. With the development of technology, more and more Mg-based BMG systems have been developed successfully with various methods. And these Mg-based BMGs exhibit a wide supercooled liquid region before crystallization and have large GFA. The system of Mg-Ni-Nd BMG with a thickness as large as 3.5 mm is produced through chill-block melt-spinning [14]. Mg-Cu-Ni-Ag-Zn-Y-Gd BMG with a diameter of 14 mm was successfully fabricated by conventional copper mold casting method [15]. Mg-Cu-Ni-Gd BMG systems with a maximum diameter of
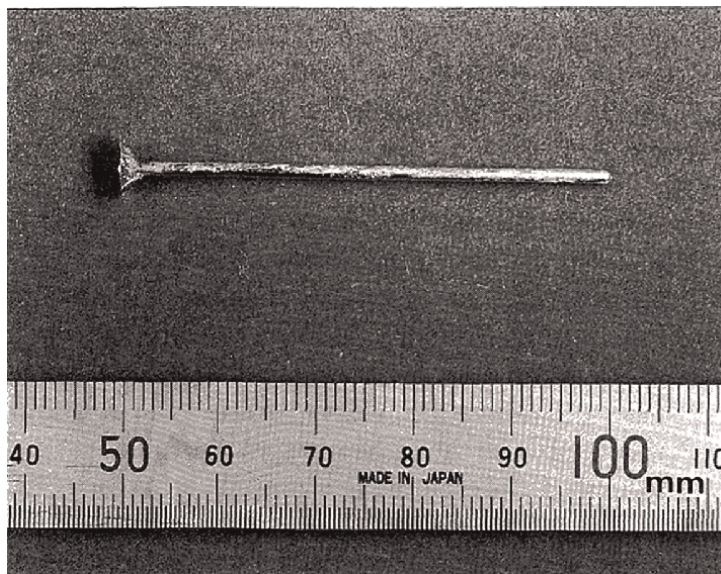
Figure 1.
Mg-Cu-Y BMG produced by low-pressure casting into a copper mold [12].

2.5–5.0 mm were prepared by copper mold casting (**Figure 2**) and exhibited high strength above 900 MPa [16]. Some Mg-based BMG systems and preparation methods are summarized in **Table 1**.

2.3 Structure of Mg-based metallic glasses

Metallic glasses are of utmost importance because of their exceptional chemical, mechanical, and physical properties. They are amorphous in structure without any regular pattern, such as crystalline metallic alloys. Their disorder structure can be realized from a wide range of glassy compositions because of the absence of specific stoichiometries. This is also favorable for the microscopic tuning of properties under
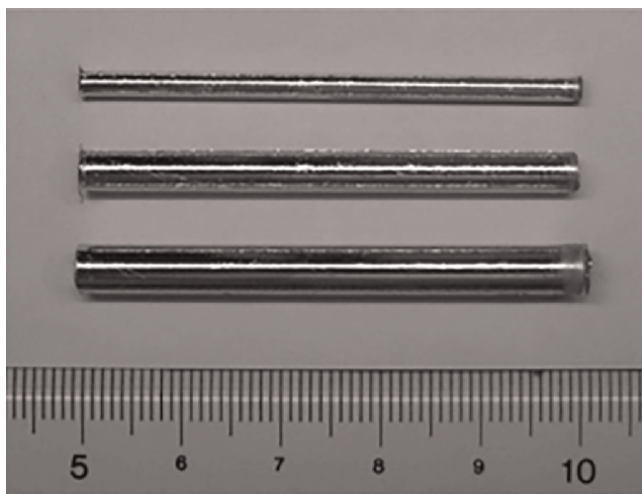
Figure 2.
Outer shape and surface appearance of Mg-Cu-Ni-Gd BMG rods with diameters of 2.5, 4.0, and 5.0 mm, respectively [16].

System	Production method	Diameter (mm)	Refs.
Mg-Cu-Y	Copper mold casting	4	[12]
Mg-Ni-Nd	Chill-block melt-spinning	3.5 (thickness)	[14]
Mg-Cu-Ni-Gd	Copper mold casting	2.5–5.0	[16]
Mg-Cu-Y-Zn	Induction furnace under an inert atmosphere	3	[17]
Mg-Cu-Ni-Zn-Ag-Y-Gd	Copper mold casting	14	[15]
Mg-Cu-Ni-Zn-Ag-Y	Copper mold casting	9	[14]
Mg-Cu-Ag-Er	Copper mold casting	8	[18]
Mg-Ni-La	Injection casting	2.5 ∼ 4.0	[19]
Mg-Zn-Ca-Sr	Copper mold casting	4 ∼ 6	[20]
Mg-Y-Cu-Ag-Pd	Water quenching	12	[21]
Mg-Zn-Ca	Spark plasma sintering	15	[22]

Table 1.
The summary of Mg-based BMGs systems with different diameters by various preparation processes.

a certain range through the optimization of the glass transition composition. Take the Mg-Cu-Y-Ni metallic glass as an example, researchers described the structure of Mg-Cu-Y-Ni metallic glass by experimental and modeling methods. Mg-Cu-Y-Ni metallic glass was prepared in the form of ribbons with a thickness of 0.08 mm and a width of 10 mm by the melt spinning (MS) technique. And they also found that a small amount of Ni could improve the glass-forming ability of an Mg-Cu-Y alloy. As shown in **Figure 3**, the structure of Mg-Cu-Y-Ni metallic glass is presented by the 3D atomic configuration obtained from Monte Carlo (RMC) modeling of the random configuration of 8000 atoms. It can be seen that the distribution of atoms is not completely homogeneous. And the Cu and Y atoms segregate in some areas, indicating the formation of local ordering with more and less dense regions.

Metallic glass has a special microstructure, which is different from crystalline alloy. The X-ray diffraction (XRD) pattern and Differential Scanning Calorimetry (DSC) curve of Mg-Cu-Y-Ni metallic glass are displayed in **Figure 4**. It reveals a typical broad diffraction peak that is centered at about 43° and indicated the formation of an amorphous phase. The sample was heated from room temperature to 600 K at a heating rate of 20 K/min. It can be observed that the Mg-Cu-Y-Ni metallic glass exhibits an endothermic effect of the glass transition followed by a distinct exothermic peak. The detected effects confirm the amorphous structure of the studied sample and allowed the glass transition temperature (T_g = 420 K), the onset crystallization temperature (T_x = 467 K), and the peak crystallization temperature (T_p = 474 K) to be determined. The supercooled liquid region($\Delta T_x = T_x - T_g$) of Mg-Cu-Y-Ni metallic glass can be calculated at about 54 K.
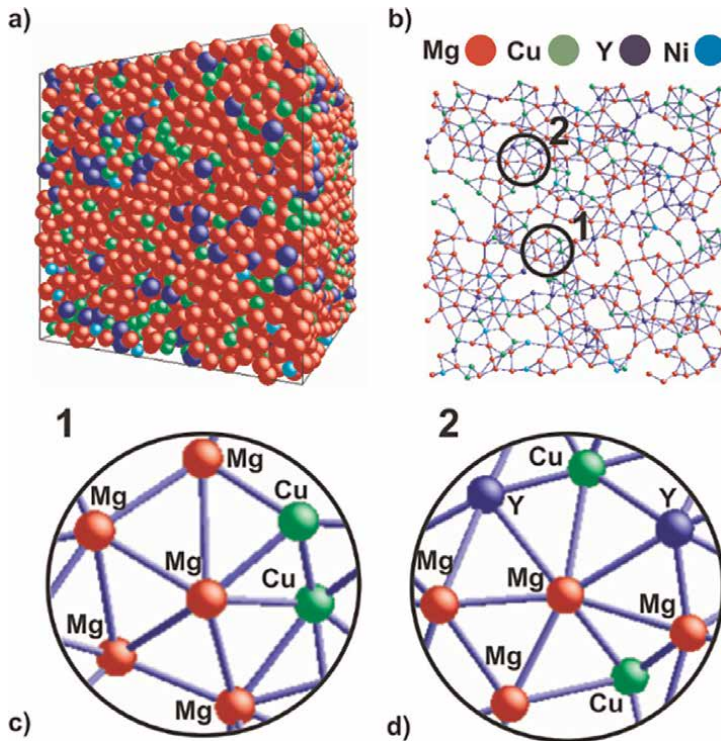
Figure 3.
Structure of Mg-Cu-Y-Ni metallic glass [23].
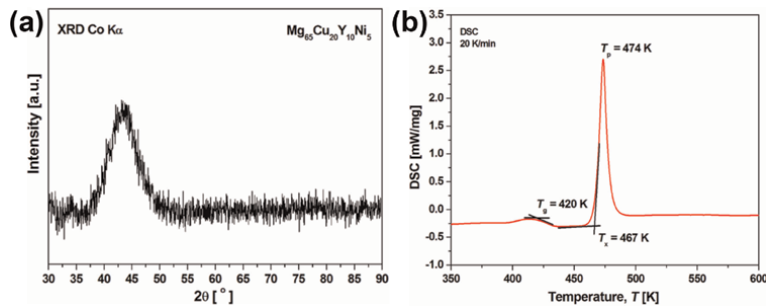
Figure 4.
(a) XRD pattern and (b) DSC curve of Mg-Cu-Y-Ni metallic glass [23].

3. Applications of Mg-based BMGs in the biomedical field

The development of biodegradable BMGs is still in its infancy. Since the inception of an Mg-Zn-Ca BMG in 2005 [24], only Mg-based biodegradable BMGs have been successful as potential contenders for temporary implant applications. For crystalline Mg and its alloy, the rapid degradation rate will precipitate a large amount of hydrogen. Hydrogen evolution that cannot be removed will form pores in the tissue, affecting tissue healing. In contrast to crystalline Mg, the potentially much greater range of alloying elements in an amorphous single-phase structure allows the production of particular metallic glasses with significantly improved corrosion characteristics. This implies that glassy Mg alloys may exist for hydrogen evolution during degradation, which is significantly reduced or even prevented completely [25]. And it is very necessary for the biomedical application.

Recent research into Mg-based BMGs has found that they have higher strength and lower Young's modulus than pure Mg and conventional Mg alloys [26]. In addition, the system of Mg-Zn-Ca BMG presents more uniform corrosion morphology than conventional crystalline Mg alloys, has much lower corrosion rate, and shows higher cell viability than conventional crystalline Mg [5, 27, 28]. All of Mg, Zn, and Ca are essential elements for the human body, the completely nontoxic Mg-Zn-Ca BMG thus has attracted huge attention in biomedical applications.

3.1 Mechanical properties

Although Mg-Zn-Ca BMG shows great potential biomedical applications, however, Mg-based BMGs are among the most brittle BMGs with almost no plasticity [29] at room temperature (**Figure 5**); this limits their potential application [30]. To improve their mechanical properties, it is always preferred to use the particulate-reinforced Mg-based BMGs composite [31–33]. Metallic elements, alloys, polymers, ceramics, and oxides can be selected as the second phase. However, from the previous research, it seems that metal elements are the best reinforcer. Xie et al. [34] introduced Fe particles into Mg-Zn-Ca MG to fabricate composites by ball milling process. After sintered by spark plasma sintering (SPS), the samples exhibit a microstructure of core-shell. The scanning electron microscope (SEM) of Mg-Zn-Ca BMGs and composites with Fe particles are displayed in **Figure 6**. It can be observed that Fe particles distribute on the surface of Mg-Zn-Ca forming a composite material with a core-shell structure where Fe as the second phase is located at boundaries of amorphous regions.
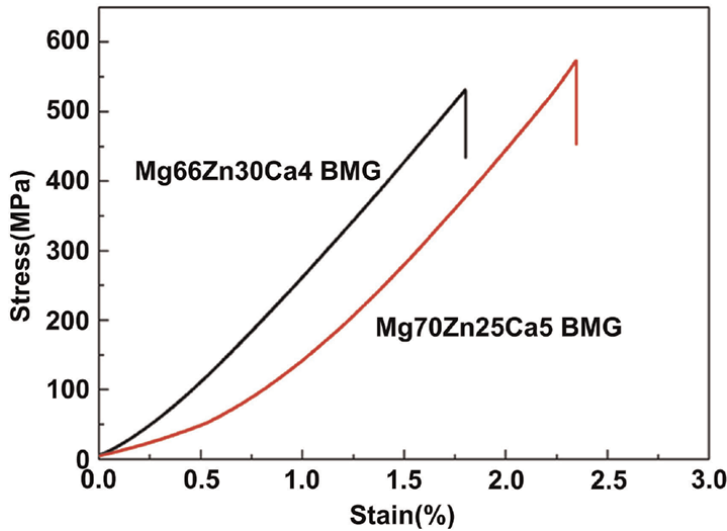
Figure 5.
Compression properties of $Mg_{66}Zn_{30}Ca_4$ and $Mg_{70}Zn_{25}Ca_5$ BMG [29].
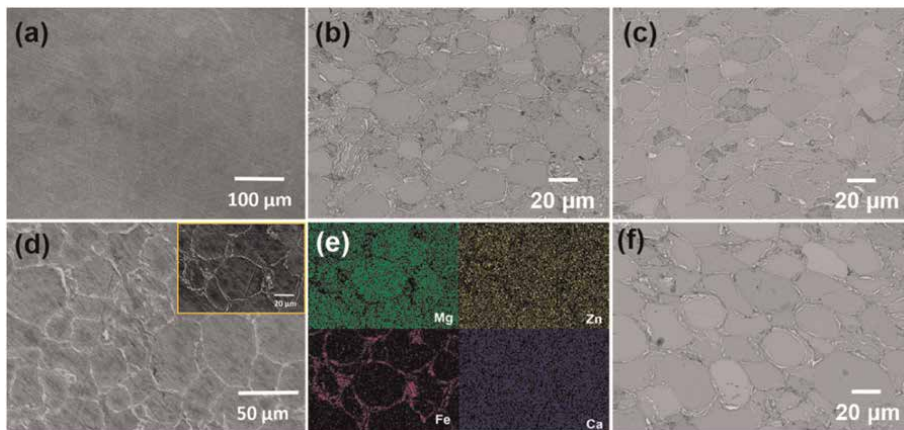
Figure 6.
The SEM images of Mg-Zn-Ca BMG and Mg-Zn-Ca/Fe BMG composite with different Fe after SPS processing, respectively. High resolution of Mg-Zn-Ca/Fe BMG composite is inserted in (d) and (e) mapping images for the element Mg, Zn, Fe, and Ca of Mg-Zn-Ca/Fe BMG composite (with 10% of Fe) [34].

Figure 7 shows the compressive strength of Mg-Zn-Ca BMG and composites with different addition contents of Fe. The stress of Mg-Zn-Ca BMG is 574 MPa while those of the composites are 679 MPa, 738 MPa, 765 MPa, and 641 MPa for the composites with addition of 5%, 8%, 10%, and 12% (mol.%) Fe, respectively. Due to introducing Fe into Mg-based BMG, the composites exhibit an enhanced compressive strength. Therefore, "ex-situ" addition of the elements into metallic glass (MG) matrix can be regarded as an effective and attractive way to improve the mechanical strength. However, the addition of Fe did not improve the plasticity of Mg-Zn-Ca BMG.

It is worth mentioning that Mg-Zn-Ca BMG exhibits good plasticity with the addition of rare earth elements [35]. **Figure 8** displays the compressive stress-strain curves of Mg-Zn-Ca BMG with rare earth Y. The Mg-Zn-Ca glassy alloy also exhibits
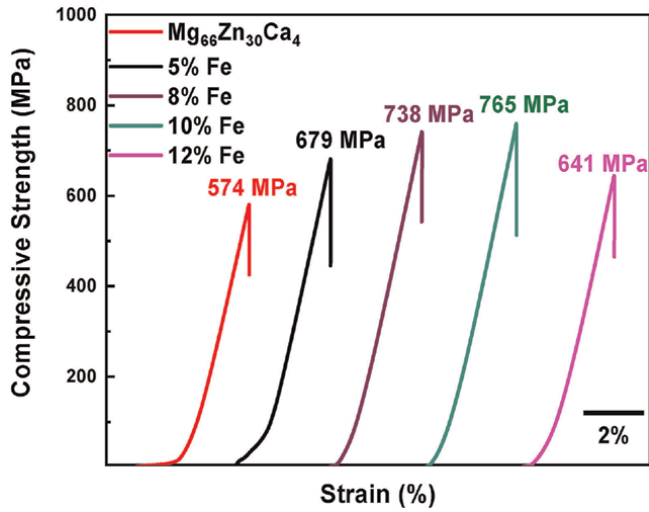
Figure 7.
The compressive stress-strain curves of Mg-Zn-Ca BMG and Fe@Mg-Zn-Ca BMG composites at room temperature [34].
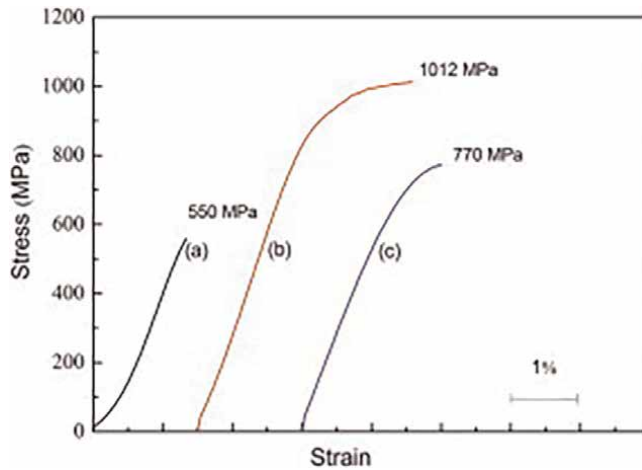
Figure 8.
Engineering strain-stress curves of the $Mg_{69-x}Zn_{27}Ca_4Y_x$: (a) x = 0, (b) x = 1, (c) x = 2 at.% [35].

linear elastic behavior and it only fails in the absence of macroscopic yielding and plastic strain. However, the addition of Y can significantly improve fracture strength. Fracture strength increases from 550 to 1012 MPa (80% increment) with the addition of 1 at.% Y, which is four times higher than that of traditional magnesium alloys and 26% higher than Mg-Zn-Ca metallic glass. The Mg-Zn-Ca-Y Mg-Zn-Ca BMG also exhibits an excellent capacity for plastic strain, above 3.1%, which is 2.5 times higher than the capacity of Mg-Zn-Ca metallic glass. However, the biocompatibility of rare earth elements is still unclear. So rare earth elements as biomedical materials are still very controversial.

More mechanical properties of Mg-Zn-Ca BMG and their composites via different methods are summarized in **Table 2**. It is worth noting that the mechanical properties

System	σ_f	σ_y	A (%)	H_v	Ref
$Mg_{60}Zn_{35}Ca_5$	571	—	—	—	[31]
$Mg_{67}Zn_{28}Ca_5$	432	—	—	—	[31]
$Mg_{68}Zn_{28}Ca_4$	828		1.28	—	[36]
$Mg_{70}Zn_{25}Ca_5$	642	—	0.4	—	[36]
$Mg_{80}Zn_{15}Ca_5$	513		3.58		[36]
$Mg_{66}Zn_{30}Ca_4$	716–854	—	—	—	[37]
$Mg_{71}Zn_{25}Ca_4$	672–752	—	—	—	[37]
$Mg_{60}Zn_{34}Ca_6$	—	888	—	296 ± 25	[38]
$Mg_{73}Zn_{23}Ca_4$	—	636	—	212 ± 19	[38]
$Mg_{66}Zn_{30}Ca_4$	378–587	—	—	257–263	[22]
Mg-Zn-Ca-Cu	583–797	—	—	—	[39]
$Mg_{60}Zn_{35}Ca_5$/Ti	807	—	—	—	[31]
$Mg_{67}Zn_{28}Ca_5$/Ti	690	—	—	—	[31]
$Mg_{66}Zn_{30}Ca_{4-x}Sr_x$	787–848	—	—	2.45–2.51	[20]
Mg-Zn-Ca-Ga	>600	—	—	—	[40]

σ_f: Compressive fracture strength, σ_y: compressive yield strength, A: elongation, H_v: microhardness.

Table 2.
The mechanical properties of Mg-Zn-Ca BMG and their composites.

of Mg-Zn-Ca BMG are differently prepared by different methods. The mechanical properties of Mg-Zn-Ca BMG composites are highly dependent on the inherent properties of the second phase of reinforcement and its volume fraction. However, the plasticity of Mg-Zn-Ca BMG is still not ideal and needs more researches to overcome it.

3.2 Corrosion properties

Crystalline Mg and its alloys show poor corrosion resistance in body liquid, which leads to a fast degradation rate and an uncontrollable hydrogen release. Because of the active chemical reaction between the alloys and the body fluid, the biomedical application of Mg-based alloys is extremely limited. Due to the unique atomic configuration in the absence of translational and rotational symmetry down to sub-nanoscale, Mg-based BMGs exhibit better corrosion resistance compared with crystalline alloys. However, they still cannot meet the clinical needs. Cardiovascular and orthopedic applications are the most important applications of Mg-based alloys, however, for the bioabsorbable cardiovascular and orthopedic applications, it should degrade slowly in the early stage of implantation. Vascular and orthopedic remodeling is generally completed in 90 and 120 days, respectively. After that, it should gradually degrade at an appropriate rate so that the degradation products do not cause adverse reactions in the surrounding tissues. Generally speaking, a full absorption of the cardiovascular and orthopedic applications is expected within two years. Obviously, it cannot be achieved for the current Mg-based alloys and BMGs. Therefore, improving the

corrosion resistance of Mg-based BMGs is still the biggest challenge. The effective ways to improve the corrosion resistance of Mg-based BMGs are introducing other alloying elements [40] and preparing surface coating [41].

The researchers introduced Ga into Mg-Zn-Ca and investigated the corrosion behavior in **Figure 9**. According to the results of electrochemical tests and immersion tests, it can be seen that with the increase of Ga addition, Mg-Zn-Ca-Ga metallic glasses have significantly higher corrosion potential and lower corrosion current density corresponding to higher corrosion resistance. The addition of element Ga can help to form a dense oxide or hydroxide film on the metallic glasses. Ga thus improves the anticorrosion performance of Mg-Zn-Ca metallic glass.

The methods for preparing the coating mainly include plasma spraying, pulsed laser deposition, sol-gel method, electrochemical deposition, and so on. Among these methods, electrochemical deposition is popular because of the relatively low deposition temperature, controllability for a coating composition, and fast deposition rate. In this part, take the electrochemical deposition method as an example. The researchers synthesized a series of calcium phosphate (CaP) coatings on Mg-Zn-Ca metallic glass via the electrodeposition method. Among all bioactive coatings, calcium phosphate (CaP) compounds exhibit outstanding biocompatibility and low toxicity. However, the coating thickness, chemical composition, and morphology will strongly influence the biological activity and degradation rate. Different voltages will influence the coating thickness and morphology. In this work, different voltages including -3.3 V, -3.5 V, and -3.7 V are carried out to prepare coatings with different coating thicknesses. **Figure 10** displays the SEM morphologies of surface and cross-section of electrodeposited coating under different voltages. The flake-like morphology CaP
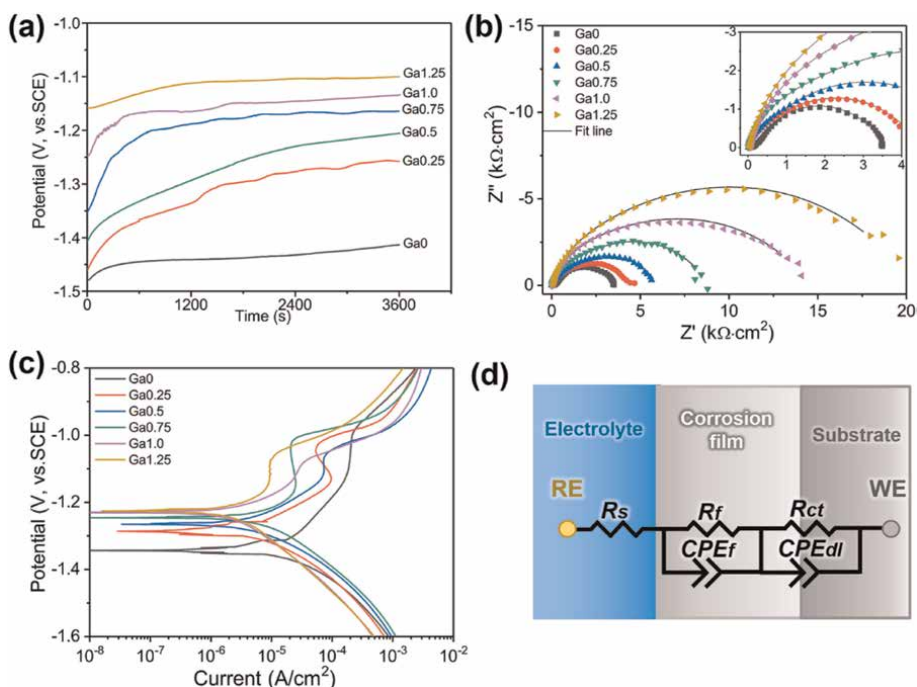
Figure 9.
(a) Open circuit potential (OCP) curves, (b) Nyquist plots, and (c) potential dynamic polarization (PDP) curves of different Mg-Zn-Ca-Ga metallic glasses (Ga0, Ga0.25, Ga0.50, Ga0.75, Ga1.00, and Ga1.25) tested in hanks' solution at 37°C, (d) electrical equivalent circuit (EEC) used in the fitting of EIS result [40].
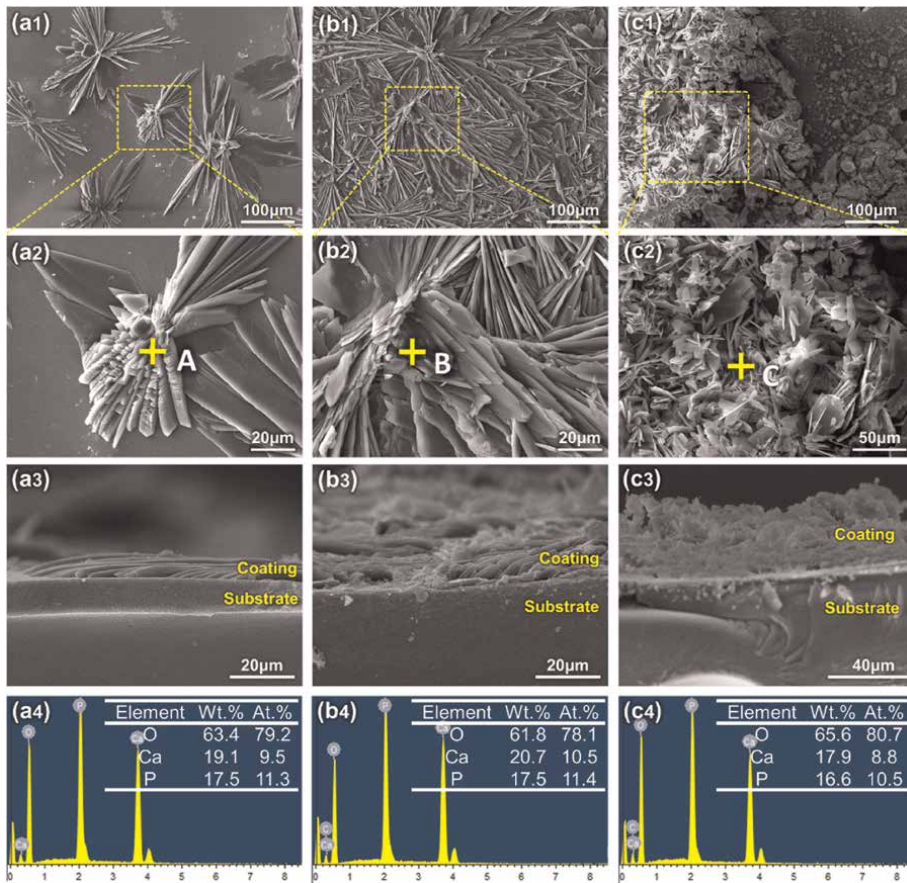
Figure 10.
The SEM morphologies of samples: (a1) (a2) CaP-3.3 V, (b1) (b2) CaP-3.5 V, and (c1) (c2) CaP-3.7 V and the cross-section morphologies of (a3) CaP-3.3 V, (b3) CaP-3.5 V, and (c3) CaP-3.7 V. the corresponding EDS results are provided in (a4), (b4), and (c4) [42].

coatings are formed on the substrate under different electrodeposited voltages. The thicknesses of CaP coating are 3.6 ± 1.6 μm, 8.3 ± 2.1 μm, and 31.1 ± 6.8 μm under different electrodeposited voltages of -3.3 V, -3.5 V, and -3.7 V, respectively. The result indicates the CaP coating is increased with the increase of electrodeposited voltage. Electrodeposited CaP coating can effectively inhibit the reaction between sample surface and liquid environment.

Figure 11 shows the electrochemical results of different electrodeposited CaP coating on Mg-Zn-Ca metallic glass in different samples. From **Figure 11(a)**, the open-circuit potential (OCP) of CaP coating samples is higher than that of Mg-Zn-Ca metallic glass, which indicates higher corrosion potential. In results of fitted electrochemical impedance spectroscopy (EIS) data (**Figure 11(b)** and **(d)**), comparing with the electrodeposited coating samples, Mg-Zn-Ca metallic glass exhibits a significantly smaller capacitive loop and polarization resistance value (3516 Ω cm²). The polarization resistance of the sample CaP-3.3 V increased to 5701 Ω cm², which is slightly higher than that of the Mg-Zn-Ca metallic glass substrate. When the electrodeposition voltage was 3.5 V, the polarization resistance of sample CaP-3.5 V reaches the highest value of 27,110 Ω cm². As the electrodeposition voltage further increased to 3.7 V, the
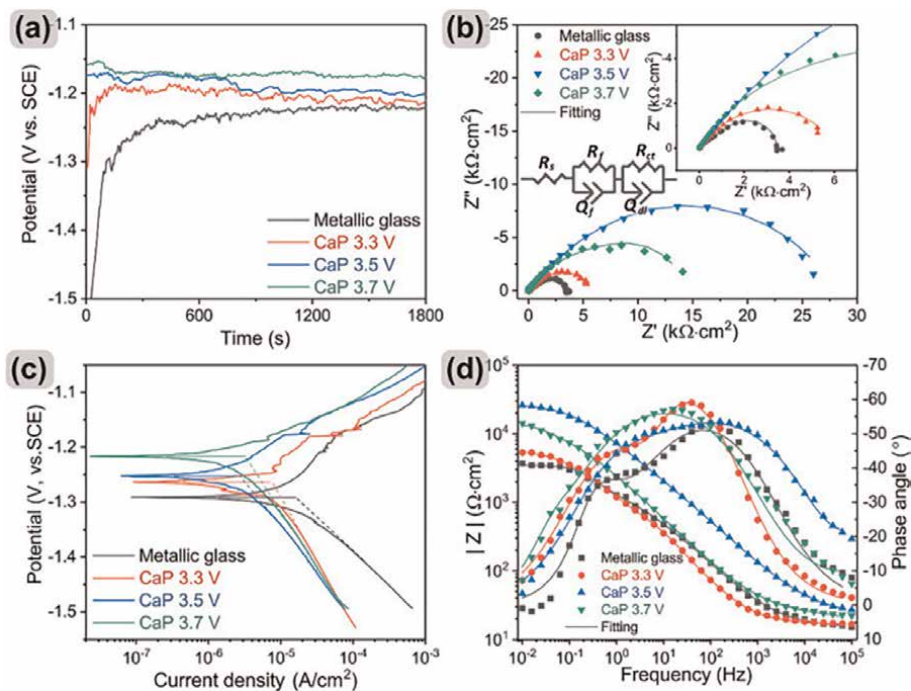
Figure 11.
The electrochemical results of different samples. (a) OCP curves, (b) Nyquist plots, (c) PDP curves, and (d) bode Nyquist plots tested in Hanks' solution [42].

polarization resistance of sample CaP-3.7 V dropped to 14,454 Ω cm^2. According to the EIS fitting parameter (R_p), the corrosion resistance of samples CaP-3.3 V, CaP-3.5 V, and CaP-3.7 V are 1.6 times, 7.7 times, and 4.1 times higher than that of the Mg-Zn-Ca metallic glass. **Figure 11(c)** shows that the value of Mg-Zn-Ca metallic glass is significantly lower than that of electrodeposited coating samples, this result indicates that the electrodeposited CaP coating can effectively inhibit the electrochemical reactions on the sample surface, thus reducing the corrosion rate.

Although a great deal of research has been carried out on the corrosion of Mg-based BMGs, it is worth mentioning: the research on the corrosion mechanism of Mg-based BMGs is still in the early stage, so it is a great challenge to further study the corrosion mechanism of degradable medical Mg alloys.

3.3 Biocompatibility

For implant materials, biocompatibility is the most important evaluation index. It is necessary to ensure that the material is completely nontoxic before further research is necessary. Numerous studies have been conducted on the biocompatibility of Mg-Zn-Ca BMGs both *in vivo* and *in vitro*.

The system of Mg-Zn-Ca BMGs has been proven with excellent biocompatibility. **Figure 12** shows the animal studies in the abdominal walls and cavities (two tissue types apiece) of domestic pigs to evaluate the tissue reactions of the Mg glass during degradation and the hydrogen evolution *in vivo*. Mg-Zn-Ca BMGs discs, together with a crystalline reference Mg alloy (WZ21), were implanted and analyzed after 27 and 91 days. Around both materials, a fibrous capsule, typical of wound-healing processes
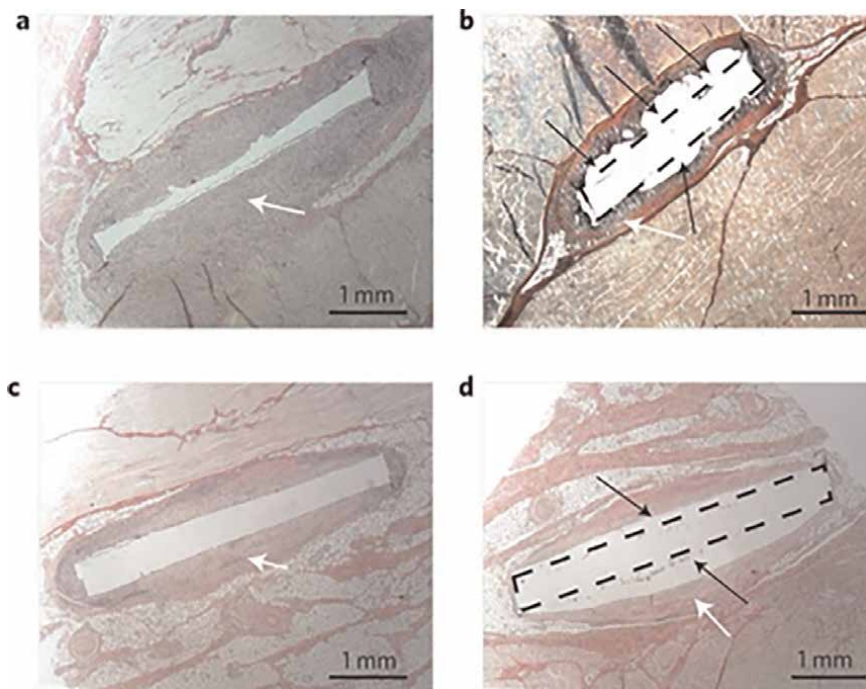
Figure 12.
Animal studies of Mg-based BMG in comparison with a crystalline Mg alloy reference sample. Mg-Zn-Ca BMG (a) and (c) and crystalline Mg alloy reference (WZ21) (b) and (d) [25].

after implant surgery, has developed in all four different tissue types (see the white arrows). Within the capsules, however, gas cavities formed by hydrogen evolution (as indicated by the black arrows in **Figure 12(b)** and **(d)**) are only observed around the crystalline Mg discs. In contrast, no tissue-imprinted hydrogen gas cavities have formed in the histological preparations of the glassy Mg-Zn-Ca samples (see **Figure 12 (a)** and **(c)**). As no inflammatory reaction was observed for any of the implants, the animal tests show that the biocompatibility of Mg-Zn-Ca metallic glass as good as the crystalline Mg alloy [25].

The biocompatibility of Mg-Zn-Ca BMG *in vitro* has also been studied. According to ISO 10993-5: 2009, Mg-Zn-Ca BMG and Mg-Zn-Ca (with 10% content of Fe) BMG composite specimens immersed into high glucose Dulbecco's modified eagle medium (HGDMEM) (Hyclone) supplemented with 10% fetal bovine serum (FBS and Gibco) and penicillin/streptomycin (PS, Gibco). Raw264.7 cells were seeded in a 24-well plate with a concentration of 1.6×104/ML and replaced with a prepared extract after 24 h and cultured for 1, 3, and 5 days. Cells were washed with PBS three times, 500 μl mixed dye was added to each well, and cells were cultured in a cell incubator for 15 min. Live/dead BacLight (Invitrogen) was used to detect the live or dead Raw264.7 cells. Then observe the cell fluorescence by fluorescence microscopy. Green respects living cells and red means dead cells.

Figure 13(a) shows the numbers of RAW264.7 cells culturing in extract of Mg-Zn-Ca BMG and Mg-Zn-Ca BMG composites with addition of Fe for one day, three days, and five days. The number of cells increases significantly from day one to day five, which proves that the two materials are nontoxic and with good biocompatibility for RAW264.7 cells. **Figure 13(b)** presents the quantitative results in **Figure 13(a)**.
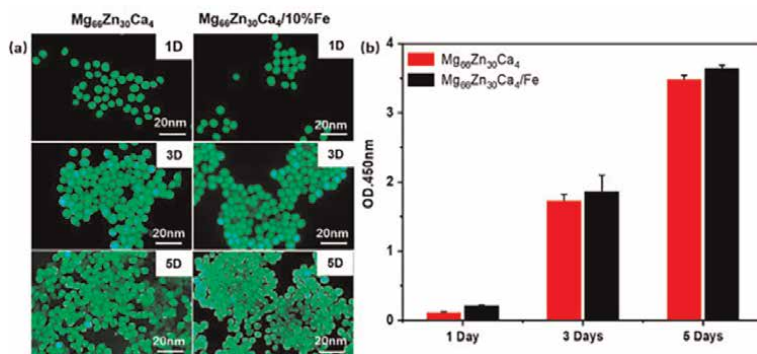
Figure 13.
(a) Live cell staining assay and (b) cell proliferation after culturing RAW 264.7 measured for one day, three days, and 5 days [34].

With the addition of Fe, the absorbance value becomes higher proves the addition of Fe is beneficial to cell proliferation.

Figure 14(A) shows the representative gross sagittal image of a harvested rabbit femur exposing the surgical implant site. All the implanted rods were found to be well-fixed inside the bone tunnel with no evidence of loosening. Before they were sent for histological sectioning, all rods were removed manually. The results show remarkable new bone formation surrounding the Mg-Zn-Ca BMGC and Ti6Al4V alloy at 12 and 24 weeks after implantation (**Figure 14(B)**). In contrast, many osteoblasts are found surrounding the Mg-Zn-Ca BMG and Ti6Al4V alloy rods compared to PLA. No inflammatory cells such as leukocytes or macrophages are localized at the implant sites, signifying good biocompatibility for Mg-Zn-Ca BMG. All rabbits demonstrated good health before sacrificing with no evidence of local (surgical site) or systemic inflammation.

A conclusion can be drawn from the above results, no matter whether *in vivo* or *in vitro*, Mg-Zn-Ca BMG shows superior biocompatibility. With an improved biodegradation rate, excellent biocompatibility, and most importantly, osteogenic ability, Mg-based BMG has great potential for future surgical implant development and application.

4. Conclusions

A large number of studies have shown that Mg-based bulk metallic glasses had a huge application prospect in the field of biodegradable biomaterials. For biodegradable applications, they will degrade gradually in human body after completing their temporary mission (would dissolve completely upon fulfilling the mission of fixing or supporting) during which arterial/bone remodeling and healing would occur. They can be used as a scaffold and bioresorbable implants because they offer an excellent combination of mechanical properties, low degradation rate, and biocompatibility. Through different methods to improve the mechanical properties and corrosion resistance of Mg-based bulk metallic glasses, great progress has been made. However, brittle fracture and fast corrosion rate of metallic glass have not been completely solved, which is the biggest obstacle limiting its application. Despite better resistance
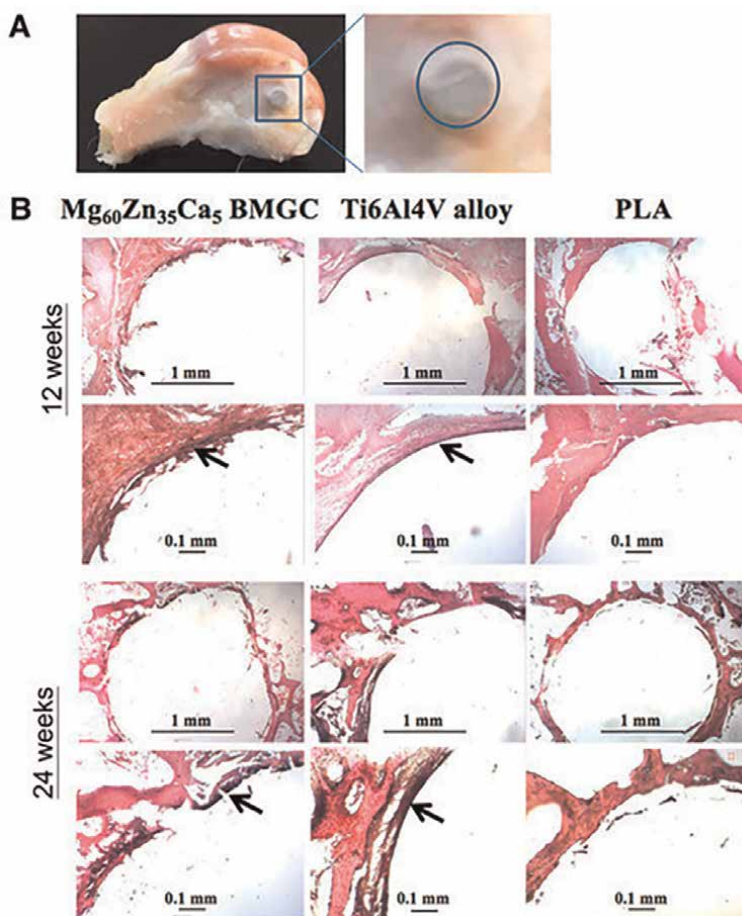
Figure 14.
(A). Gross image of harvested rabbit femur indicating the surgical implanted site of Mg-Zn-Ca BMG, Ti6Al4V, and PLA. The fixation rod was first removed before sent for histologic section. (B) Histological images of the implanted site at 12 weeks and 24 weeks. Black arrows indicate new bone formation [43].

to degradation, more suitable mechanical properties, and biocompatibility, the development of magnesium-based bulk metallic glasses for biomedical applications is still in the stage of infancy. From the processing point of view, challenges remain in obtaining a bulk sample that is a sample that is sufficiently large enough to be of use. What is certain, however, is that the biocompatibility of Mg-Zn-Ca metallic glass system has been fully recognized by implanting in animals experiments. Although initial degradation studies showed promising results compared to their crystalline counterparts, the mechanism behind their *in vivo* degradation is not yet well understood. Mg-based bulk metallic glasses certainly are promising candidates for future biomedical applications. Breakthrough in processing methods to obtain a sufficiently large bulk metallic glass without compromising the amorphous structure should pave the way for accelerated research as a substitute for current biomaterials and in targeted engineering applications.

Author details

Kun Li[1] and Guoqiang Xie[1,2]*

1 School of Materials Science and Engineering, Harbin Institute of Technology (Shenzhen), Shenzhen, China

2 State Key Laboratory of Advanced Welding and Joining, Harbin Institute of Technology, Harbin, China

*Address all correspondence to: xieguoqiang@hit.edu.cn

IntechOpen

References

[1] Du P, Wu ZW, Li K, Xiang T, Xie GQ. Porous Ti-based bulk metallic glass orthopedic biomaterial with high strength and low Young's modulus produced by one step SPS. Journal of Materials Research and Technology. 2021;**13**:251-259. DOI: 10.1016/j.jmrt. 2021.04.084

[2] Xie GQ, Kanetaka H, Kato H, Qin FX, Wang W. Porous Ti-based bulk metallic glass with excellent mechanical properties and good biocompatibility. Intermetallics. 2019;**105**:153-162. DOI: 10.1016/j.intermet.2018.12.002

[3] Xie GQ, Qin FX, Zhu SL. Recent progress in Ti-based metallic glasses for application as biomaterials. Materials Transaction. 2013;**54**:1314-1323. DOI: 10.2320/matertrans.MF201315

[4] Guan BR, Shi X, Dan ZH, Xie GQ, Niinomi M, Qin FX. Corrosion behavior, mechanical properties and cell cytotoxity of Zr-based bulk metallic glasses. Intermetallics. 2016;**72**:69-75. DOI: 10.1016/j.intermet. 2016.02.001

[5] Qin FX, Ji C, Dan ZH, Xie GQ, Wang H, Yamaura SI, et al. Corrosion behavior of MgZnCa bulk amorphous alloys fabricated by spark plasma sintering. Acta Metallurgica Sinica (English Letters). 2016;**29**:793-799. DOI: 10.1007/s40195-016-0451-9

[6] Mear FO, Xie GQ, Louzguine-Luzgin DV, Inoue A. Spark plasma sintering of Mg-based amorphous ball-milled powders. Materials Transaction. 2009; **50**:588-591. DOI: 10.2320/matertrans. MRA2008177

[7] Cai ZY, Chen JY, Xie GQ. Mechanical properties and corrosion resistance of large-size biodegradable Ca-Mg-Zn bulk metallic glasses fabricated via powder

metallurgy. Intermetallics. 2022;**148**: 107633. DOI: 10.1016/j.intermet.2022. 107633

[8] Schroers J. Bulk metallic glasses. Physics Today. 2013;**66**:32-37. DOI: 10.1063/PT.3.1885

[9] Akihisa I, Tao Z, Tsuyoshi M. Glass-forming ability of alloys. Journal of Non-Crystalline Solids. 1993;**156-158**:473-480. DOI: 10.1016/0022-3093(93)90003-G

[10] Inoue A. Bulk amorphous alloys with soft and hard magnetic properties. Materials Science and Engineering A. 1997;**226-228**:357-363. DOI: 10.1016/ S0921-5093(97)80049-4

[11] Dambatta MS, Izman S, Yahaya B, Lim JY, Kurniawan D. Mg-based bulk metallic glasses for biodegradable implant materials: A review on glass forming ability, mechanical properties, and biocompatibility. Journal of Non-Crystalline Solids. 2015;**426**:110-115. DOI: 10.1016/j.jnoncrysol.2015.07.018

[12] Inoue A, Kato A, Zhang T, Kim SG, Masumoto T. Mg-Cu-Y amorphous alloys with high mechanical strengths produced by a metallic mold casting method. Materials Transaction. 1991;**32**: 609-616. DOI: 10.2320/matertrans1989. 32.609

[13] Munir K, Lin J, Wen C, Wright PFA, Li Y. Mechanical, corrosion, and biocompatibility properties of Mg-Zr-Sr-Sc alloys for biodegradable implant applications. Acta Biomaterialia. 2020; **102**:493-507. DOI: 10.1016/j.actbio.2019. 12.001

[14] Li Y, Liu HY, Jones H. Easy glass formation in magnesium-based Mg-Ni-Nd alloys. Journal of Materials Science.

1996;**31**:1857-1863. DOI: 10.1007/BF00 372200

[15] Park ES, Kim DH. Formation of Mg-Cu-Ni-Ag-Zn-Y-Gd bulk glassy alloy by casting into cone-shaped copper mold in air atmosphere. Journal of Materials Research. 2005;**20**:1465-1469. DOI: 10.1557/JMR.2005.0181

[16] Yuan GY, Qin CL, Inoue. Mg-based bulk glassy alloys with high strength above 900 MPa and plastic strain. Journal of Materials Research. 2011;**20**: 394-400. DOI: 10.1557/JMR.2005.0044

[17] Zhang XL, Chen G, Bauer T. Mg-based bulk metallic glass composite with high bio-corrosion resistance and excellent mechanical properties. Intermetallics. 2012;**29**:56-60. DOI: 10.1016/j.intermet. 2012.04.018

[18] Sun Y, Zhang HF, Fu HM, Wang AM, Hu ZQ. Mg-Cu-Ag-Er bulk metallic glasses with high glass forming ability and compressive strength. Materials Science and Engineering: A. 2009;**502**:148-152. DOI: 10.1016/j.msea.2008.10.008

[19] Gonzalez S, Figueroa IA, Todd I. Influence of minor alloying additions on the glass-forming ability of Mg-Ni-La bulk metallic glasses. Journal of Alloys and Compounds. 2009;**484**:612-618. DOI: 10.1016/j.jallcom.2009.05.002

[20] Li HF, Pang SJ, Liu Y, Sun LL, Liaw PK, Zhang T. Biodegradable Mg-Zn-Ca-Sr bulk metallic glasses with enhanced corrosion performance for biomedical applications. Materials & Design. 2015;**67**:9-19. DOI: 10.1016/j.matdes.2014.10.085

[21] Amiya K, Inoue A. Preparation of bulk glassy $Mg_{65}Y_{10}Cu_{15}Ag_5Pd_5$ alloy of 12 mm in diameter by water quenching.

Materials Transaction. 2001;**42**:543-545. DOI: 10.2320/matertrans.42.543

[22] Li K, Li BH, Du P, Xiang T, Yang XX, Xie GQ. Effect of powder size on strength and corrosion behavior of $Mg_{66}Zn_{30}Ca_4$ bulk metallic glass. Journal of Alloys and Compounds. 2022;**897**: 163219. DOI: 10.1016/j.jallcom.2021.163219

[23] Babilas R, Lukowiec D, Temleitner L. Atomic structure of Mg-based metallic glass investigated with neutron diffraction, reverse Monte Carlo modeling and electron microscopy. Beilstein Journal of Nanotechnology. 2017;**8**:1174-1182. DOI: 10.3762/bjnano.8.119

[24] Gu XN, Shiflet GJ, Guo FQ, Poon SJ. Mg-Ca-Zn bulk metallic glasses with high strength and significant ductility. Journal of Materials Research. 2005;**20**: 1935-1938. DOI: 10.1557/JMR.2005.0245

[25] Zberg B, Uggowitzer PJ, Loffler JF. MgZnCa glasses without clinically observable hydrogen evolution for biodegradable implants. Nature Materials. 2009;**8**:887-891. DOI: 10.1038/NMAT2542

[26] Li HF, Zheng YF. Recent advances in bulk metallic glasses for biomedical applications. Acta Biomaterialia. 2016; **36**:1-20. DOI: 10.1016/j.actbio.2016.03.047

[27] Qin FX, Xie GQ, Dan ZH, Zhu SL, Seki I. Corrosion behavior and mechanical properties of Mg-Zn-Ca amorphous alloys. Intermetallics. 2013; **42**:9-13. DOI: 10. 1016/j.intermet.2013.04.021

[28] Qin FX, Dan ZH, Xie GQ. Mg-based bulk amorphous alloy composites fabricated by spark plasma sintering. Materials Science Forum. 2014;**783-786**:

1931-1936. DOI: 10.4028/www. scientific.net/MSF.783-786.1931

[29] Gu XN, Zheng YF, Zhong SP, Xi TF, Wang JQ, Wang WH. Corrosion of, and cellular responses to Mg-Zn-Ca bulk metallic glasses. Biomaterials. 2010;**31**: 1093-1103. DOI: 10.1016/j. biomaterials.2009.11.015

[30] Guo W, Wada T, Kato H. Work-hardenable Mg-based bulk metallic glass matrix composites reinforced by ex-situ porous shape-memory-alloy particles. Materials Letters. 2016;**183**:454-458. DOI: 10.1016/j.matlet.2016.07.082

[31] Wong PC, Tsai PH, Li TH, Cheng CK, Jang JSC, Huang JC. Degradation behavior and mechanical strength of Mg-Zn-Ca bulk metallic glass composites with Ti particles as biodegradable materials. Journal of Alloys and Compounds. 2017;**699**: 914-920. DOI: DOI10.1016/j. jallcom.2017.01.010

[32] Song SM, Wong PC, Chiang CW, Tsai PH, Jang JSC, Chen CH. A bi-phase core-shell structure of Mg-based bulk metallic glass for application in orthopedic fixation implants. Materials Science and Engineering: C. 2020;**111**: 110783. DOI: 10.1016 /j. msec.2020.110783

[33] Jang JSC, Li TH, Jian SR, Huang JC, Nieh TG. Effects of characteristics of Mo dispersions on the plasticity of Mg-based bulk metallic glass composites. Intermetallics. 2011;**19**:738-743. DOI: 10.1016/j.intermet.2011.01.013

[34] Li K, Cai ZY, Du P, Xiang T, Yang XX, Xie GQ. Core-shell $Mg_{66}Zn_{30}Ca_4$ bulk metallic glasses composites reinforced by Fe with high strength and controllable degradation. Intermetallics. 2021;**138**:107334. DOI: 10.1016/j.intermet.2021.107334

[35] Wang JF, Li Y, Huang S, Wei YY, Xi XF, Cai KY, et al. Effects of Y on the microstructure, mechanical and bio-corrosion properties of Mg-Zn-Ca bulk metallic glass. Journal of Materials Science & Technology. 2014;**30**: 1255-1261. DOI: 10.1016/j.jmst.2014. 11.007

[36] Li QF, Weng HR, Suo ZY, Ren YL, Yuan XG, Qiu KQ. Microstructure and mechanical properties of bulk Mg-Zn-Ca amorphous alloys and amorphous matrix composites. Materials Science and Engineering A. 2008;**487**:301-308. DOI: 10.1016/j.msea.2007. 10.027

[37] Zhao YY, Ma E, Xu J. Reliability of compressive fracture strength of Mg-Zn-Ca bulk metallic glasses: Flaw sensitivity and Weibull statistics. Scripta Materialia. 2008;**58**:496-499. DOI: 10.1016/j. scriptamat. 2007.10.052

[38] Matias TB, Roche V, Nogueira RP, Asato GH, Kiminami CS, Bolfarini C, et al. Mg-Zn-Ca amorphous alloys for application as temporary implant: Effect of Zn content on the mechanical and corrosion properties. Materials & Design. 2016;**110**:188-195. DOI: 10.1016/ j.matdes.2016.07.148

[39] Zhao YF, Zhu J, Chang L, Song JG, Chen XH, Hui XD. Influence of Cu content on the mechanical properties and corrosion resistance of Mg-Zn-Ca bulk metallic glasses. International Journal of Minerals, Metallurgy, and Materials. 2014;**21**:487-493. DOI: 10.1007/s12613-014-0933-6

[40] Zai W, Man HC, Su Y, Li G, Lian J. Impact of microalloying element Ga on the glass-forming ability (GFA), mechanical properties and corrosion behavior of Mg-Zn-Ca bulk metallic glass. Materials Chemistry and Physics. 2020;**255**:123555. DOI: 10.1016/j.match emphys.2020.123555

[41] Zhou J, Li K, Wang B, Ai F. Nano-hydroxyapatite/ZnO coating prepared on a biodegradable Mg-Zn-Ca bulk metallic glass by one-step hydrothermal method in acid situation. Ceramics International. 2020;**46**:6958-6964. DOI: 10.1016/j.ceramint.2019.11.074

[42] Zai W, Sun S, Man HC, Lian J, Zhang Y. Preparation and anticorrosion properties of electrodeposited calcium phosphate (CaP) coatings on Mg-Zn-Ca metallic glass. Materials Chemistry and Physics. 2022;**290**:126532. DOI: 10.1016/j.matchemphys.2022.126532

[43] Wong CC, Wong PC, Tsai PH, Jang JSC, Cheng CK, Chen HH, et al. Biocompatibility and osteogenic capacity of Mg-Zn-Ca Bulk Metallic Glass for Rabbit Tendon-Bone Interference Fixation. International Journal of Molecular Sciences. 2019;**20**:2191. DOI: 10.3390/ijms20092191

Edited by Tomasz Arkadiusz Tański,
Katarzyna Cesarz-Andraczke and Ewa Jonda

This book focuses on the processing, potential, and new applications of magnesium alloy systems. To date, the automotive industry uses the unique properties of magnesium alloys on the largest scale. However, scientists propose the use of magnesium and its alloys in many new areas and industries. As such, this book describes and reports on the progress of research on magnesium alloys, for example, in the oil and gas, implantology, and thermoelectric industries. Due to their availability and relatively high mechanical properties combined with low density, magnesium alloys are a dynamically developed group of light metal alloys. Both scientists and industrial centers are involved in expanding the application possibilities of magnesium-based alloys. New applications proposed in this book are examined in relation to technology, functional properties, and potential of the tested materials. The book also examines related challenges of magnesium-based alloys, including implementation problems, encountered barriers and problems to be solved in the scope of the proposed application were described also.

IntechOpen